Graphene and Hexagonal Boron Nitride on Transition Metals and Their Application

---

Dissertation

zur

Erlangung der naturwissenschaftlichen Doktorwürde
(Dr. sc. nat.)

vorgelegt der

Mathematisch-naturwissenschaftlichen Fakultät

der

Universität Zürich

von

Thomas Brugger

aus

Deutschland

Promotionskomitee

Prof. Dr. Thomas Greber (Vorsitz und Leitung der Dissertation)

Prof. Dr. Jürg Osterwalder

Prof. Dr. Harald Brune

Zürich, 2010

Die vorliegende Arbeit wurde von der Mathematisch-naturwissenschaftlichen Fakultät der Universität Zürich im Herbstsemester 2009/2010 als Dissertation angenommen.

Promotionskomitee: Prof. Dr. Thomas Greber (Vorsitz und Leitung der Dissertation),
Prof. Dr. Jürg Osterwalder und
Prof. Dr. Harald Brune.

‘Science is not about learning,
it is about asking good questions.’

freely adapted from
Isidor Isaac Rabi

Abstract

The experimental possibility to manufacture stable single layers of graphite called *graphene* recently opened a new field of physics: The conduction electrons in graphene were found to behave like particles that obey the two-dimensional Dirac equation for massless fermions. For hexagonal boron nitride the fabrication of single layers and their investigation by transmission electron microscopy has been achieved a few months ago. Hexagonal boron nitride is isoelectric to graphene but unlike graphene it is an insulator.

If these two sp^2-hybridized compounds are grown on transition metal substrates superstructures with nanometer periodicity may be found. Depending on the lattice mismatch between the sp^2 layer and the substrate top layer the bond strength of the carbon (boron and nitrogen) atoms to the metal substrate atoms varies on a length scale of several nanometers. This variation can lead to a corrugation of the sp^2 layer forming a highly regular surface texture. It is found that the electrostatic potential above the sp^2 layer is inextricably linked to this surface texture leading to in-plane dipoles above the graphene (hexagonal boron nitride) layer. These dipoles introduce a new functionality: The corrugated sp^2 layers evolve to nano-templates which can act as an array of traps for polarizable adsorbates like for example molecules. This array of traps has the same periodicity as the surface texture. For the corrugated dielectric hexagonal boron nitride layer a different polarization in the loosely bound and in the tightly bound regions of the superstructure unit cell leads to a peculiar electronic structure.

It is also shown that the surface texture of hexagonal boron nitride on rhodium is removable through the intercalation of atomic hydrogen. In the flat state the effect of the corrugation on the electronic structure of the hexagonal boron nitride layer vanishes. The process is reversible as hydrogen may be expelled by mild annealing. This mechanism is proposed to be similarly efficient for hexagonal boron nitride on ruthenium and may also work in the case of the metallic graphene based systems. Thus a route to reversible switching of dielectric and metallic sp^2-hybridized nano-templates is presented.

Experiments on 150 nm thick silicon supported cobalt films show that similar to the nickel case the solid–vacuum interface may be passivated with a commensurate 1×1 overlayer of hexagonal boron nitride. After formation of the hexagonal boron nitride layer the surface electronic structure is governed by sp^2-derived bands for which a large band gap is observed. In addition the solid–vacuum transmission probability for electrons which originate from the metal substrate is strongly reduced. The protection layer is proposed to make the metal film inert and stable against contaminations.

Finally the template functionality of hexagonal boron nitride on rhodium is demonstrated using the example of metal cluster growth. Utilizing a cobalt carbonyl precursor well separated metal clusters are found to nucleate in arrays that have the nanometer periodicity of the template. With this the first step towards a new method for the growth of regular magnetic metal cluster arrays is demonstrated.

Zusammenfassung

Vor wenigen Jahren wurde die experimentelle Herstellung einzelner stabiler Graphit Lagen, genannt *Graphene* realisiert. Dies eröffnete ein neues Forschungsgebiet in der Physik: Es konnte gezeigt werden, dass sich die Leitungselektronen in Graphene wie Teilchen verhalten, die der zweidimensionalen Dirac Gleichung für masselose Fermionen gehorchen. Im Fall von hexagonalem Bornitrid wurde die Herstellung einzelner Lagen und deren Untersuchung mittels Transmissionselektronenmikroskopie erst vor wenigen Monaten erreicht. Hexagonales Bornitrid und Graphene sind isoelektrisch, jedoch ist hexagonales Bornitrid im Gegensatz zu Graphene ein Isolator.

Werden diese beiden sp^2-hybridisierten Verbindungen auf der Oberfläche von Übergangsmetallen gewachsen, so entstehen Überstrukturen mit einer Periodizität im Nanometerbereich. Die Bindungsstärke zwischen den Kohlenstoff- (Bor- und Stickstoff-) atomen und den Metallatomen des Substrates variiert aufgrund der Fehlanpassung der Gitterkonstanten für die sp^2-Lagen und die oberste Substratlage auf einer Längenskala von einigen Nanometern. Diese Variation kann zu einer Wölbung der sp^2-Lage und somit zur Ausbildung einer sehr regelmässigen Oberflächenstrukturierung führen. Es wird gezeigt, dass das elektrostatische Potential über der sp^2-Lage untrennbar mit dieser Oberflächenstrukturierung verbunden ist, was zur Bildung von planaren Dipolen über dem Graphen (hexagonalen Bornitrid) führt. Diese Dipole erzeugen eine neue Funktionalität: Die korrugierten sp^2-Lagen entwickeln sich zu einer Art Nanovorlagen, welche mit einer regelmässigen Anordnung von Stellen erhöhter Bindunsgenergie für polarisierbare Adsorbate, wie zum Beispiel Moleküle, solche gezielt einfangen können. Die Periodizität innerhalb dieser Nanovorlage ist dieselbe wie in der regelmässigen Oberflächenstrukturierung. Im Falle des gewölbten, dielektrischen hexagonalen Bornitrids führt eine unterschiedliche Polarisation für die stark und die schwach gebunden Regionen zu einer eigenartigen elektronischen Struktur.

Es stellt sich heraus, dass die Oberflächenstrukturierung von hexagonalem Bornitrid auf Rhodium durch die Einlagerung von atomarem Wasserstoff entfernt werden kann. In diesem flachen Zustand verschwindet auch die eigenartige elektronische Struktur der Bornitridschicht, welche durch die Wölbung hervorgerufen worden war. Der Prozess kann durch mildes Heizen der Probe umgekehrt werden. Dabei wird der eingelagerte Wasserstoff aus der Zwischenschicht ausgetrieben. Dieser Mechanismus sollte ähnlich effizient auch für hexagonales Bornitrid auf Ruthenium funktionieren. Für die metallischen, auf Graphene basierenden Systeme wird ein ähnlicher Effekt erwartet. Hiermit wird also ein Weg zum reversiblen Schalten von sp^2-hybridisierten Nanovorlagen präsentiert.

Experimente mit hexagonalem Bornitrid auf einem 150 nm dicken Kobaltfilm, welcher auf einer Silizium Unterlage aufgebracht war, zeigen, dass dort eine Situation ähnlich zur Verwendung von Nickel als Metallsubstrat intritt. Die Grenzfläche zwischen Festkörper und Vakuum wird mit einer kommensurablen 1×1 Schicht aus hexagonalem Bornitrid passiviert. Die elektronische Struktur der Oberfläche wird nach dem Wachstum der hexagonalen Bornitrid Schicht von

Bändern dominiert, die von der sp^2-Schicht herrühren. Zusätzlich wird die Übergangswahrscheinlichkeit für die Elektronen aus dem Metallsubstrat vom Festkörper ins Vakuum stark abgeschwächt. Die Schutzschicht macht die Metalloberfläche inert und unempfindlicher gegenüber Verschmutzungen.

Schliesslich wird die Möglichkeit des hexagonalen Bornitrids auf Rhodium zum Einfangen von Adsorbaten noch am Beispiel von kleinen Metallhaufen demonstriert. Unter Verwendung eines Kobalt Karbonyls als Ausgangsstoff wird gezeigt, dass auf dem Bornitrid kleine, räumlich eindeutig getrennte Metallhäufchen mit der Regelmässigkeit der Nanovorlage gebildet werden. Damit wird der erste Schritt für eine neue Methode zum Wachstum regelmässig angeordneter, magnetischer Metallhäufchen aufgezeigt.

List of acronyms

UHV	ultra high vacuum
STM	scanning tunneling microscopy
FFT	fast Fourier transformation
PES	photoelectron spectroscopy
XPS	x-ray photoelectron spectroscopy
UPS	ultraviolet photoelectron spectroscopy
ARPES	angle-resolved photoelectron spectroscopy
ARUPS	angle-resolved ultraviolet photoelectron spectroscopy
LEED	low energy electron diffraction
SXRD	surface x-ray diffraction
BZ	Brillouin zone
SBZ	surface Brillouin zone
FSM	Fermi surface map
PED	photoelectron diffraction
XPD	x-ray photoelectron diffraction
PAX	photoemission of adsorbed xenon
DFT	density functional theory
SQUID	superconducting quantum interference device
TM	transition metal
***h*-BN**	hexagonal boron nitride
g	graphene
2D	two-dimensional
3D	three-dimensional
ML	monolayer
L	Langmuir ($1\,\mathrm{L} = 10^{-6}\,\mathrm{Torr\,s}$)
YSZ	yttria-stabilized zirconia
MOKE	magneto optical Kerr effect
XMCD	x-ray magnetic circular dichroism
TDS	thermal desorption spectroscopy
ROI	region of interest
MBE	molecular beam epitaxy

Contents

1 Introduction **1**

1.1 Interface engineering 1

1.2 sp2-hybridized systems 2

1.3 The nanomesh 4

2 Experimental **11**

2.1 Scanning tunneling microscopy 11

2.2 Photoelectron spectroscopy 13

2.2.1 X-ray photoelectron spectroscopy 14

2.2.2 X-ray photoelectron diffraction 15

2.2.3 Ultraviolet photoelectron spectroscopy 16

2.3 Photoemission of adsorbed xenon 18

2.4 Low energy electron diffraction 20

2.5 Thermal desorption spectroscopy 21

3 Results and Discussion **23**

3.1 Comparison of *g*/Ru and *h*-BN/Ru 23

3.1.1 Theory 26

3.1.2 Results and discussion 26

3.1.3 Conclusions 31

3.2 Reversible switching of surface texture by hydrogen intercalation 33

3.2.1 Experimental 33

3.2.2 Theory 33

3.2.3 Results 35

3.2.4 Conclusions 38

3.3 *h*-BN on Co 41

3.3.1 Experimental 42

3.3.2 Results 42

3.3.3 Conclusions 46

3.4 Co clusters on the *h*-BN/Rh(111) nanomesh 49

3.4.1 Standard Co evaporation 50

3.4.2 Evolution of Co clusters using a cobalt carbonyl precursor 58

4 Summary and Outlook **63**

A Projections **65**

B Nanomesh preparation **67**

C Nanomesh growth without sputtering **71**

D Carbonyl handling **75**

Bibliography **79**

Chapter 1

Introduction

On an introductory level the crystal in solid state physics is usually referred to as being infinite. With this model the so called bulk properties as for example the heat capacity or resistivity of crystals down to a size of several hundred nanometers can be explained very well. However every solid has a surface at which the translational symmetry of the crystal is broken. This surface constitutes the interface from solid to either vacuum, a gas or a liquid and becomes more and more important the smaller the objects under consideration get. The physical properties of the surface may differ considerably from the bulk properties. In semiconductors and certain transition metals for example new electronic states which decay exponentially into the bulk can be found close to the Fermi level in the band gap of the bulk projected bands [1]. Furthermore the abrupt absence of neighboring atoms leads to dangling bonds at the surface atoms making them rather reactive or likely to catch adsorbate atoms [2]. These properties have been studied in detail and in the case of the dangling bonds it was for example found that they play an important role in catalytic processes on surfaces [2, 3]. Depending on the applications this surface effects may either be undesirable or are even wanted to be enhanced. Partial control over this effects can be achieved by volitional modifications of the surface.

1.1 Interface engineering

The two fundamentally different approaches to modify a surface are the *top down* and the *bottom up* strategies. Top down includes all techniques where external tools are used for structuring or functionalization. These are for example lithographic methods like photolithography which is a fast method with a resolution that is currently limited to about 100 nm due to the wavelength of the used light beam. Other lithographic methods include electron beam lithography, focused ion beam lithography and lithography through surface manipulations with atomic force microscopes. Contrary to photolithography where masks are used to illuminate and thus create the whole structure pattern at once these methods are serial methods in which the structuring process is limited to one ‘pixel’ at the time which makes them extremely slow. However the resolution limit of only a few nanometer is orders of magnitude higher than for photolithography. Bottom

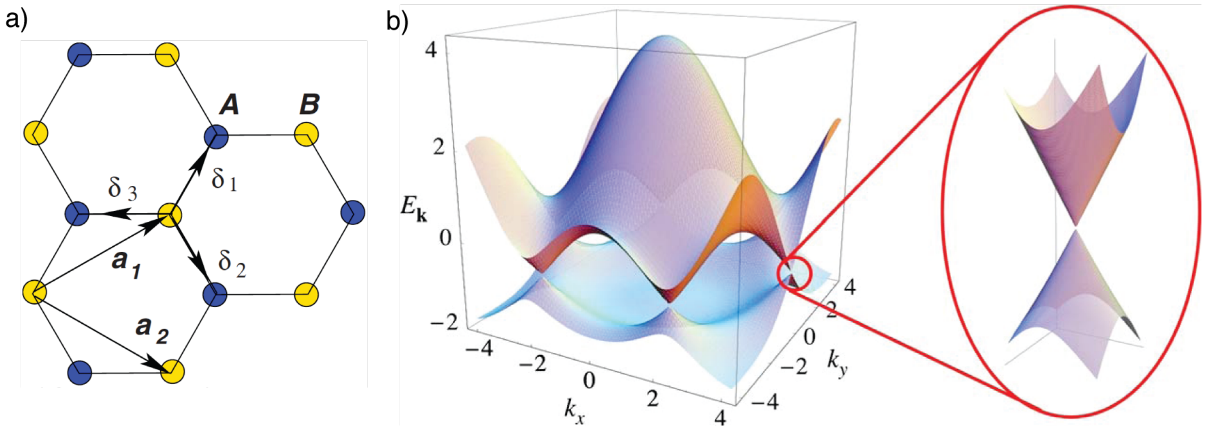

Figure 1.1: a) Two-dimensional lattice structure of a single graphite or h-BN layer. b) Tight-binding results for the dispersion of the π band in graphite. Energy scale in units of the nearest neighbour hopping energy t, reciprocal lattice vectors in units of $\pi/(3a)$ (from Ref. [5]).

up methods rely on molecular self-assembly which is the ability of certain molecules to form regular structures through noncovalent interactions among the single molecules. Molecular self-assembly is for example studied in liquids or on surfaces and is a key concept in supramolecular chemistry. Since about a decade molecular self-assembly is also being used in surface science to design all kinds of regular architectures on the nanometer scale like molecular chains or open networks of free substrate patches framed by molecules [4]. The latter are especially interesting since they may provide regular arrays of host sites for the formation of other nanometer sized entities.

1.2 sp^2-hybridized systems

Among the materials that may be used for the functionalization of transition metal surfaces graphite and hexagonal boron nitride (*h*-BN) are of particular importance. The graphite allotrope α-graphite and *h*-BN both have a hexagonal close packed crystal structure with very similar lattice constants of $a_{\text{graphite}} = 2.464\,\text{Å}$, $c_{\text{graphite}} = 6.711\,\text{Å}$ [6] and $a_{h-\text{BN}} = 2.504\,\text{Å}$, $c_{h-\text{BN}} = 6.661\,\text{Å}$ [7]. It has to be mentioned that the unit cell of the hexagonal layer contains two carbon atoms C_A and C_B in the case of graphite. This may also be regarded as two interpenetrating hexagonal sublattices A and B [Fig. 1.1 a)]. Graphite and *h*-BN are isoelectric with four valence electrons per atom on average. In both compounds the 2s and the 2p valence orbitals of neighboring atoms hybridize to form three sp^2 orbitals which correspondingly lead to three σ bands that are responsible for a strong in plane bonding and stiffness of the lattice. Their name is derived from the s orbitals and is due to the rotational symmetry of the σ orbitals along the connecting line between nearest neighbor atoms. The remaining p orbital is oriented along the out-of-plane direction with the node at the height of the basal plane and usually is referred to as the p_z orbital. It forms the π band of graphite and *h*-BN. The interaction between consecutive layers is weak in both materials and accordingly they may easily slide horizontally. This is one of the reasons why graphite is often used as a lubricant. In spite of all similarities there are also differences between graphite and *h*-BN: Graphite is a semimetal with bands crossing the Fermi level E_F but a vanishing density of states at E_F. It has a highly interesting electronic structure [8, 9]. For the case of *h*-BN the heteronuclear base leads to ionicity (N has a higher electronegativity than B) and renders it an insulator with a band gap of about 5 eV [10, 11].

For the calculation of the band structure of graphite the interaction between planes can be neglect in a first approximation due to the large interlayer spacing of adjacent layers, assuming that conduction only takes place within layers. The three electrons forming the co-planar σ bonds will not participate in conductivity, thus graphite may be treated as having one conduction electron in the 2 p_z state. The Brillouin zone (BZ) of a single layer of graphite called *graphene* (*g*) which contains two states per carbon atom (spin up and spin down) is a hexagon with sides being $2\pi/\left(\sqrt{3}a\right)$ away from the center ($\overline{\Gamma \mathrm{M}}$). In a tight-binding approach where only electron hopping to nearest (hopping between atoms of different sublattices) and next nearest neighbours (hopping between atoms of the same sublattice) is taken into account the solution of the Hamiltonian for the π band is still rather simple due to the pure two-dimensionality as well as the fact that both sublattices are made up of the same atoms [8]. The resulting dispersion relation has the form:

$$\begin{aligned} E_\pm\left(\vec{k}\right) &= \pm t\sqrt{3+f\left(\vec{k}\right)} - t' f\left(\vec{k}\right), \\ f\left(\vec{k}\right) &= 2\cos\left(ak_y\right) + 4\cos\left(\frac{a}{2}k_y\right)\cos\left(\frac{\sqrt{3}a}{2}k_x\right), \end{aligned}$$

where E_+ and E_- are the solutions for the antibonding π^* and for the bonding π band, t and t' are the nearest and the next nearest neighbor hopping energies, respectively. At the K point of the BZ the π^* and the π band touch and within its vicinity both show a linear dispersion relation which can be approximated by

$$\begin{aligned} E_\pm\left(\vec{q}\right) &\approx \pm v_\mathrm{F}\left|\vec{q}\right| + O\left[\left(q/K\right)^2\right], \\ \vec{k} &= \vec{K} + \vec{q}, \quad \text{with} \quad \left|\vec{q}\right| \ll \left|\vec{K}\right|. \end{aligned}$$

Here v_F is the Fermi velocity $\sqrt{3}ta/2$ which is of the order of $10^6\,\mathrm{ms}^{-1}$ and $\vec{q}$ is the momentum relative to the K point [5]. This result is remarkably since v_F does neither depend on the momentum nor on the energy [Fig. 1.1 b)]. The energy at which the two bands touch is termed Dirac energy E_D and does for $t' \neq 0$ no longer correspond to E_F ($E_\pm\left(\vec{q}\right) \approx 3t' \pm v_\mathrm{F}\left|\vec{q}\right| + O\left[\left(q/K\right)^2\right]$). The analogy to Dirac physics results from the fact that the electrons in the vicinity of the K point also obey the 2D Dirac equation for massless particles [12]. Therefore the point in reciprocal space at which $E\left(\vec{k}\right) = E_\mathrm{D}$ is also called the Dirac point.

The high Fermi velocity should in principle lead to conductivities comparable to those of a good metal. But due to the fact that graphite crystallites are very small and their relative orientation is highly disordered, graphite is a poor conductor. However when Novoselov *et al.* succeeded to prepare several micrometer large graphene flakes consisting of only a few layers in 2004 they found ballistic electron transport at submicrometer distances, charge carrier densities of the order of $10^{13}\,\mathrm{cm}^{-2}$ and charge carrier mobilities of up to $10^4\,\mathrm{cm}^2/\mathrm{Vs}$ [13]. This opened a new field in nanotechnology which has been and is still growing vastly since then. Possible applications of graphene include field effect transistors [13], gas sensors [14], perfect nano-balloons [15] and many more. Some actually see graphene as a successor material of silicon for chip fabrication. For many of these applications the graphene needs to be put onto a substrate. Most substrates interact more or less strongly with the graphene layer and the influence on the intrinsic properties of graphene can usually not be neglected [16].

But substrate do not necessarily have to make things worse. They also bear the potential of inducing new functionality to the sp^2-hybridized systems graphene and *h*-BN. The interaction of transition metals with graphite has been studied since decades [17] while for *h*-BN first experimental studies are dated back to the 90s [18]. The systematic investigation of monolayer or few layer graphite and of *h*-BN started shortly after [19]. Recently it has been found that graphene (*g*) as well as *h*-BN may be grown as single layers on the transition metals rhodium (Rh) and ruthenium (Ru). For all four systems *h*-BN/Rh(111) [20], *h*-BN/Ru(0001) [21], *g*/Ru(0001) [22, 23] and *g*/Rh(111) [24, 25] a strong corrugation of the sp^2 layer has been found. In the case of *h*-BN/Rh(111) which has been coined *nanomesh* it was shown that the corrugation induces a new functionality – the ability to trap molecules [26, 27]. It is the aim of this thesis to provide insight into the interaction between the adsorbed sp^2 layers and the Rh(111) and Ru(0001) surfaces as well as to explore their possible applications.

1.3 The nanomesh

The *h*-BN/Rh(111) nanomesh had been discovered in 2003 by Corso *et al.* [20]. It forms upon exposure of the clean 1050 K hot Rh(111) crystal to about 40 L of borazine [$(HBNH)_3$]. Its electronic structure is peculiar and shows two sets of sp^2-derived bands ($\sigma_{1,\alpha}, \sigma_{2,\alpha}, \pi_\alpha$ and $\sigma_{1,\beta}, \sigma_{2,\beta}, \pi_\beta$), separated by about 1 eV in binding energy. The topography as determined by scanning tunneling microscopy (STM) is strongly corrugated by about 0.5 Å but highly regular. This surface texture can be described by a hexagonal superstructure of low *h*-BN regions called 'holes' surrounded by high *h*-BN regions called 'wires' with a super-lattice constant of about 3.2 nm. After its discovery the *h*-BN/Rh(111) nanomesh was proposed to consist of two *h*-BN layers on top of each other, each with open apertures of about 2 nm plus a lateral registry shift of half a super-lattice unit cell. Later it was found that it is actually made up from a single corrugated *h*-BN layer on top of the Rh(111) surface [26, 28]. Figure 1.2 juxtaposes atomically resolved STM and density functional theory (DFT) results of the *h*-BN/Rh(111) single layer model. Due to the lattice mismatch of 6.9 % between the laterally rigid *h*-BN layer and the Rh(111) substrate ($a_{\mathrm{Rh}} = 3.8034\,\text{Å}$ [29]) the registry of the BN units with respect to the Rh substrate atoms gradually varies within the large nanomesh unit cell. surface x-ray diffraction (SXRD) unambiguously showed that this unit cell consists of 13×13 BN units that coincide with 12×12 Rh units [30] and is stable up to about 1100 K [31]. Within regions where N atoms occupy *top* and B atoms occupy *fcc* positions [(N,B)$\sim (top, fcc)$] the attractive forces of the Rh atoms on

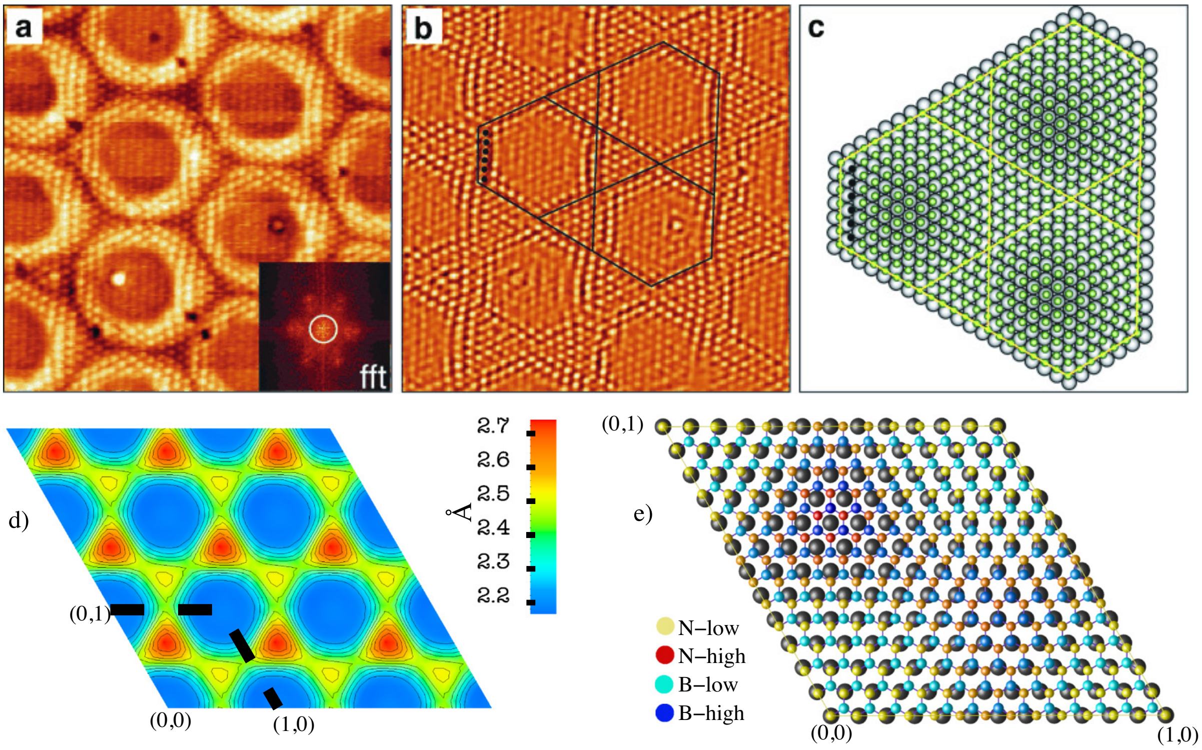

Figure 1.2: a) – c) Atomic structure of the *h*-BN/Rh(111) nanomesh derived from STM topographic data (from Ref. [26]). a) STM image taken at $T = 77\,\mathrm{K}$ in which the h-BN nanomesh is atomically resolved ($9.4 \times 9.4\,\mathrm{nm}^2, I_t = 1\,\mathrm{nA}, V_s = -2\,\mathrm{mV}$). Only one atomic species is imaged. b) Image a) filtered by FFT in order to remove the 3.2 nm nanomesh periodicity and to emphasize the atomic corrugation in the wires and pores. c) Atomic model for the single-layer nanomesh representing the N atoms (green spheres) for the area delimited by the black lines in b).
d) and e) Atomic structure of the *h*-BN/Rh(111) nanomesh as it results from DFT calculations (from Ref. [28]). d) Contour map of the z coordinate of N atoms in the 3×3 nanomesh unit cell. e) Ball and stick model of the nanomesh unit cell (with just one metal layer). Colors indicate the height of the B and N atoms.

the B atoms are strongest whereas the repulsive ones on the N atoms are weakest[1]. Thus the *h*-BN layer is in close contact to the Rh substrate ($d_{\mathrm{Rh-N}} \approx 2.2\,\mathrm{Å}$) leading to the ‘holes’ of the nanomesh. The ‘wires’ of the nanomesh consist of two regions where *h*-BN is in loose contact with the Rh substrate: (N,B)$\sim$ (fcc, hcp) with $d_{\mathrm{Rh-N}} \approx 2.7\,\mathrm{Å}$ and (N,B)$\sim$ (hcp, top) with $d_{\mathrm{Rh-N}} \approx 2.5\,\mathrm{Å}$ [28]. In the STM image displayed in Figure 1.2 b) the super-lattice corrugation with its periodicity of 3.2 nm has been filtered out by removing the super-lattice diffraction spot in the fast Fourier transformation (FFT) of Image 1.2 a) (inset). The resulting image resembles the calculated contour map of the z coordinate of the N atoms above the Rh substrate well [Fig. 1.2 d)]. It unveils the two inequivalent triangular regions of BN atoms constituting the ‘wire’ region as well as the abrupt height change which occurs in the transition from the ‘hole’ to the

---

[1] *top*, *hcp* and *fcc* positions are those in-plane coordinates where a substrate atom can be found in the first, the second and the third substrate layer of the (111) face of a solid with *fcc* crystal lattice, respectively.

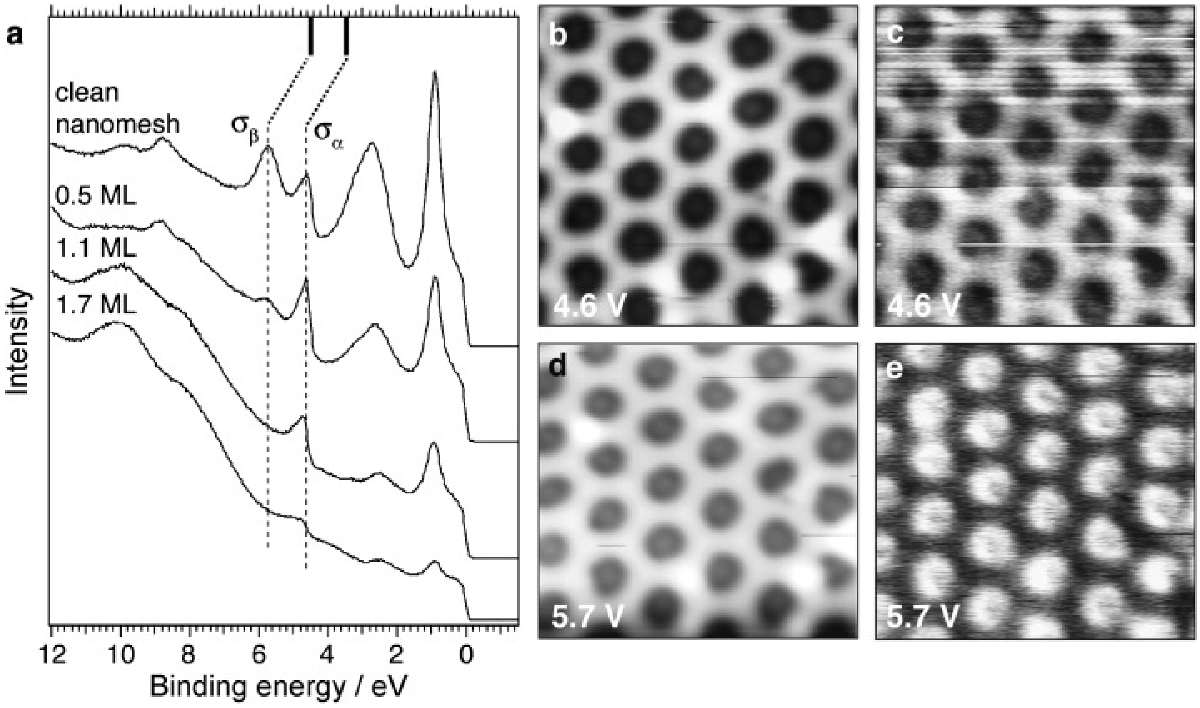

Figure 1.3: Electronic structure of the *h*-BN/Rh(111) nanomesh (from Ref. [26]). a) Normal emission UPS for increasing coverages of naphthalocyanine (Nc) molecules. b) and d) Constant-current STM images ($15 \times 15\,\text{nm}^2$ and $15 \times 13\,\text{nm}^2$) of the clean nanomesh measured at $I_t = 0.1\,\text{nA}$ and sample bias voltages of $V_s = -4.6\,\text{V}$ and $V_s = -5.7\,\text{V}$, respectively. Conductivity (dI/dV) maps recorded simultaneously with the topographic images in b) and d) are shown in c) and e).

'wire' region.

For a free-standing *h*-BN layer a charge transfer of about $0.6\,\text{e}^-$ from B to N occurs due to the higher electronegativity of N [32, 33]. When the *h*-BN layer is brought into contact with the Rh(111) surface an additional polarization takes place. This static polarization is caused by a higher probability for the *h*-BN valence electrons to reside on the interface side rather than on the vacuum side of the *h*-BN layer [34]. This polarization has similar effects as a charge transfer from the *h*-BN layer to the substrate but does not lead to a p-doping of the *h*-BN layer – it remains insulating [32, 35]. The polarization strength depends on the Rh–N distance and thus differs for 'holes' and 'wires' leading to an unequal electronic structure for both. This difference in electronic structure explains the band splitting which had been observed in ultraviolet photoelectron spectroscopy (UPS) and also the unequal local density of states (LDOS) distribution which had been measured using scanning tunneling spectroscopy [26]. Figure 1.3 a) shows normal emission UPS data where the σ band splitting of the clean nanomesh can clearly be seen (topmost curve). From top to bottom an increasing amount of naphthalocyanine (Nc) molecules ($C_{48}H_{26}N_8$) had been evaporated on the clean nanomesh. STM images reveal that the molecules are exclusively occupying the 'holes' of the nanomesh [Fig. 1.4 c)]. Due to that the intensity of the photoelectrons originating from the σ_β band which corresponds to the low *h*-BN region is strongly attenuated up to a coverage of about 1 ML while the other peaks are less strongly affected. Starting from about 1 ML also the other peaks are heavily damped indicating that also 'wire' sites begin to be occupied by molecules. In addition STM topography images and LDOS (dI/dV) maps of the clean nanomesh recorded by STM with a lock-in technique are presented. The data were taken for the two different sample bias voltages $V_s = -4.6\,\text{V}$ and $V_s = -5.7\,\text{V}$ corresponding to the tunneling from states located at the energy position of the σ_α and the σ_β band in normal emission UPS, respectively. In the topography images for both bias voltages the 'wires' are mapped as protrusions and the 'holes' are mapped as depressions [Fig. 1.3 b) and d), respectively]. However the LDOS map at the energy of the σ_α band has its main weight on the 'wires' whereas the LDOS map at the energy of the σ_β band has its main weight on the 'holes' [Fig. 1.3 c) and e), respectively].

The corrugation of the *h*-BN/Rh(111) nanomesh also has an important effect on its functionality. Due to the dissimilar BN–Rh charge transfer for 'holes' and 'wires' the electrostatic potential above the *h*-BN layer varies within the super-structure unit cell: In the close contact region it is about 0.5 eV smaller than in the loose contact region. This leads to a corrugation of the local work-function amplitude that is pinned to the topographic corrugation. But more importantly lateral in-plane dipoles are formed at the positions where the gradient of the corrugation amplitude is maximal thus forming rings of radial dipoles at the rims of the nanomesh 'holes'. If the *h*-BN/Rh(111) nanomesh is approached by a polarizable entity, as it may be a certain molecule or a rare gas atom, its induced dipole leads to an enhanced bonding of the entity to the rim of the nanomesh 'holes' caused by dipole-dipole interactions. The afore mentioned modulation of the local work-function within the nanomesh unit cell and the enhanced bonding at the rims of the nanomesh have been quantified experimentally by photoemission of adsorbed xenon (PAX) [27]. The work-function at a distance of 3.8 Å above the *h*-BN layer was indeed found to be 0.3 eV higher on the 'wires' than on the 'holes'. Thermal desorption PAX measurements showed that the Xe on the 'wires' and most of the Xe in the 'holes' ($\approx 60\,\%$) has a desorption energy of about 0.18 eV. However about 40 % of the Xe in the 'holes' experiences a bonding to the nanomesh which is enhanced by a factor of 1.13 and therefore desorbs only at a higher temperature. This corresponds to 12 Xe atoms which were proposed to be located at the rims of the nanomesh 'holes' forming a Xe ring with an outer diameter of about 2.1 nm comparable to the 'hole' diameter observed in STM. This combined experimental and theoretical study finally provided an explanation for a great discovery which had been made earlier – the trapping of molecules in the 'holes' of the nanomesh upon evaporation *at room temperature* [26]. Figure 1.4 c) shows an STM image of the *h*-BN/Rh(111) nanomesh after evaporation of Nc molecules on the clean nanomesh at room temperature. Almost every 'hole' of the nanomesh holds at least one Nc molecule while no 'wire' site is found to be occupied by molecules. So the nanomesh turns out to be a nano-template for the bottom-up fabrication of highly ordered molecular arrays.

In order to judge the potential of the *h*-BN/Rh(111) nanomesh for possible applications, like for example large-area sorting of molecules, we tested its stability. It was found that the nanomesh is stable in air for at least several days. After a short UHV annealing normal emission UPS showed

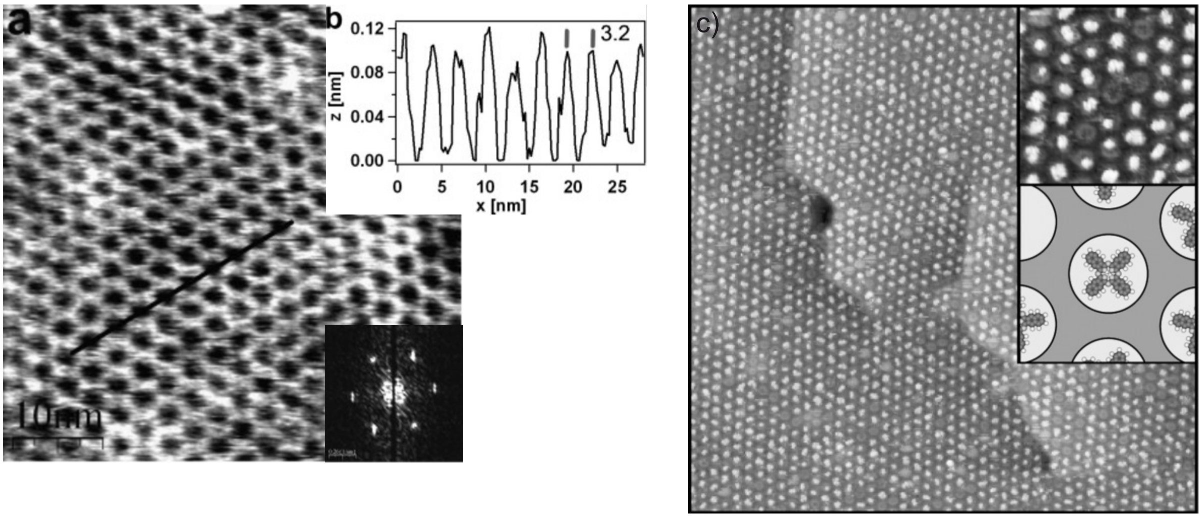

Figure 1.4: a) and b) Stability of the nanomesh in aqueous solutions. a) STM image of the nanomesh in 0.1 M $HClO_4$ at $+120\,\text{mV}$ vs. mercury sulphate reference electrode, $V_t = 50\,\text{mV}, I_t = 100\,\text{pA}, \Delta z = 0.15\,\text{nm}, \text{RMS} = 0.03\,\text{nm}$. b) Profile line along black line drawn in a). FFT of STM image from a) at right panel. From Ref. [36]
c) Site-selective adsorption in the nanomesh pores. STM image ($120 \times 120\,\text{nm}^2, I_t = 0.3\,\text{nA}, V_s = 1.3\,\text{V}$ showing a nearly complete monolayer of Nc molecules on the nanomesh. The top right inset shows an enlargement ($19 \times 19\,\text{nm}^2$) and gives a high-resolution view that shows trapping of the Nc molecules inside the nanomesh pores. The middle right inset shows a schematic representation of the molecular structure of Nc ($C_{48}H_{26}N_8$) on top of a nanomesh pore. From Ref. [26]

spectra comparable to those taken directly after the preparation. Even STM images that showed the unique topography of the nanomesh were recorded. An immersion into 0.1 M perchloric acid ($HClO_4$) for several minutes also did not harm the nanomesh. Figure 1.4 a) shows a STM image that has been taken *in situ* in 0.1 M $HClO_4$ [36]. The superstructure is clearly observable and for the applied sample potential of $+120\,\text{mV}$ with respect to a mercury sulphate reference electrode (MSE) has been stable for several hours. Though successive sweeping of the sample potential between $+260\,\text{mV}$ and $-540\,\text{mV}$ led to a considerable roughening of the nanomesh surface texture. Nevertheless after UHV annealing of the sample low energy electron diffraction (LEED) showed an intact nanomesh superstructure indicating that the *h*-BN/Rh(111) nanomesh is even a very robust and inert nano-template.

The properties of the *h*-BN/Rh(111) nanomesh are unique but the *h*-BN/Rh(111) nanomesh itself is not unique in a sense that it would be the only system exhibiting the above discussed astonishing properties. On Ru(0001) ($a_{\text{Ru}} = 2.7059\,\text{Å}, c_{\text{Ru}} = 4.2815\,\text{Å}$ [37]) a larger lattice mismatch to *h*-BN ($\approx 7.5\,\%$) when compared to Rh(111) exists. Nevertheless a *h*-BN/Ru(0001) nanomesh with similar properties as on Rh(111) can be grown by exposure of the hot crystal to borazine [21]. Due to the fact that *h*-BN is more strongly bound on Ru than on Rh [33] the diameter of the nanomesh ‘holes’ as seen by STM is bigger on Ru. The band structure of *h*-BN/Ru(0001) again shows a splitting of the σ bands and the π band [38] and it was found that the Ru nanomesh may act as a template for gold cluster growth [39]. Up to now Rh and Ru are the only elements on which the *h*-BN nanomesh growth could be observed.

Chapter 2

Experimental

2.1 Scanning tunneling microscopy

With the development of the scanning tunneling microscope (STM) at the IBM research laboratory in Zurich, for which they were awarded the Nobel price in physics in 1986[1], Binnig and Rohrer launched a new era in the field of surface science [40]. Their instrument, whose working principle is based on the quantum mechanical tunneling effect for electrons through thin vacuum barriers, made it possible to image individual surface atoms in a real space image for the first time. A sharp metal tip usually made of W, Pt or Pt/Ir is brought into close contact with the sample surface (distance $5-50\,\text{Å}$) and a bias voltage V between these two electrodes is applied. Due to the close distance d of the electrodes their electron wave functions overlap and lead to a small but finite tunneling current I. For a rectangular tunneling barrier the solution of the one dimensional Schrödinger equation leads to

$$I \propto e^{-2\kappa d}.$$

The parameter $\kappa = \sqrt{2m(V_b - E)/\hbar^2}$ contains the electron mass m, the average barrier height V_b, Planck's constant $\hbar$ and the energy E of the state which for usual tunneling conditions is close to the Fermi energy E_F. The very high vertical resolution of the STM is caused by the exponential dependence of the tunneling current on the sample-tip separation ($1\,\text{Å}$ decrease of d increases I by almost one order of magnitude). A topographic map is than created by scanning the tip over the surface with a very precise piezo motor point by point, line by line, controlling the tip-surface distance in a way to keep the tunneling current constant (Fig. 2.1a).

For an accurate description of the tunneling current the vacuum barrier can be treated with first-order perturbation theory since for typical tip-sample separations (about $9\,\text{Å}$ nucleus-to-nucleus) the coupling between tip and sample is weak. In the case of small bias voltages V this results in the Bardeen formula [41]

$$I = \frac{2\pi}{\hbar} e^2 V \sum_{\mu,\nu} |M_{\mu,\nu}|^2 \delta(E_\nu - E_\text{F}) \delta(E_\text{F} - E_\mu),$$

---

[1] http://nobelprize.org/nobel_prizes/physics/laureates/1986/

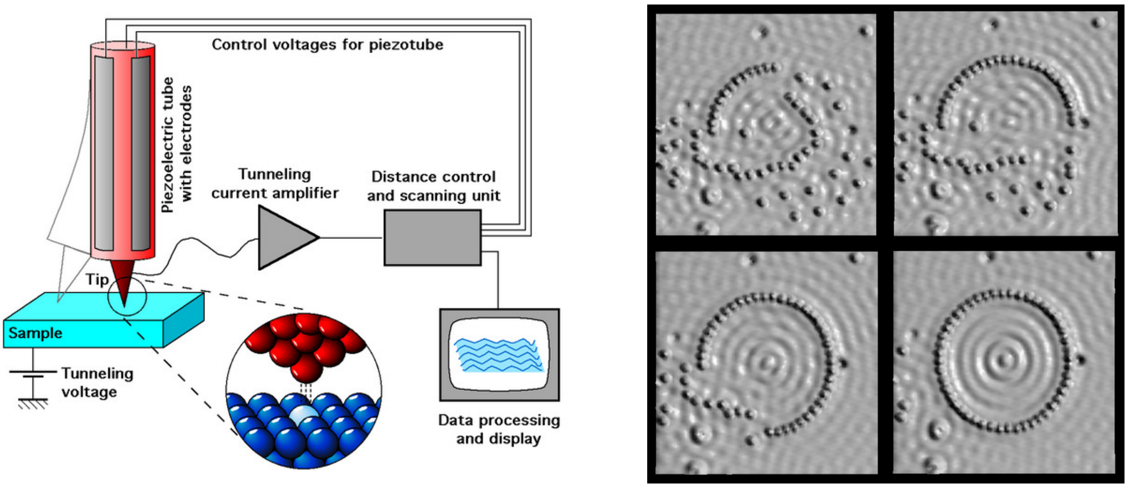

(a) Schematic diagram of a scanning tunneling microscope (from `http://www.iap.tuwien.ac.at/www/surface/stm_gallery/stm_schematic`).

(b) Series of STM images showing the subsequent formation of a ring of 48 Fe atoms on a Cu(111) surface by single atom manipulation with the STM tip ($V_{sample} = 10\,\mathrm{mV}$, $I_t = 1.0\,\mathrm{nA}$, from `http://www.almaden.ibm.com/vis/stm/gallery.html`).

Figure 2.1: Working principle of the STM and very impressive early data of Crommie *et. al* demonstrating the capability of the method, also for the manipulation of single atoms [43].

where e is the elementary charge and $M_{\mu,\nu}$ the tunneling matrix element between states ψ_μ and ψ_ν of the respective electrodes. E_μ and E_ν are their respective energies. Tersoff and Hamann showed that as long as the tunneling matrix elements can be adequately approximated by those of an s-wave tip wave function the tunneling current at small voltages reduces to

$$\begin{aligned} I &\propto \sum \left|\psi_\nu(\vec{r}_t)\right|^2 \delta(E_\nu - E_\mathrm{F}) \\ &\equiv \rho(\vec{r}_t, E_\mathrm{F}), \end{aligned}$$

which is the result for the tunneling current of an ideal STM tip that would consist of a mathematical point source [42]. In that case any contributions to the matrix element are proportional to the amplitude of ψ_ν at the tip. Within this approximation the STM simply measures $\rho(\vec{r}_t, E_\mathrm{F})$ – the local density of states (LDOS) at E_F, that is the charge density from states at the Fermi level, for the bare surface at the position of the tip.

In summary the contrast in STM images is always a result of the convolution of the electronic structure of the sample, the tunneling barrier function and to a certain extend the electronic structure of the tip. A nice example are the STM images of a few Fe atoms on Cu(111) displayed in Figure 2.1b. Here Crommie *et. al* deposited a small amount of Fe atoms on a clean Cu(111) surface at $T = 4\,\mathrm{K}$ and subsequently moved single Fe atoms with the tip of the STM to form a ring of about 143 Å diameter containing 48 Fe atoms. The final STM image shows the Fe atoms as very high objects on top of the Cu(111) surface. In addition strong circular modulations of the topography inside the diameter of the ring and weak modulations outside of the ring are

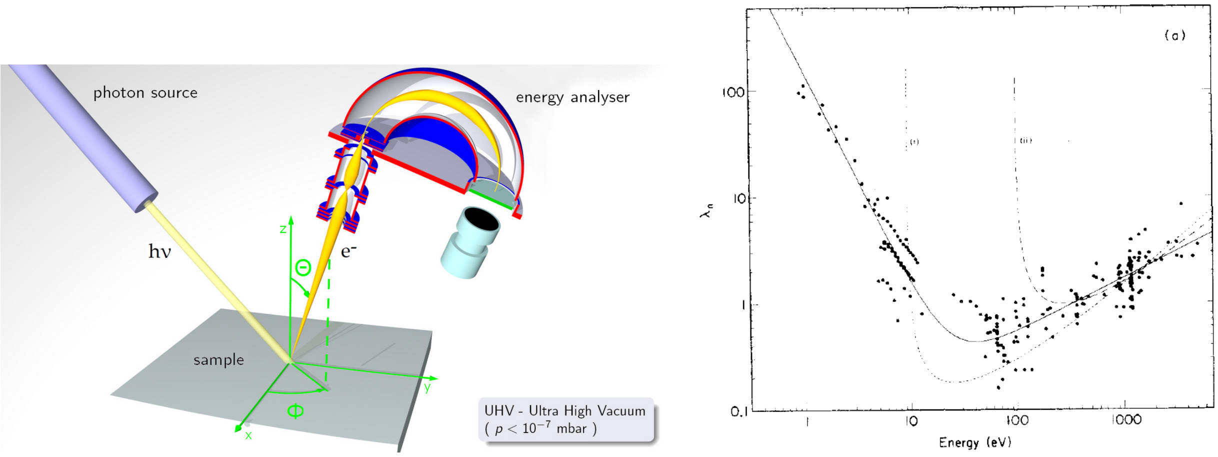

(a) Schematic drawing of an experimental setup to measure angle resolved photoelectron spectroscopy (from http://en.wikipedia.org/wiki/ARPES).

(b) Compilation of inelastic mean free path measurements $\lambda(\mathrm{nm})$ from [48]

Figure 2.2: Schematics of an angle resolved photoelectron spectroscopy setup and electron inelastic mean free paths in solids demonstrating the surface sensitivity of the method.

observed. These modulations are solely a density of states effect and not related to true topography. What can be seen are standing wave interference patterns of the surface state electron wave functions scattering at the barrier produced by the Fe atoms.

For a more detailed insight into the theory and applications of STM the reader is referred to one of the comprehensive textbooks (e.g. Ref. [44]). Therein one can also find a qualitative theory for tunneling spectroscopy that is for modest bias voltages. For those a qualitative generalization of Tersoff and Hamann results in

$$I(V) \propto \int_{E_\mathrm{F}}^{E_\mathrm{F}+V} \rho(E)T(E,V)dE,$$

with the so called barrier transmission coefficient $T(E,V)$.

2.2 Photoelectron spectroscopy

Photoelectron spectroscopy (PES) is based on the photoelectric effect which has been discovered in 1887 by Hertz[45] and theoretically described by the postulation of the quantum nature of light in 1905 by Einstein [46]. For the latter Einstein received the Nobel price in Physics in 1921[2]. As a standard work for PES the textbook by Hüfner [47] is recommended.

When light of a given energy $h\nu$ impinges on a gas or the surface of a solid photoelectrons are created and can escape into the vacuum. Their kinetic energy E_{kin} is given as the difference of the photon energy, the sample work function ϕ and their binding energy E_B prior to the excitation

---

[2] http://nobelprize.org/nobel_prizes/physics/laureates/1921/

process

$$E_{kin} = h\nu - \phi - |E_B|. \tag{2.1}$$

In PES the binding energy of an electron in a solid is usually referred to the Fermi level and given as a positive number. For free atoms or molecules it is referred to the vacuum level E_{vac}. The momentum p of the photoelectron in vacuum can be determined from its kinetic energy by

$$p = \sqrt{2mE_{kin}}.$$

The direction of $\vec{p}$ is inferred from the polar angle ϑ and the azimuthal angle φ under which the photoelectron leaves the surface. In a real experiment the kinetic energy of the photoelectrons in vacuum is measured with an electrostatic analyzer with a small acceptance angle in order to simultaneously determine the emission angles (ϑ, φ) (see Fig. 2.2a). To avoid scattering of the photoelectrons on their way to the analyzer ultra-high vacuum (UHV) is required. Thereby their mean free path increases to a few meters but at the same time the effort that has to be put on the experimental side multiplies.

Because of frequent electron-electron and electron-phonon collisions electrons have a very short inelastic mean free path λ inside the solid. This is the distance which they can travel without loosing energy through a scattering process. The inelastic mean free path depends on the kinetic energy of the electrons and with the exception of a few cases electron-phonon scattering only plays a role at very low energies. The inelastic mean free path overlaps with the general relation

$$\lambda = \frac{143\,\mathrm{nm}\cdot\mathrm{eV}^2}{E^2} + 0.054\,\mathrm{nm}\cdot\mathrm{eV}^{-1/2}\sqrt{E}$$

for most elements [48] (see Fig. 2.2b). From this relation it becomes obvious that for usual electron kinetic energies in a PES experiment ($E_{kin} \gtrsim 5\,\mathrm{eV}$) the inelastic mean free path is smaller than 10 nm which makes the method very surface sensitive since only electrons originating from the first ~ 50 ML of the sample can be measured. This always has to be taken into account when statements about the bulk properties of a solid are derived from the results of a PES experiment (the same holds true for all other surface sensitive methods like e.g. STM).

2.2.1 X-ray photoelectron spectroscopy

Using x-rays ($h\nu > 200\,\mathrm{eV}$) for PES even photoelectrons from the low lying core levels of heavy elements can be excited. The energy distribution of the density of states for the core electrons (i) in a solid resembles a sum of delta functions $\mathrm{DOS}(E) = \sum_i a_i \delta(E - E_{b,i})$ and is unique for each individual element. Upon excitation of a core electron a core hole ($q = +e$) is created. This core hole interacts with the remaining electrons and the excited photoelectron and leads to a modification of the kinetic energy distribution of the photoelectron intensity $I(E_{kin})$ which is to be measured. In addition the nonzero spectral linewidth of the excitation source as well as the finite experimental energy resolution lead to a further broadening of the photoelectron

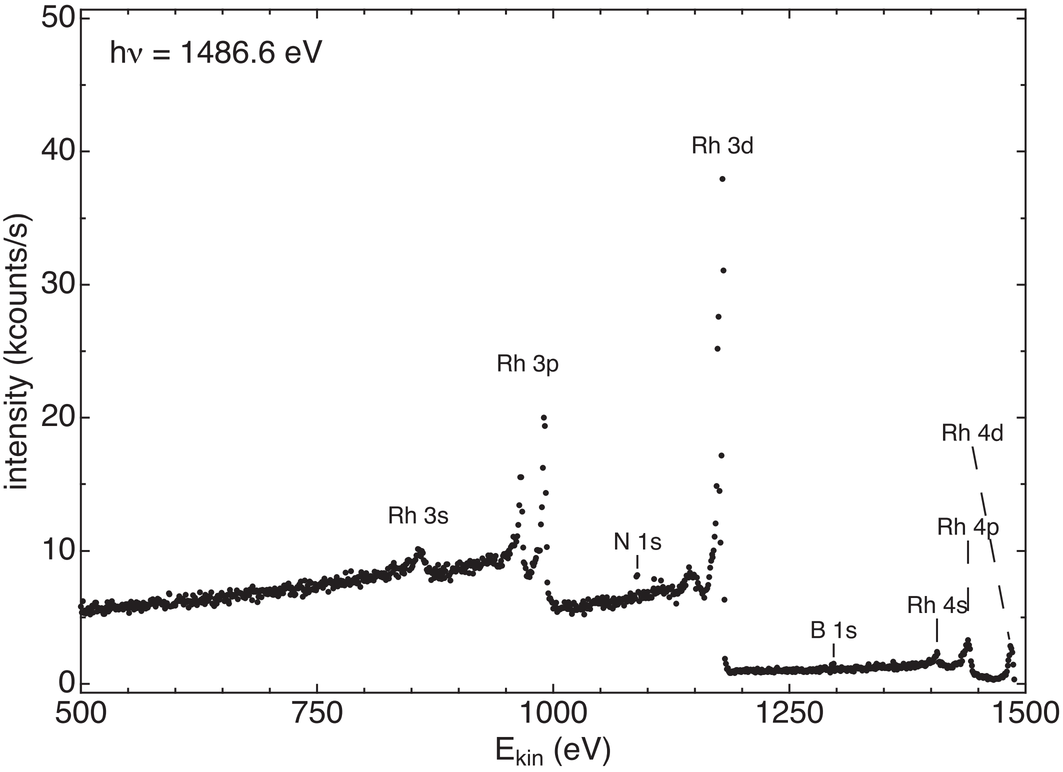

Figure 2.3: Experimental photoelectron spectrum of *h*-BN/Rh(111) excited with monochromatized Al K_α x-rays.

intensity peak and secondary electrons. These electrons which scatter inelastically on their way to the sample surface, result in a background signal increasing to the low kinetic energy site of the photoelectron spectrum. Nevertheless this processes are sufficiently well known in order to conclude on the chemical composition of an investigated sample from the recorded photoelectron intensity distribution (ESCA: Electron Spectroscopy for Chemical Analysis). An example for ESCA is given in Figure 2.3. It shows a x-ray photoelectron spectrum of a Rh(111) surface covered with a single layer of *h*-BN.

2.2.2 X-ray photoelectron diffraction

While traveling to the crystal surface the photoelectron is scattered at the periodic crystal potential. This scattering leads to wavelength and crystal orientation dependent intensity modulations of the final-state electron wave function. One method to measure this modulations is the so called x-ray photoelectron diffraction (XPD) which can experimentally be realized by measuring the intensity of the emitted photoelectrons for a fixed kinetic energy at all angles (ϑ, φ) of the upper hemisphere above the crystal surface.The thereby obtained intensity pattern is usually displayed in polar coordinates as a stereographic projection for which the radial coordinate r is almost linear in ϑ for $\vartheta = 0 - \pi/2$ (see Chap. A). This diffraction pattern contains information about the atomic structure of the system under investigation. In order to model the diffraction process the photoelectron beam in vacuum is regarded as being a superposition of the primary photoelec-

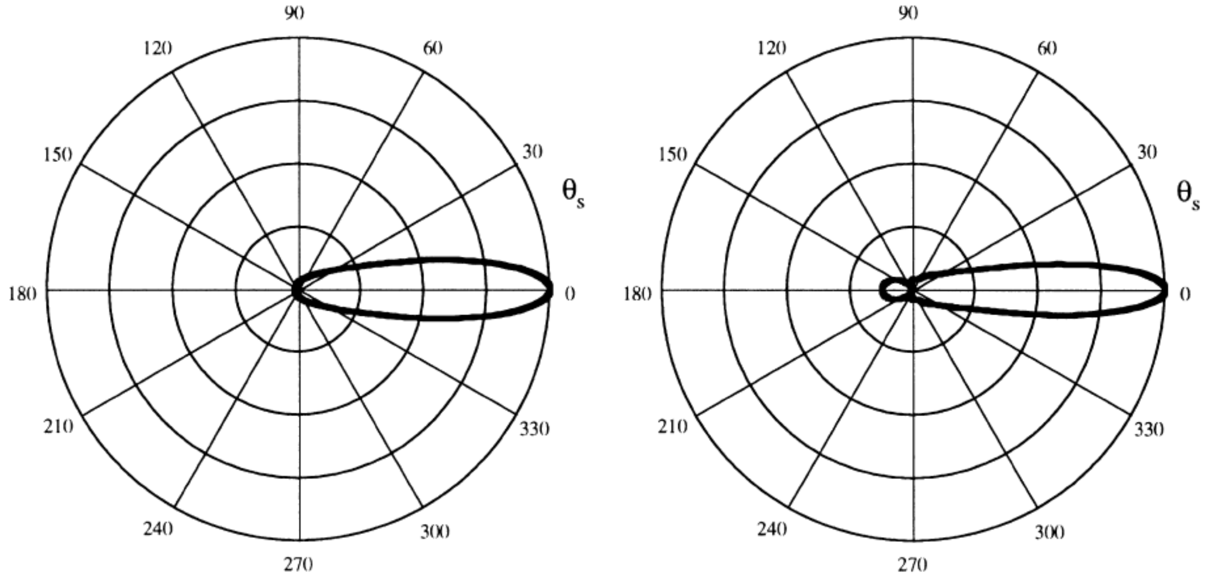

Figure 2.4: Form factor $f(\theta_s)$ for the scattering of a plane electron wave with $E_{kin} = 723\,\mathrm{eV}$ off an oxygen atom (left) and off a rhodium atom (right) (from Ref. [49]).

tron wave, originating from the site of the photoemission process, and the elastically scattered photoelectron waves originating from the ions surrounding the primary emission site. Often it is sufficient to only take single scattering events and a manageable amount of surrounding ions into account which is then referred to as single-scattering cluster (SSC) calculations. The fact that the scattering amplitude for high energy photoelectrons ($E_{kin} \gtrsim 300\,\mathrm{eV}$) has a strong asymmetry showing an enhancement into the forward direction ($\theta_s = 0$) (Fig. 2.4) makes the interpretation of the main features of XPD patterns from single crystalline surfaces straight forward: A high photoelectron intensity may be expected in directions which connect both – the emitter and one or more scatterer (Fig. 2.5). This makes XPD a powerful tool for the investigation of the atomic structure of surfaces or adsorbate-surface systems [50].

With a variation of this experimental technique which is often referred to as photoelectron diffraction (PED) bond lengths in crystals and molecules can be inferred. There the geometry of incident light, sample and analyzer is kept fix but the photon energy is varied which requires the use of synchrotron radiation.

2.2.3 Ultraviolet photoelectron spectroscopy

In metals and semiconductors some of the valence electrons of the ions which constitute the crystal experience a very low energy barrier for hopping to neighboring atoms. These electrons account for the electron transport in those materials. However the valence electrons may not move without restriction. Valence electrons with a given wave vector $\vec{k}$ may only be found at certain energies $E(\vec{k})$. This energy dispersion relation is also known as the band structure and can be measured with angle-resolved ultraviolet photoelectron spectroscopy (ARUPS). Valence band photoelectron spectroscopy is achieved using photons of lower energy (typically in the

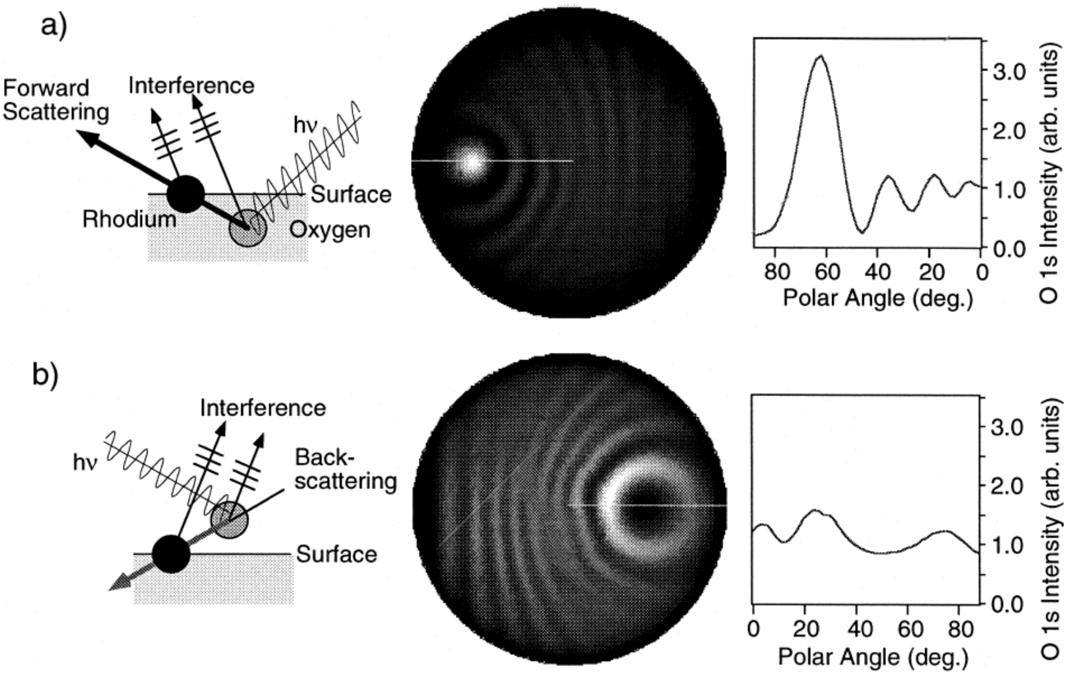

Figure 2.5: Scattering geometries (left), full XPD patterns of single-scattering cluster calculations (middle) and azimuthal cuts along the white lines in the SSC patterns (right) for O 1s emission at $E_{kin} = 723\,\text{eV}$ for a) subsurface oxygen on rhodium and b) adsorbed oxygen on rhodium (from Ref. [49]).

visible or UV range $h\nu \sim 5 - 100\,\text{eV}$) than for core level spectroscopy as excitation source. This results in valence band photoelectrons which have a similar kinetic energy. Thus a much better energy resolution ΔE than in x-ray photoelectron spectroscopy (XPS), where electron kinetic energies in the range of about $100 - 2000\,\text{eV}$ ought to be measured, can be reached. Through Eqn. (2.1) we can determine the energy E of the electrons inside the solid. In order to obtain their wave vector $\vec{k}$ we have to take a close look at the complete photoemission process. There are several models describing the photoemission process. For example the *one-step model* which is often regarded as the correct model and the phenomenological *three-step model* [51] which is much easier to understand and still proved to be very successful. In the three-step model the photoemission process is divided into three steps:

- *First* an electron in the initial state $|i\rangle$, a Bloch state which is defined by its energy E_i, wave vector $\vec{k_i}$ and spin σ_i, is excited by an impinging photon into an unoccupied final state $|f\rangle$. The energy of the final state is given by $E_f = E_i + h\nu$. Since the momentum of the photons in the energy range used for UPS is negligible compared to the electron's momentum only direct or vertical transitions in a reduced zone scheme are allowed. The wave vector of the photo-excited electron in the solid thus is $\vec{K} = \vec{k_f} = \vec{k_i} + \vec{G}$ where $\vec{G}$ denotes a reciprocal lattice vector.
- *Second* this final state electron $|f\rangle$ travels through the crystal. Usually a free-electron final state is used to describe the propagation of the electron through the crystal ($E_f = \hbar^2 k^2/2m$).

Electron-electron scattering leads to the production of secondary electrons and reduces the number of photo-excited electrons reaching the surface.

- *Third* the final state electrons $|f\rangle$ can be transmitted into the vacuum. Thereby they have to overcome the surface potential barrier V_0 which costs energy and leads to refraction at the solid–vacuum boundary. For that reason the momentum of the photoelectrons in vacuum $\vec{p}$ does not equal $\hbar\vec{K}$. Nevertheless the parallel momentum $\vec{p}_{\|}$ is conserved and

$$\begin{aligned} \frac{|\vec{p}_{\|}|}{\hbar} = K_{\|} &= \frac{\sqrt{2m}}{\hbar}\sqrt{E_{kin}}\sin\vartheta \\ &= \frac{\sqrt{2m}}{\hbar}\sqrt{E_{kin}^{solid}}\sin\vartheta^{solid}, \end{aligned} \tag{2.2}$$

where E_{kin} and ϑ are the measurable quantities in a real photoemission experiment while E_{kin}^{solid} and ϑ^{solid} are properties of the photo-excited electrons inside the solid. Through the relation $E_{kin} = E_{kin}^{solid} - V_0$ Snell's law for the refraction of the photoelectrons at the solid–vacuum interface

$$\sin\vartheta = \sin\vartheta^{solid}\sqrt{\frac{E_{kin}+V_o}{E_{kin}}}$$

as well as an equation for the indirect determination of the perpendicular electron momentum

$$k_{\perp} = \frac{\sqrt{2m}}{\hbar}\sqrt{E_{kin}+V_o}\sin\vartheta^{solid} \tag{2.3}$$

can be derived. Unfortunately the inner potential V_o may not be measured and can only be determined by comparison of calculated and measured band structures.

In conclusion by combining Eqns. (2.1) and (2.2) we can establish the band structure $E(K_{\|})$ along a certain sample azimuth φ through measuring E_{kin} and (ϑ,φ). In ARPES it is common to display Eqn. (2.2) in a form which is more handsome for the every day use namely

$$K_{\|}(\text{Å}^{-1}) = 0.5123\,\text{Å}^{-1}\sqrt{E_{kin}(\text{eV})}\sin\vartheta.$$

From Eqn. (2.2) it is also obvious that band structure measurements with x-rays are hardly possible since the angular acceptance $\Delta\vartheta$ of the electron analyzer of about 2° leads to a final state wave vector K that is smeared out over the whole Brillouin zone due to the high kinetic energy of the photoelectrons [$\Delta K_{\|} = 0.51\,\text{Å}^{-1}\sqrt{E_{kin}(\text{eV})}\cos\vartheta\,\Delta\vartheta$].

2.3 Photoemission of adsorbed xenon

As already discussed photo-excited electrons have to overcome the work function of a surface in order to be promoted into the vacuum. This work function φ_c may be heterogeneous above a sample surface. The mean value ϕ of the sample work function can be determined by the width

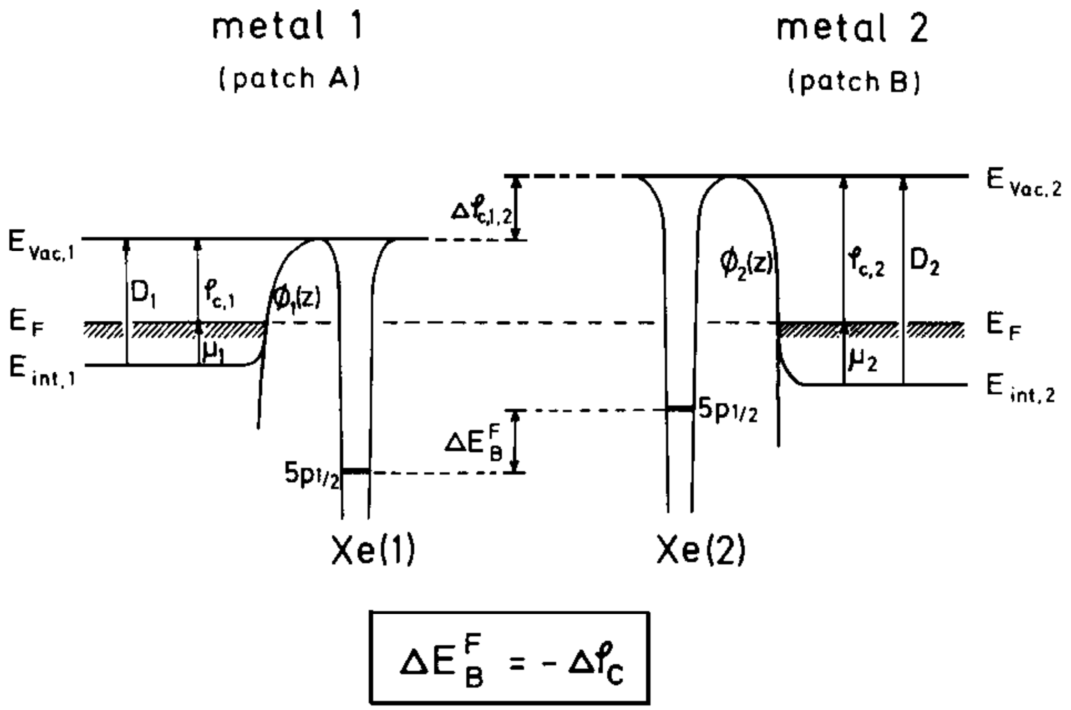

Figure 2.6: Potential energy diagram for the photoemission of adsorbed xenon (from Ref. [53]).

ΔE of the photoemission spectrum: $\phi = h\nu - \Delta E$. In an experimental photoemission setup the measured sample is usually connected to ground which results in an alignment of the absolute position of the Fermi levels E_F for all metallic samples. For surfaces possessing different work functions $\varphi_{c,i}$ this immediately leads to different vacuum levels $E_{vac,i}$. A photoemission method to determine the position of the vacuum level with respect to the Fermi level is given by the PAX [52, 53].

Figure 2.6 depicts a potential energy diagram for the xenon adsorbed on a metal surface. The electrostatic potential experienced by any charge which is brought from infinity through the surface to the bulk is given by the curve $\Phi(z)$ connecting the vacuum level E_{vac} outside the surface with the potential E_{int} inside the metal. The surface contribution $D = E_{vac} - E_{int}$ to the total work function φ_c extends only about 2 Å beyond the metal surface. However for xenon adsorbed on metal surfaces Xe–metal spacings of $Z > 3$ Å have been derived by LEED. As an immediate consequence the electrostatic potential of the Xe atom aligns to the same level as in the gas phase – the vacuum level E_{vac}. This explains the invariance of the Xe ionization potential as it had been observed for many different metals and more important provides easy access to the variation of the work function $\Delta\varphi_{c,1,2} = \varphi_{c,2} - \varphi_{c,1}$ be that above a heterogeneous surface or above different surfaces. $\Delta\varphi_{c,1,2}$ is directly reflected in the binding energy difference of the core levels of Xe above different work function regions as referred to the Fermi level $\Delta E^\mathrm{F}_{\mathrm{B},1,2} = -\Delta\varphi_{c,1,2}$

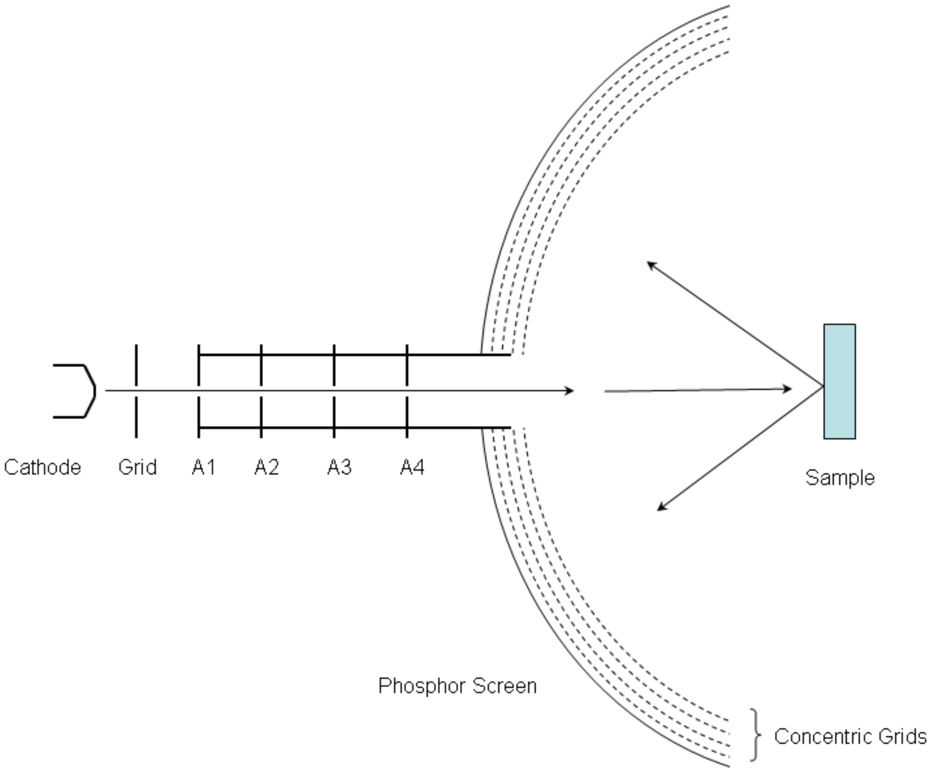

Figure 2.7: Schematic representation of a LEED setup (from `http://en.wikipedia.org/wiki/Low-energy_electron_diffraction`).

2.4 Low energy electron diffraction

The de Broglie wavelength $\lambda = h/p = h^2/\sqrt{2mE_{kin}}$ of electrons of mass m with kinetic energies E_{kin} in the range of $10-1000\,\mathrm{eV}$ lies in the order of $500-50\,\mathrm{pm}$. Since this is smaller than the inter-atomic distances in condensed matter interference among electrons having that low kinetic energies and being elastically scattered at periodic crystal lattices occurs. The small inelastic mean free path of these electrons ($50-500\,\mathrm{pm}$ [48]) leads to the huge surface sensitivity of the method. Directions under which constructive interference is observed can be deduced from the Bragg diffraction condition. The geometric construct of the Ewald sphere is also applicable to LEED but due to the quasi two-dimensionality of the investigated sample (stemming from the low penetration depth) the reciprocal lattice evolves from points to rods which are aligned parallel to the surface normal. Therefore diffraction patterns may always be observed as soon as the radius of the Ewald sphere reaches a value which equals the distance of two such rods in reciprocal space.

The experimental setup for LEED is depicted in Figure 2.7: Electrons are emitted from a hot filament and accelerated towards the sample surface by an electron gun. The diffracted electrons are energy selected by several concentric grids floating on different potentials. Finally they are accelerated onto a fluorescent screen using high voltage.

LEED is an ideal tool for the investigation of surface reconstructions, the classification of periodic surface structures, the confirmation of superlattice formations and as a check of surface cleanliness and roughness. Through analyzing the energy dependent intensity variations of individual diffraction spots [LEED-I(V)] even structure information for the third dimension – perpendicular to the surface – can be made accessible. A more detailed introduction into the method is given in Ref. [54].

2.5 Thermal desorption spectroscopy

thermal desorption spectroscopy (TDS) is a formidable method to investigate thermally activated desorption processes on surfaces. In TDS a temperature ramp with a constant heat rate β is programmed for the sample and than either a spectroscopic feature of the system under investigation is monitored during the temperature increase (e.g. using UPS) or the desorbing species are directly measured with a mass spectrometer. If for the latter a well-defined relation between the density of particles n_i as measured with the mass spectrometer ($n_i \propto I_i$) and the partial pressure p_i of this species can be found, which for most light gases is the case, the amount of desorbed particles N_i can be determined from the area under the TDS curve and the pumping speed S of the chamber:

$$\begin{aligned} N_i &= \frac{S}{k_\mathrm{B}T}\int_{t_0}^{t_1} p(t)dt \\ &= \frac{S}{k_\mathrm{B}T}\frac{1}{\beta}\int_{T_0}^{T_1} p(T)dT. \end{aligned}$$

A more detailed introduction into desorption from surfaces is given in the textbook by M. Henzel and W. Göpel [55]. There also a description of the different orders of desorption is given.

Chapter 3

Results and Discussion

The following chapter is a modified version of the accepted manuscript of:
T. Brugger, S. Günther, B. Wang, J. H. Dil, M.-L. Bocquet, J. Osterwalder, J. Wintterlin, and T. Greber, *Comparison of electronic structure and template function of single-layer graphene and a hexagonal boron nitride nanomesh on Ru(0001)*, Physical Review B **79**, 045407 (2009), DOI: 10.1103/PhysRevB.79.045407.

3.1 Comparison of *g*/Ru and *h*-BN/Ru

A single layer of an adsorbate strongly influences the physical and chemical properties of a surface. Sticking and bonding of atoms and molecules may change by orders of magnitude as well as the transport properties across and parallel to the interface. For developments in nanotechnology it is particularly useful to have single layer systems which are inert, remain clean at ambient conditions and are stable up to high temperatures. In this field sp^2 hybridized graphene and hexagonal boron nitride are outstanding examples [13, 20]. On ruthenium both form perfect single layers, where the lattice mismatch between the substrate and the adsorbate causes two dimensional regular super structures with a lattice constant of about 3 nm [21–23, 56]. The peculiar functionality as a template for trapping molecules which had been found in the case of the *h*-BN/Rh(111) nanomesh [26, 27] might also be valid for *g*/Ru(0001), although experimental demonstrations on this issue are missing so far.

The purpose of this section is to establish a comparison between *g*/Ru(0001) and *h*-BN/Ru(0001) in view of the electronic structure and functionality as a template. For this purpose, photoemission and DFT are used. It is shown that *g*/Ru(0001) is a metal with a sizeable Fermi surface, while *h*-BN/Ru(0001) is not. The exploration of the electrostatic potential energy landscape by PAX also indicates a modulation of the local work function for *g*/Ru(0001), analog to the *h*-BN/Rh(111) nanomesh [27] and a concomitant template function. However, the different topography of the two systems also proposes complementary functionality.

The lattice mismatch $\mathfrak{M}$ of the laterally rigid sp^2 networks graphene and hexagonal boron nitride on different transition metals leads to super structures with lattice constants in the sp^2 layer of

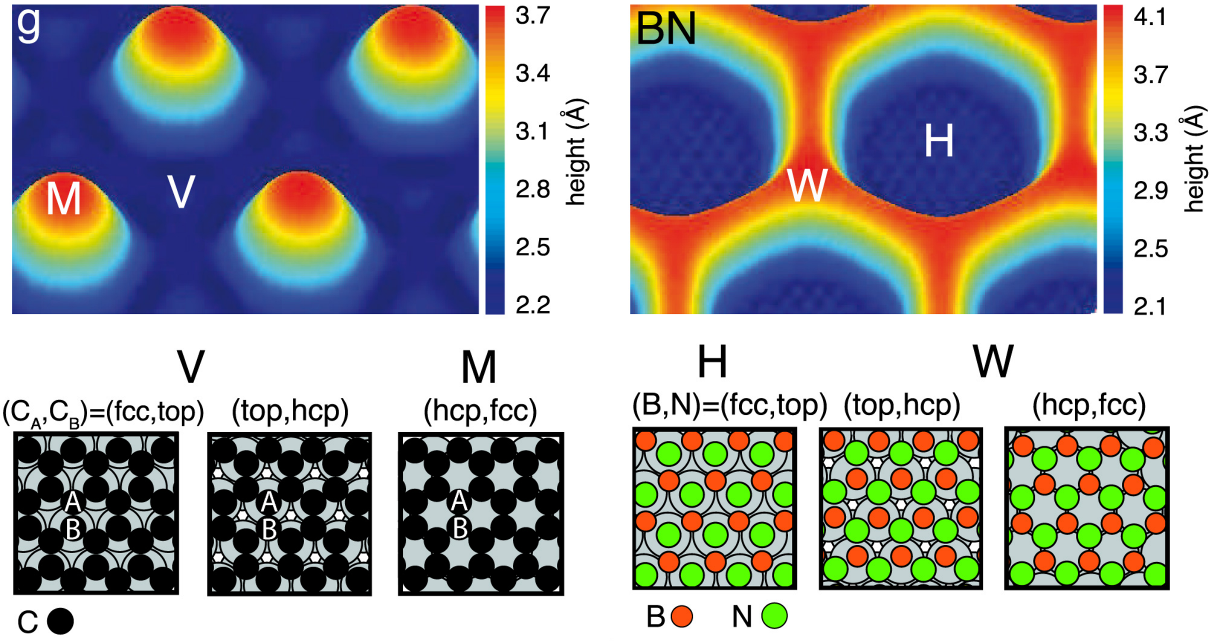

Figure 3.1: Views of the height modulated graphene (*g*) and *h*-BN nanomesh (BN) on Ru(0001), as obtained from a DFT calculation for both systems. *M* and *V* denote mounds and valleys of the graphene, H and W holes and wires of the *h*-BN nanomesh. The six ball model panels illustrate the three different regions [(fcc,top), (top,hcp) and (hcp,fcc)] which can be distinguished in both systems (see text).

$a_{\mathrm{sp}^2}/\mathfrak{M}$, where a_{sp^2} is the (1×1) lattice constant of graphene and *h*-BN, of about 0.25 nm [1]. Together with the coordination dependent bond strength of the adsorbate atoms to the diverse transition metal substrate atoms this leads to distinct atomic structures [18, 20–24, 56–61]. The SXRD data which are presented in Figure 3.2 show that for graphene on Ru(0001) 25 × 25 graphene unit cells coincide with 23 × 23 Ru units [62]. This large unit cell splits into four subunits of 12.5 × 12.5 *g* on 11.5 × 11.5 Ru cells. Each subunit corresponds to one wavelength of the corrugation of the graphene overlayer. For *h*-BN/Rh(111) 13 × 13 BN units coincide with 12 × 12 Rh units [20, 30] and for *h*-BN/Ru(0001) 14 × 14 BN units on 13 × 13 Ru units are found [63]. Whereas *h*-BN has a base with two different atoms in the unit cell, the base of graphene consists of two identical carbon atoms C_A and C_B which become distinguishable by the local coordination to the substrate (Fig. 3.1). In *g*/Ru the local (fcc,top) and (top,hcp) coordination leads to close contact between the (C_A,C_B) atoms and the substrate [64] while (B,N) is strongly interacting only in the (fcc,top) coordination [35]. As a result, twice as many atoms are bound in strongly interacting regions in *g*/Ru when compared to *h*-BN/Ru. In the following we call the strongly bound region of *g*/Ru(0001) valley (*V*) and the weakly bound region with the (C_A,C_B) atoms on (hcp,fcc) sites mounds (*M*). The fact that (top,hcp) leads to strong bonding for graphene but weak bonding for *h*-BN gives rise to an inverted topography of the two layers: a connected

---

[1] The lattice mismatch $\mathfrak{M}$ is defined as the relative difference $\left(a_s - a_{\mathrm{sp}^2}\right)/a_s$ between the substrate in plane lattice constant a_s and the sp^2 network lattice constant a_{sp^2}.

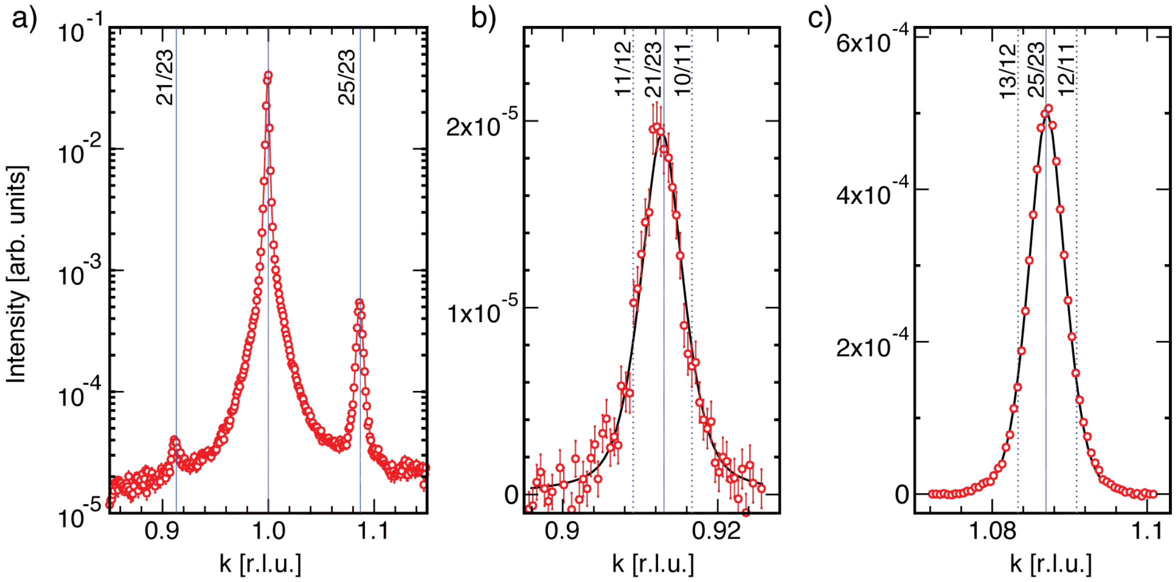

Figure 3.2: SXRD data of g/Ru(0001). a) In-plane scan along the k direction in the neighborhood of the $(h = 0, k = 1)$ crystal truncation rod (CTR) of Ru at $l = 0.4$ r.l.u. b) and c) High-resolution scans across the superstructure signal of g/Ru(0001), detailing the 25-on-23 reconstruction. The data were fit to a pseudo-Voigt profile (solid black curves). The positions where 13-on-12 and 12-on-11 reconstruction diffraction signals would lie are indicated by the dotted lines [62].

network of strongly bound regions for graphene (valley) and a connected network of loosely bound regions for h-BN (wires).

The height in Figure 3.1 corresponds to the theoretical results. It is the distance of the overlayer atoms from the average position of the first Ru layer. The value for h-BN nanomesh on Ru(0001) is larger than the presently accepted experimental value of about 0.5 Å [21] and the theoretical value of 0.55 Å for h-BN nanomesh on Rh(111) [28]. For the case of g/Ru STM indicates bias dependent mound heights of $0.7 - 1.1$ Å [23] and $0.2 - 1.0$ Å [56, 65, 66]. These quantitatively conflicting results indicate how difficult the complete description of the sp^2 layers with different bonding regimes is. It has for example to be expected that van der Waals bonding which is important for the mounds of g/Ru and the wires of h-BN/Ru is less well described by DFT than the strongly bound regions. We emphasize that theory predicts the correct shape of the sp^2 layer corrugations while the absolute values of the heights that are reflected in the band splittings and the electrostatic potential corrugation are too large if compared with the experiment. The SXRD structure determination of g/Ru(0001) [62] relied on the theoretical results of the graphene corrugation [64], but the observed strong intensity oscillations in the superstructure rods along l demonstrated that the Ru substrate is also considerably corrugated. This is a result of the strong interaction between g and Ru in the valley of the g/Ru unit cell. A recent structural analysis of this SXRD data which contains a fit to Fourier-series expanded displacement fields from the ideal bulk structure finds a chiral displacement of the C atoms on the hills of the graphene layer which breaks the mirror symmetry of the unit cell [67]. An unambiguous experimental sp^2 layer corrugation determination by structural methods will involve low-energy electron diffraction (LEED) [68], atomic force microscopy or He diffraction.

3.1.1 Theory

Ab initio calculations were performed with the VASP package based on DFT, which implements PAW pseudopotentials [69] and the PBE exchange correlation functional in the Generalized Gradient Approximation (GGA) [70]. The structural calculations of *g*/Ru were performed with a (12×12) *g* on (11×11) Ru supercell. It was tested that the results for a (13×13) *g* on (12×12) Ru supercell were very similar, so that the actual (12.5×12.5) *g* on (11.5×11.5) Ru supercell must be well described, too. For *h*-BN/Ru a (13×13) BN on (12×12) Ru supercell was used. One layer of *g* (BN) on a three layer Ru slab with the *g* (BN) layer and the first Ru layer relaxed was investigated. The effective vacuum region was larger than 7.5 Å. For the band structure calculations epitaxial (1×1) *g* or BN/Ru structures were investigated with the lattice constant of graphene kept fixed at the calculated value for free standing graphene, a 4-layer Ru slab with the lattice constant adjusted, a $36 \times 36 \times 1$ *k*-sampling and 400 eV cutoff [2]. The electrostatic potential calculation has been performed with one *g* layer on both sides of a five layer Ru slab with the same lateral periodicity as for the structural calculations and the vertical positions as they result from the latter. The whole supercell had a vertical height of 50 Å leading to an effective vacuum region larger than 30 Å.

3.1.2 Results and discussion

The hybridization of the carbon p_z orbitals with the substrate atoms breaks the symmetry between the C_A and the C_B atoms. This is reflected in the band structure where a large π-band gap opens at $\overline{K}$. Figure 3.3(a) shows the measured band structure for *g*/Ru(0001) along $\overline{\Gamma K}$. At $\overline{K}$ the π-band levels off at a binding energy of 4.6 ± 0.1 eV. This strong hybridization is in line with observations on *g*/Ni(111) [11]. The experiment is in good agreement with calculations for a (1×1) graphene sheet 2.2 Å above the topmost Ru layer with $(C_A,C_B)\sim$(top,hcp) [Figure 3.3(b)]. Calculations with $(C_A,C_B)\sim$(hcp,fcc) 3.7 Å above the Ru top layer result in a shift of the carbon derived bands to lower binding energies. The π- and π^*-bands get connected with Dirac cones at $\overline{K}$, as it is expected for freestanding graphene [71] [Figure 3.3(c)]. The experiment does however not indicate a π-band splitting, that is two different π-bands for low and high graphene. With a recent paper on a C 1s core level splitting as measured with XPS in *g*/Ru(0001) [24] that was assigned to the high and low regions, this suggests that the high regions are electronically linked

---

[2] For the calculation of the band structure of the (1×1) models we found it more suitable to fix the graphene lattice at the relaxed value of the free-standing layer (and adjust the Ru substrate accordingly) because the band width sensitively depends on the small strains of the graphene lattice. The Dirac point on the weakly interacting *M* regions [Figure 3.3(c)] is then slightly above E_F (p doping). In the opposite case, when the Ru lattice is kept at the relaxed value of the bare surface and the graphene is adjusted (as in Reference [64]), the Dirac point moves below E_F (n doping).

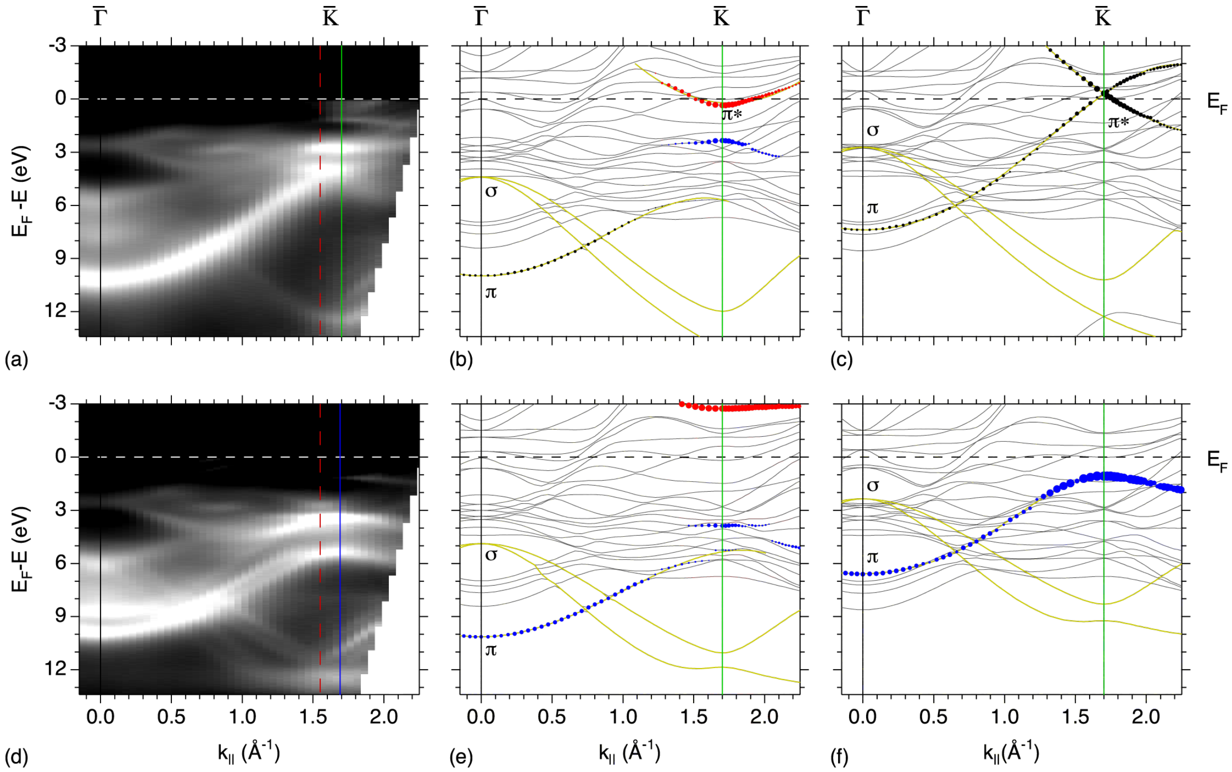

Figure 3.3: Band structures of graphene and *h*-BN nanomesh on Ru(0001) along $\overline{\Gamma K}$. (a) He II$_\alpha$ photoemission of *g*/Ru(0001). [(b) and (c)] DFT of *g*/Ru(0001) for the low [(C_A,C_B)∼(top,hcp)] and high [(C_A,C_B)∼(hcp,fcc)] regions, respectively. (d) He II$_\alpha$ photoemission of *h*-BN/Ru(0001). [(e) and (f)] DFT of *h*-BN/Ru(0001) for the low [(B,N)∼(fcc,top)] and high [(B,N)∼(hcp,fcc)] regions, respectively. The vertical lines at $\overline{K}$ indicate the boundaries of the 1 × 1 surface BZs for Ru (red dashed), *h*-BN (blue solid) and graphene (green solid). The size of the filled circles in (b), (c), (e) and (f) represents the p_z weight of the adsorbate atoms on the bands, where blue describes C_A (top) in (b) and N in (e) (top) and (f) (fcc). Red describes hollow site atoms [C_B in (b) and B in (e)]. Black circles depict the average of the two inequivalent adsorbate atoms. Thick yellow curves are guides for the eyes.

to the low regions in a way that hampers the free graphene picture as it emerges in Figure 3.3(c). The same section of *k*-space for *h*-BN/Ru(0001) is shown in Figure 3.3(d). The π-band levels off at a binding energy of 5.4 ± 0.1 eV. Calculations for a (1 × 1) (B,N)∼(fcc,top) sheet 2.2 Å above the topmost Ru layer describe the global characteristics of the σ-bands and the π-band of *h*-BN on Ru well [Figure 3.3(e)]. For the case of *h*-BN nanomesh a π-band splitting is observed in experiment and theory [Figure 3.3(d)-(f)], which is also consistent with the N 1s core level splitting [72]. This signifies an intriguing and important difference between graphene and *h*-BN nanomesh on Ru(0001), and is proposed to lie in the difference in atomic and electronic structure (see below). Theory additionally shows that the two atoms in the base of the sp^2 networks have a different p_z weight on the different bands. For the case of *h*-BN in the close contact region (holes) the π-band is mainly nitrogen derived, while the unoccupied π*-band has its main weight on the boron atoms. For graphene in the low region (valley) only the C_B atom contributes to

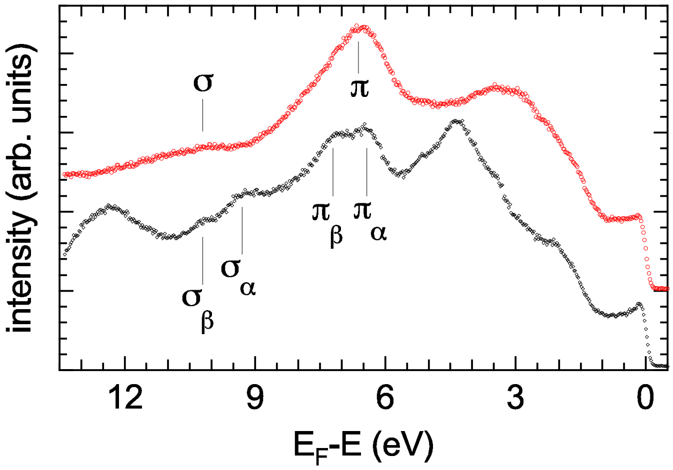

Figure 3.4: He II_{α} energy distribution curves at $k_{\parallel} = 1.12\,\mathring{\mathrm{A}}^{-1}$ for graphene (red open circles) and *h*-BN nanomesh (black open diamonds) on Ru(0001) extracted from the band structure data of Figures 3.3(a) and (d), respectively. The curves are vertically offset for clarity.

the π^*-band close to $\overline{\mathrm{K}}$ while the π-band has equal portions from top and hollow site atoms. The effect of p_z-d, that is C(N)-Ru hybridization is reflected in the close contact regions (valley and holes) by states in the π-band gap that are mainly $\mathrm{C_A}$(N)-Ru derived. In the case of the high regions of graphene (mounds) the two carbon atoms are degenerate again and consequently $\mathrm{C_A}$ and $\mathrm{C_B}$ contribute in equal measures to the π-band. For the loosely bound BN (wires) the nitrogen and the boron atoms determine the π- and the π^*-band, respectively.

A distinct difference between graphene and *h*-BN nanomesh is the band splitting of 0.8 eV for the BN bands that belong to the 'wires' (σ_α and π_α) and the 'holes' (σ_β and π_β), respectively [Figures 3.3(d) and 3.4]. The band splitting of *h*-BN was assigned to the dielectric nature of *h*-BN and the local work function difference between the 'hole' and the 'wire' regions [21]. For graphene no splitting is observed, where a splitting smaller than 310 meV could not be resolved by the experiment [Figures 3.3(a) and 3.4]. This can be explained by a smaller corrugation of the graphene layer or by the metallic nature of graphene. Although both systems are corrugated isoelectric sp^2 networks where atoms reside in two different vertical positions (low and high regions) which leads to distinguishable core level binding energies, this turns out to be not sufficient to conclude on an equivalent valence band structure of *g*/Ru and *h*-BN/Ru.

The metallicity of *g*/Ru(0001) is reflected in the measured FSM which is compared to that of *h*-BN/Ru(0001) in Figure 3.5. The FSM of *h*-BN/Ru(0001) shows only bands that are also seen on the bare Ru(0001) surface (data not shown). On the other hand, *g*/Ru(0001) displays states at the Fermi level that are reminiscent to the Dirac points at the $\overline{\mathrm{K}}$ points of free standing graphene [71]. The band structure measurements in Figure 3.3(a) demonstrate that these graphene related states are part of the π^*-band, which means that charge is transferred from the substrate to the graphene. The Luttinger volume of the electron pockets near $\overline{\mathrm{K}}$ corresponds to the number of transferred electrons $N_e = 2\pi/\left(3\sqrt{3}\right)\left(\Delta\phi_{\overline{\mathrm{K}}}\right)^2$, where $\Delta\phi_{\overline{\mathrm{K}}}$ is taken as the full width at half maximum of the intensity on an azimuthal cut across $\overline{\mathrm{K}}$, in radians [Figure 3.5(c)]. For the FSM in Figure 3.5(a)

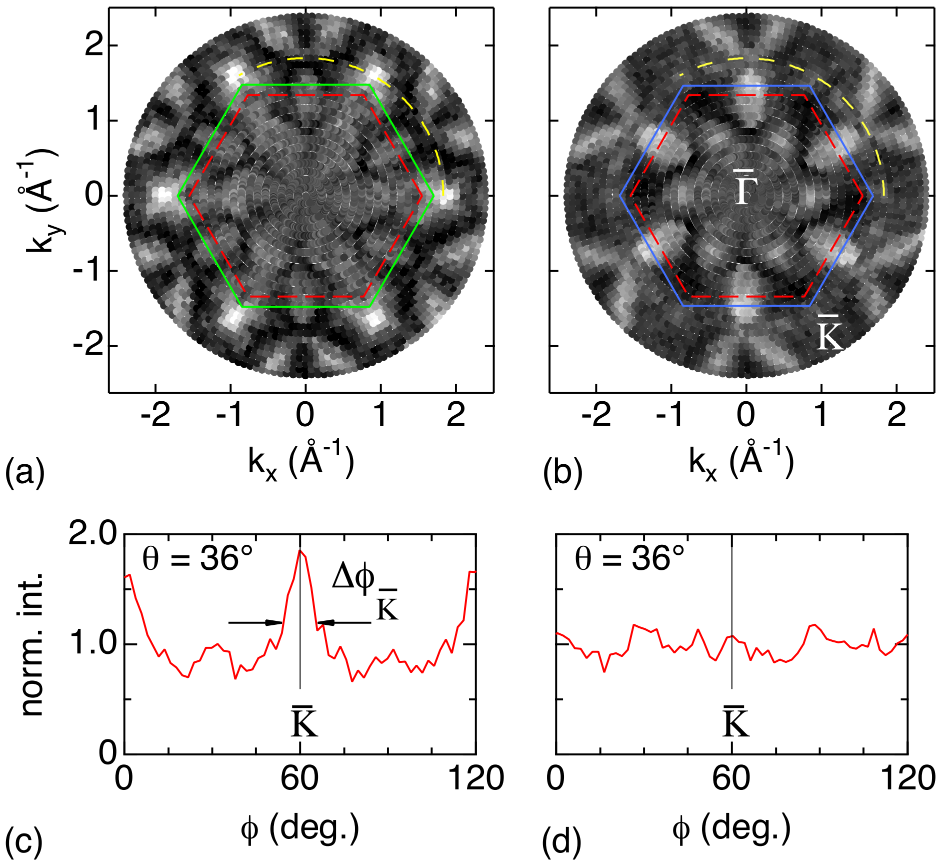

Figure 3.5: He II$_\alpha$ FSMs. (a) *g*/Ru(0001). (b) *h*-BN/Ru(0001). The hexagons indicate the surface BZs of Ru(0001) (red dashed), graphite [green solid in (a)] and *h*-BN [blue solid in (b)]. (c) and (d) show the normalized intensities of azimuthal cuts along the dashed yellow sectors in (a) and (b) respectively.

we find $\Delta\phi_{\bar{K}} = 0.27 \pm 0.03$ rad, which translates to $N_e = 0.09 \pm 0.02$ electrons per 1×1 graphene unit cell. Of course, this value is the weighted average for mounds and valleys.

The differences in the atomic and electronic structure are also reflected in the potential energy surfaces that drive the functionality of the super structures as templates for the formation of molecular arrays. In Figure 3.6(a) the calculated electrostatic potential for *g*/Ru(0001) at the position of adsorbed xenon atom cores (3.8 Å above the carbon cores) is shown. As for the case of *h*-BN/Rh(111) nanomesh the electrostatic energy landscape correlates with the atomic corrugation [27]. For the theoretical corrugation of *g*/Ru(0001) of 1.5 Å we obtain a potential amplitude of 0.52 eV. This potential amplitude may be measured with PAX [53]. Also for *g*/Ru(0001) two Xe bonding regions can be distinguished with distinct Xe 5p$_{1/2}$ photoemission binding energies [Figure 3.6(b)]. Assuming a Xe van der Waals radius of 2.2 Å, 50 Xe atoms per *g*/Ru(0001) unit cell are expected for the monolayer coverage [62]. From the spectral weight and the known atomic structure it can be deduced that the Xe^V species in the graphene valley has the higher Xe 5p$_{1/2}$ photoemission binding energy and contains 37 atoms at full coverage. The Xe^M species with lower photoemission binding energy corresponds to Xe adsorbed on the mounds of the graphene. The binding energy difference between these two species of 236 ± 5 meV is deter-

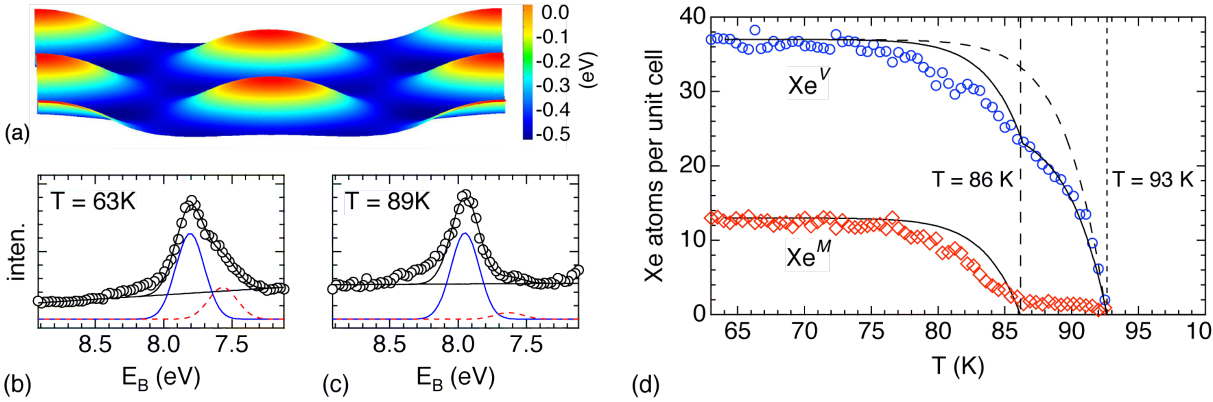

Figure 3.6: Xe adsorption on *g*/Ru(0001). (a) Calculated electrostatic potential map 3.8 Å above the outermost carbon atoms. [(b) and (c)] He I$_\alpha$ excited Xe 5p$_{1/2}$ spectra for two Xe coverages during thermal desorption. At high coverage two spectral components may be distinguished, as can be seen from the two Gaussians that are fitted to the data. (d) Spectral weights of the two Xe species as a function of temperature. Blue open circles stand for the high binding energy and red open diamonds for the low binding energy component.

mined from a fit of two Gaussians with equal width and does not depend on the coverage. This value reflects a local work function difference between V- and M-graphene and is in line with the theoretical result shown in Figure 3.6(a). Since for *h*-BN/Ru(0001) no experimental PAX data is available we compare the *g*/Ru(0001) PAX results with the similar system *h*-BN/Rh(111) nanomesh [27]. For both the strongly bound regions (valley and holes) have a lower work function. However, for *g*/Ru(0001) the local work function difference is about 20 % lower than for the case of *h*-BN/Rh(111). Intuitively, this is related to the metallic nature of the graphene that screens out lateral electric fields in the sp^2-layer. The better screening of graphene is indeed reflected in the Xe 5p$_{1/2}$ final state binding energy as referred to the vacuum level $E_B^V = E_B + \Phi$ [73]. Table 3.1 shows that E_B^V of Xe^V at monolayer coverage ($\theta \to 1$) on *g*/Ru(0001) is 210 meV smaller than that of Xe^H on *h*-BN/Rh(111).

From the thermal desorption the Xe adsorption energy is inferred. In Figure 3.6(d) the spectral weights of the Xe species are shown as a function of temperature (heating rate $\beta = 1.5 \pm 0.05\,\mathrm{K\,min^{-1}}$). The temperatures at which the two Xe species disappear indicate that Xe^V is about 8 % stronger bound than Xe^M. In order to compare *g*/Ru with *h*-BN/Rh, the temperature dependent weights of the two Xe species were fitted to zero order desorption. From $-dN = \nu/\beta \exp(-E_d/k_\mathrm{B}T)dT$ the desorption energies E_d are found (see Table 3.1). The values are slightly smaller than the desorption energies on graphite (249 meV [74]) but higher with respect to *h*-BN/Rh. The fits for zero order desorption show that the Xe^V species are not well described with a single desorption energy [dashed line in Figure 3.6(d)]. In the *h*-BN/Rh case two Xe^H phases (C^H and R^H) had been identified by a pronounced kink in the desorption spectrum of Xe^H. The more strongly bound of these two phases was assigned to Xe^H atoms at the rims of the holes where dipole rings induce an enhanced polarization and bonding. For *g*/Ru(0001) a clear

	g/Ru(0001)		*h*-BN/Rh(111)		
Phase	Xe^M	Xe^V	C^W	C^H	R^H
E_d (meV)	222	231	181	184	208
N_1	13	37	25	17	12
$E_B(\theta \to 0)$ (eV)		7.97		7.87	
$E_B(\theta \to 1)$ (eV)	7.56	7.80	7.42	7.72	
$\Phi(\theta \to 0)$ (eV)	3.90		4.18		
$\Phi(\theta \to 1)$ (eV)	3.89		4.18		

Table 3.1: Experimentally determined Xe parameters for *g*/Ru(0001) and *h*-BN/Rh(111) (Ref. [27]): desorption energies E_d, number of Xe atoms at full coverage N_1. For all fits an attempt frequency ν of 1.2×10^{12} Hz has been used. Xe $5p_{1/2}$ photoemission binding energies E_B and global work functions Φ for the two coverage limits ($\theta \to 0$ = zero coverage, $\theta \to 1$ = monolayer coverage). The errors for the binding energies E_B and the work functions Φ are ± 0.02 eV and ± 2 meV for the desorption energies E_d.

kink is not visible, but the deviations from the fit also indicate variations in bonding strength of the Xe^V atoms. It could well be the case that the stronger Xe bonding sites are localized at the rims of the *g*/Ru valley. The difference to *h*-BN/Rh may be understood by the inverse shape of the potential energy surface. If we fit like for *h*-BN/Rh(111) the C^H and the R^H phase [27] two Xe^V phases for *g*/Ru(0001) [solid line in Figure 3.6(d)], binding energies of 222 meV and 234 meV are obtained for *g*/Ru(0001). The smaller difference of 12 meV is not unreasonable if the lower local work function modulation of *g*/Ru is considered, which induces a lower polarization of Xe on the rims.

3.1.3 Conclusions

In conclusion both *g*/Ru and *h*-BN/Ru have covalently and loosely bound regions, but with inverted topography. The presented findings suggest that *g*/Ru is not a corrugated single layer dielectric like *h*-BN/Ru, but a corrugated single layer metal with a Fermi surface. In contrast to *h*-BN/Ru, *g*/Ru shows no σ-band splitting due to a different polarization of the unequal regions in the supercell, though also on *g*/Ru lateral electric fields are found to act on adsorbates. The electrostatic potential variations within the supercell make both templates for molecular trapping, where the metallicity of graphene imposes a stronger electronic coupling of adsorbates to the underlying substrate.

The following chapter is a modified version of the submitted manuscript of:
T. Brugger, H. Ma, M. Iannuzzi, S. Berner, A. Winkler, J. Hutter, J. Osterwalder, and T. Greber, *Reversible switching of surface texture by hydrogen intercalation* (2009), submitted.

3.2 Reversible switching of surface texture by hydrogen intercalation

Intercalation – that is the reversible embedding of atomic or molecular species into a layered material – is a key concept for materials functionalization. Graphite is the prototype intercalation material [75] in which the relatively weak bonding between sp^2-hybridized carbon sheets allows the packing of molecular species between subsequent layers. On transition metals, single sheets of carbon (graphene) and boron nitride (*h*-BN) form highly ordered nanostructures [19, 20, 22, 59]. The lateral periodicity of these superstructures is determined by the lattice mismatch between the sp^2 layers and the substrate. For 4d and 5d transition metals the superlattice constant is about 10 times that of the free standing sp^2 layer [19, 20, 22, 59]. The deformation of the surfaces in the vertical direction – the *corrugation* – can reach values of 0.1 nm and is controlled by the bonding of B, C and N to the transition metals, where the lattice mismatch *and* the site dependent bonding impose a dislocation network with mainly out-of-plane strain in the sp^2 layer. The corrugation is the essential property that determines the texture and functionality of these superstructures and imposes a variety of new phenomena. These are for example the formation of dipole rings which are in-plane lateral electric fields [27, 38] that constitute traps for single molecules or clusters at room temperature [26, 76]. Here it is shown that the surface texture of *h*-BN/Rh(111) may be reversibly switched from corrugated to flat by hydrogen intercalation and back to corrugated by hydrogen removal.

3.2.1 Experimental

STM has been performed at $T = 350\,\mathrm{K}$ in an Omicron VT-STM where atomic hydrogen had been created through dissociation of molecular hydrogen at a hot W filament and dosed on the sample through a nozzle. In the photoemission experiment a highly effective doser had been used, in which a hot W capillary tube directs a well collimated beam of atomic hydrogen or deuterium on the sample surface [77]. Thermal desorption spectra were taken with a Prisma QMS 200 M2 quadrupole mass spectrometer (Pfeiffer Vacuum) in the channeltron mode. The pumping speed of the used TMU 071 P turbomolecular pump (Pfeiffer Vacuum) was $42\,\mathrm{ls}^{-1}$ for mass 2 (H_2) and $50\,\mathrm{ls}^{-1}$ for mass 4 (D_2) from which we interpolated $46\,\mathrm{ls}^{-1}$ for mass 3 (HD).

3.2.2 Theory

The structural and electronic properties of the *h*-BN/Rh(111) have been investigated through an atomistic model using DFT. As an initial configuration for the structure optimizations a four

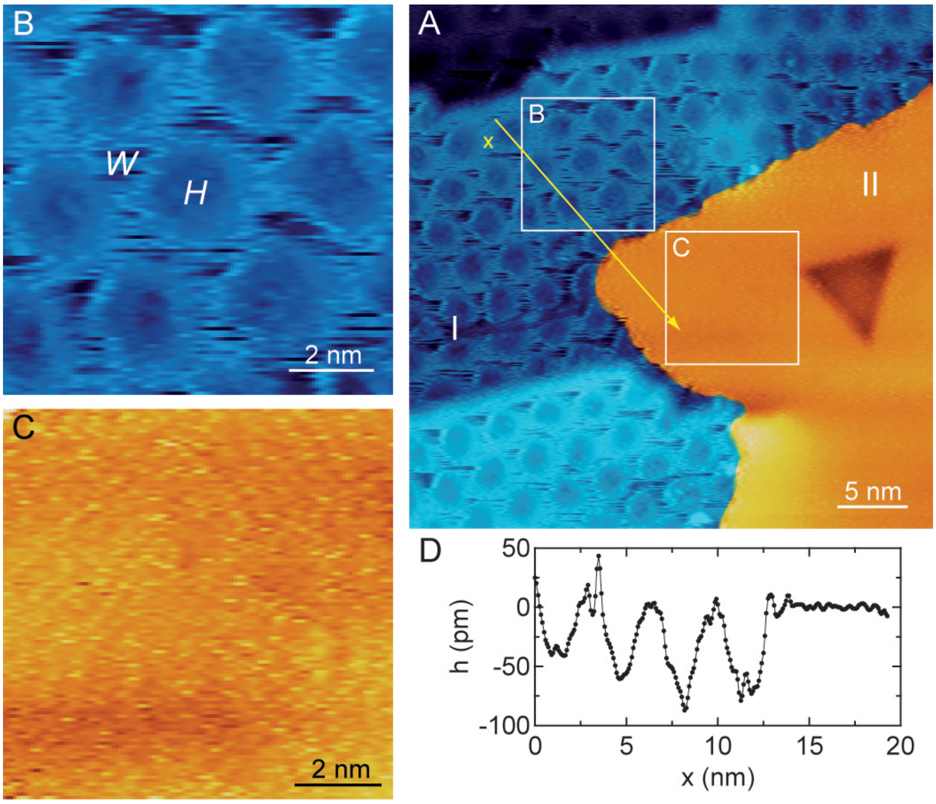

Figure 3.7: Topographic STM data of the *h*-BN/Rh(111) after exposure to atomic hydrogen. A Large scale image showing the coexistence of pristine corrugated and hydrogen intercalated flat *h*-BN/Rh(111) (regions I and II respectively). B Zoom into the pristine *h*-BN/Rh(111) area showing the wire (W) and the hole (H) regions. C Zoom into the flat *h*-BN/Rh(111) area. D Line profile along the yellow line in a) showing the transition from corrugated (I) to flat (II) *h*-BN/Rh(111).

layer Rh slab with 12×12 replicas of the two dimensional Rh(111) unit cell using the bulk Rh lattice constant of $a_{Rh} = 3.801\,\text{Å}$ plus one layer of hexagonal boron nitride containing 13×13 replicas of the *h*-BN unit cell stretched to match the 12×12 Rh(111) units have been used. An effective vacuum region of 25 Å has been added to prevent any spurious interaction among periodic images. All except the in-plane coordinates of the lowest Rh layer atoms have been relaxed. The electronic structure has been computed in the framework of the hybrid Gaussian and plane wave scheme (GPW) [78, 79] as implemented in the Cp2k package [80] using the supercell obtained from the structure optimization. The revised Perdew-Burke-Ernzerhof (revPBE) exchange-correlation functional in the generalized gradient approximation (GGA) [81] adding the dispersion correction due to Grimme [82], Molopt local basis sets [83] and GTH pseudopotentials [84] have been used. VMD has been used for rendering high resolution representations from the structure optimization results [85].

3.2.3 Results

The corrugation of the *h*-BN/Rh(111) nanomesh superstructure can directly be observed using STM . It has a peculiar electronic structure which is reflected in the core level binding energies of the elements that are sensitive to the position of the atoms [86]. A splitting of the N 1s core level into two components as observed with XPS is ascribed to the *h*-BN layer corrugation [86] and a separate set of sp^2-derived bands shows up in UPS [20].

The topographic STM data presented in Figure 3.7 show that after exposure to atomic hydrogen (H) a new phase of single layer *h*-BN without long-range periodic corrugation (II) can coexist with the unaltered nanomesh (I). Phase II is basically flat whereas the pristine nanomesh (I) exhibits a corrugated hexagonal surface texture with a periodicity of 3.2 nm. A third phase which has been observed in further STM images (not shown) consists of a crumpled *h*-BN layer in which the original nanomesh is still visible at a few places. This phase is the intermediate level where insufficient H intercalation led to a nanomesh corrugation which is not yet fully switched off. The dark triangle in region II of Figure 3.7 A is a dislocation within the Rh(111) substrate as it is often found and was used as a landmark for orientation. The zoom-in images in Figure 3.7 display a section of the same area taken from regions with and without corrugation. In the textured zoom-in six nanomesh unit cells are seen, where the two topographic elements, the ‘holes’ (*H*) and the ‘wires’ (*W*) become visible (Fig. 3.7 B). The zoom into the untextured region is basically flat (Fig. 3.7 C). The height profile in Figure 3.7 D shows the transition from the intact, corrugated nanomesh region into the flat region. The surface in the flat region levels on the height of the wires, that is the loosely bound regions in the nanomesh.

In order to determine the amount of H that is incorporated into *h*-BN/Rh(111) in the switched off (flat) state we performed thermal desorption spectroscopy (TDS) measurements during a switch on (roughening) process of the *h*-BN/Rh(111) nano-texture by annealing. We found no isotope effect between hydrogen and deuterium (D), though it is advantageous to use D since the deuterium background signal in TDS is much smaller than that of hydrogen. Also the use of isotopes allows to show that the effect is caused by atomic H (D), and at the investigated conditions not by the molecular forms H_2 (D_2). Figure 3.8 shows the TDS curve of molecular deuterium (D_2, atomic mass 4, heating rate $\beta = 0.2\,\mathrm{K\,s^{-1}}$) from a sample that had been exposed to D to switch off the surface texture and subsequently flushed with H_2 in order to supplant D on the sample holder with an isotope exchange reaction. Simultaneously the TDS signal of HD (atomic mass 3) has been recorded. From the area under both curves (3 amu and 4 amu) and the pumping speed the amount n_D of desorbed D can be inferred. We find $n_\mathrm{D} \approx (4 \pm 0.5) \cdot 10^{14}\,\mathrm{cm^{-2}}$ D atoms to be incorporated in the untextured state. This value of n_D corresponds to about 0.25 ML (1 ML $\equiv$ one atom per Rh top layer atom) but has to be regarded as a lower limit for the incorporated D amount. Remarkably, n_D is close to the number of protons which was found to bind to *h*-BN/Rh(111) in cyclic voltammograms in an electrolyte [36].

The surface texture switching is also monitored by its spectroscopic signatures that is the N 1s and B 1s XPS spectra and the band splittings of the sp^2-derived bands (Fig. 3.9). The evolution

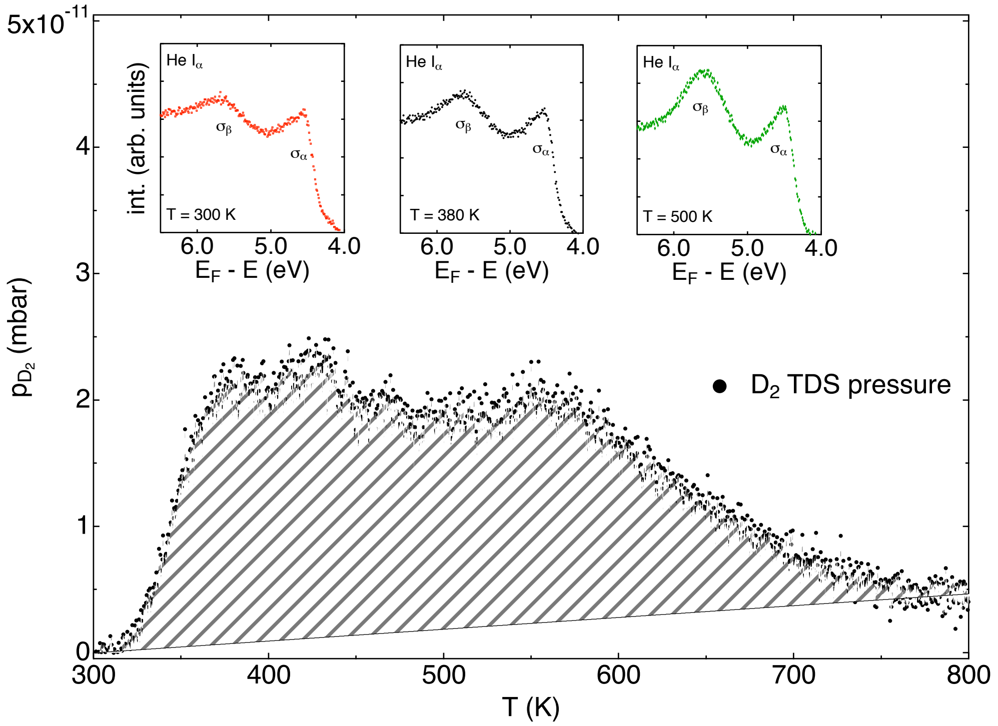

Figure 3.8: Deuterium TDS data from *h*-BN/Rh(111) intercalated with D (filled black circles, $\beta = 0.2\,\mathrm{K\,s^{-1}}$). The hatched area is proportional to the amount of D intercalated between the *h*-BN and the topmost Rh layer. The insets display He I_α normal emission UPS data for the region of the *h*-BN/Rh(111) σ bands measured during a temperature ramp.

of the N 1s core level peak during a switch off – switch on cycle substantiates the picture (Fig. 3.9 A). In the as prepared state the N 1s peak of the nanomesh can be fitted by two Gaussians with a splitting of 680 meV between the low and the high binding energy component corresponding to the wire (N_W 1s) and the hole (N_H 1s) regions, respectively [86]. The fit results in a ratio of about 3 : 1 for the peak heights of N_W 1s and N_H 1s. After switching off the surface texture of the nanomesh the peak considerably narrowed at the binding energy of the wire regions. Upon annealing the sample the N 1s peak broadens back to the original ratio of N_W 1s : N_H 1s $\approx$ 3 : 1. The same effect is observed for the B 1s core levels (not shown), though the splitting is smaller. This is an indication that the hydrogen does not bind to the *h*-BN, and it is thus conjectured that the hydrogen intercalates, i.e. binds to the Rh substrate. The insets in Figure 3.9 A show low-energy electron diffraction (LEED) data of the nanomesh in the switched on and the switched off state: The super cell size does not depend on the corrugation. The sharpness of the superstructure diffraction spots in the switched off state which originate from the (13 × 13) *h*-BN on (12 × 12) Rh units prove the structural integrity of the *h*-BN layer and exclude a twist with respect to the Rh(111) substrate in the flat state. In Figure 3.9 B the He I_α normal emission photoemission spectra also indicate a flattening of the *h*-BN layer: The bands related to the holes of the nanomesh (σ_β and π_β) vanish after H exposure. Furthermore, annealing of the H exposed sample [H/*h*-BN/Rh(111)] to about 600 K recovers the original band splitting as a result of a

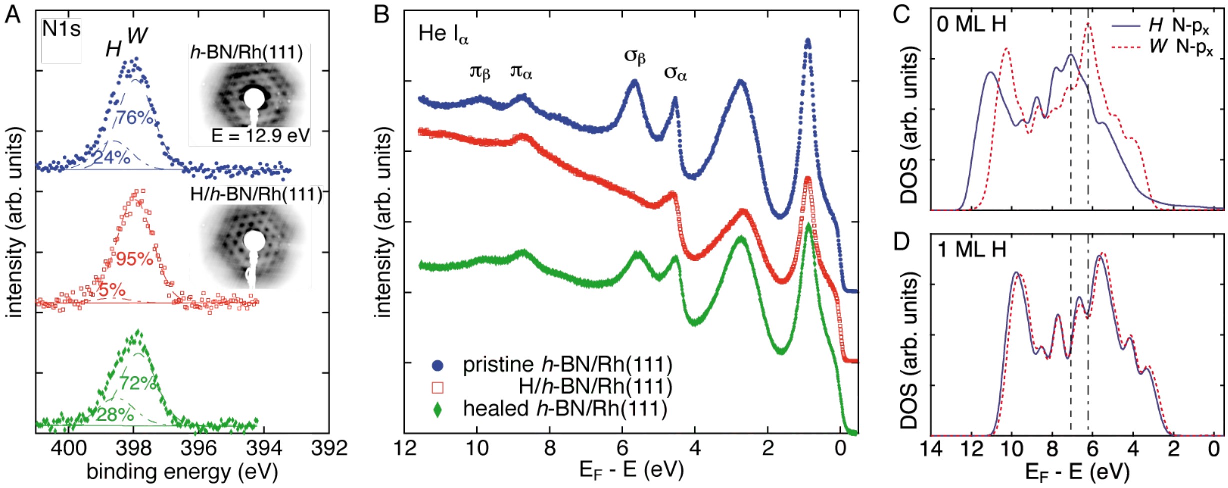

Figure 3.9: A and B The *h*-BN/Rh(111) nanomesh before (filled blue circles) and after (open red rectangles) hydrogenation; and after H desorption (filled green diamonds). A N 1s core level XPS (monochromatized Al K_α radiation) which features a distinct narrowing upon hydrogenation. Insets in A show the LEED diffraction patterns of the corrugated superstructure of *h*-BN/Rh(111) (upper panel) and the superstructure of H/*h*-BN/Rh(111) (lower panel) for a primary electron energy of $E = 12.9\,\text{eV}$. B He I_α normal emission UPS shows a vanishing of the σ_β and π_β peaks which are attributed to the holes (H) of the *h*-BN/Rh(111) after exposure to H while the σ_α and π_α peaks corresponding to the wires (W) of the *h*-BN/Rh(111) remain.
C and D Calculated projected DOS of p_x orbitals originating from N atoms in hole (H) and wire (W) regions of pristine *h*-BN/Rh(111) and *h*-BN/Rh(111) intercalated with 1 ML of H, respectively.

switch-back to the pristine nanomesh.

In Figure 3.9 C and D calculated densities of states (DOS) of p_x states on the nitrogen atoms that constitute the *h*-BN σ bands are displayed. The results for the clean nanomesh in Figure 3.9 C are in line with the experiment and Refs. [26, 28]. The N p_x DOS in the hole and wire sites have pronounced peaks at about 7 eV and 6 eV below E_F, respectively, which reproduce the experimentally observed σ band splitting of about 1 eV well. The calculated densities in Figure 3.9 D comprise 1 monolayer of intercalated hydrogen and feature the experimentally observed disappearance of the hole derived σ_β band in *h*-BN/Rh(111) under the exposure to H (or D). The structure of the full *h*-BN/Rh(111) system (567 Rh atoms plus 169 BN pairs in the unit cell) was optimized by DFT. The results agree with previously reported findings [28]. The optimized structure is displayed in Figure 3.10 A and shows a corrugated *h*-BN layer where about 40 % of the BN units are in close and about 60 % are in loose contact to the Rh(111) substrate forming the holes and the wires, respectively [about 2.2 Å and 3.2 Å above the topmost Rh(111) layer]. Hydrogen intercalation below *h*-BN on Rh(111) has been investigated in several steps starting with a single H atom on top of a free standing *h*-BN layer where no binding was found for distances greater than 2 Å. On the pristine Rh(111) surface H bonding is observed up to at least

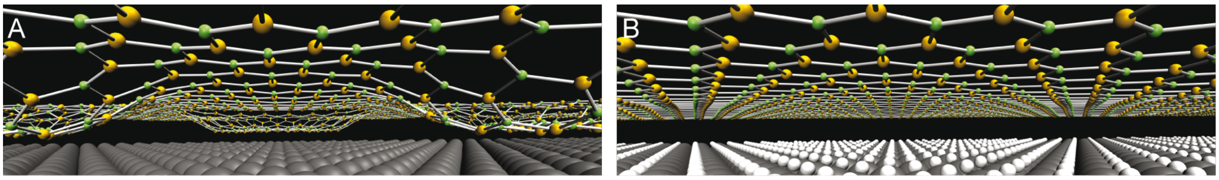

Figure 3.10: Three dimensional representation of the results from the structure optimizations with DFT. A The clean *h*-BN/Rh(111). B The *h*-BN/Rh(111) with one H atom per Rh unit intercalated between the *h*-BN and the topmost Rh(111) layer. In the pictures the corrugation amplitude of the *h*-BN layer has been enhanced by a factor of two. Rh atoms are displayed in grey, B and N atoms in orange and green, respectively, and H atoms in white. Atom sizes are not to scale.

one monolayer where H atoms favor *fcc* hollow sites in accordance with [87]. Also, distributing atomic H between the *h*-BN and the top Rh layer and optimizing the structure leads to a H–Rh bonding for the case of the full monolayer, H atoms again occupy *fcc* hollow sites. In the final step the full system of 13×13 BN units and a four layer 12×12 Rh(111) slab in the presence of intercalated H has been optimized. Figure 3.10 B shows the resulting structure for 12×12 intercalated H atoms per supercell unit (1 ML) which again favor *fcc* hollow sites and level at a height of 1.0 Å above the topmost Rh layer. A fundamental observation for the H intercalated system is the drastic reduction of the *h*-BN corrugation amplitude by a factor of five from 1.1 Å to 0.2 Å which supports the picture of H intercalation drawn from the experiment. A gradual repulsion of the *h*-BN layer was found for increasing amounts of H, where the mean *h*-BN layer – Rh distance increases from about 2.9 Å for the pristine *h*-BN/Rh(111) to about 3.4 Å for the *h*-BN/Rh(111) intercalated with 1 ML of H. This structural change directly influences the electrostatic potential whose corrugation amplitude within the nanomesh unit cell drops from 480 meV to 180 meV at a distance of 3.9 Å above the *h*-BN layer. Thus the strength of the lateral dipole rings in the *h*-BN layer, which are located at the sites of the highest corrugation gradient and which are the source of the molecular traps of the *h*-BN/Rh(111) nanomesh, is expected to be reduced by about 90 % (the dipole ring strength is proportional to the square of the potential gradient). The experimentally observed disappearance of the σ_β band in UPS after H intercalation is also confirmed by theory where the σ band splitting between the hole and wire derived N p_x DOS decreases with the amount of intercalated H, finally rendering both DOS experimentally indistinguishable for coverages $\gtrsim$ 0.5 ML (Fig. 3.9 D).

3.2.4 Conclusions

In conclusion we have shown that exposure of the a single layer of hexagonal boron nitride on Rh(111) to atomic hydrogen leads to a change of the surface texture where the corrugation of the sp^2 layer vanishes. This flattening is accompanied by a strong change of the electronic structure of *h*-BN/Rh(111). In the flat state at least one H atom is captured between four *h*-BN and Rh(111) units. We suppose that the ability of the nanomesh to trap molecules and thus its template functionality is drastically reduced in this flat state. Mild annealing recovers the original surface texture of the *h*-BN/Rh(111) nanomesh. Regarding similar sp^2-hybridized template systems the metallic analog of the nanomesh – graphene on Ru(0001) – is an interesting candidate for further investigations and is expected to show comparable switching behavior.

3.3 *h*-BN on Co

Ferromagnetic materials have been arousing interest ever since the discovery of lodestone (Fe_3O_4, magnetite) by the ancient Greeks about two thousand years ago. A profound understanding of the fundamentals of magnetism and its inextricable link to electricity has been developed over the last two centuries [88]. Since the emergence of nano-technology a new field investigating finite size effects in magnetic materials has been growing vastly. In the last years for example ferromagnetic cobalt alloys with extremely small domain sizes and out of plane magnetization were started to be used in commercial hard disk drives. Another large area of research are spintronics where thin films of ferromagnetic materials may be used as efficient spin sources as well as spin valves if they are arranged in a multi-layer system with a nonmagnetic spacer layer sandwiched between them [89]. But ferromagnetic materials may also be used as a scattering target in electron spin detection devices which exploit the strong spin-exchange interaction among electrons of very low kinetic energy (VLEED) [90]. The experimental problem in VLEED regarding the ferromagnetic target is its stability against contaminations. Due to the low kinetic energy of the scattering electrons the spin dependent scattering is very surface sensitive and the target has to be atomically clean in order to achieve high spin detection yields. The only possibility to overcome this problem is to find a passivation mechanism which renders the surface inert while preserving its ferromagnetic property. A few years ago it was found that the ferromagnetic Fe(001) surface may be passivated by oxidation upon which a $p(1 \times 1)$-O reconstruction is formed. The Fe(001)-$p(1 \times 1)$-O is stable in UHV up to a few weeks and its spin asymmetry is even higher compared to that of the bare Fe(001) surface [91]. Recently a new spin-polarized photoemission spectrometer with a high spin detection figure of merit which utilizes this target for electron scattering has been developed [92].

Besides oxidation there are other ways to treat ferromagnetic surfaces in order to achieve a passivation. Hexagonal boron nitride (*h*-BN, $a_{h-\mathrm{BN}} = 2.504\,\text{Å}$ [7]) for example has been shown to form 1×1 commensurate monolayers when grown on the (111) face of nickel [57, 93]. Ni has a *fcc* crystal structure ($a_{\mathrm{Ni}} = 3.524\,\text{Å}$ [94]) and is one of the three 3d transition metals Fe, Co and Ni which show itinerant ferromagnetism. Among those it has the smallest magnetic moment of $0.6\mu_{\mathrm{B}}$ due to the highest minority d band occupancy [95]. When *h*-BN is grown on the Ni(111) surface a perfect monolayer with a very low density of defects evolves due to the small compressive lattice mismatch of about 0.5 %. This protecting layer remarkably increases the inertness of the Ni surface [34]. However the magnetic moment in the *h*-BN/Ni(111) interface is found to be decreased in comparison to bare Ni(111) [32]. The decrease was assigned to a charge transfer from *h*-BN to the partially empty minority d band of Ni (about $0.06\,\mathrm{e}^-$ per surface unit cell) which results in a shift of the Ni 3d bands towards lower binding energy and a decrease of the minority d hole pocket of the Fermi surface.

Out of the triplet Fe, Co and Ni there is one more element for which surfaces with hexagonal symmetry exist and which therefore could be suitable for the growth of perfect *h*-BN layers (*h*-BN may also be grown on crystal faces with rectangular symmetry but there different structural domains can coexist on the same sample [96, 97]). Co has a *hcp* crystal structure at room temperature ($a_{\mathrm{Co}} = 2.507\,\mathrm{\AA}$, $c_{\mathrm{Co}} = 4.067\,\mathrm{\AA}$ [98]) and a magnetic moment of $1.7\,\mu_{\mathrm{B}}$ [99] which is nearly three times as large as the one of Ni. The matching of the lattice constant to *h*-BN is almost perfect with a slight tensile lattice mismatch of 0.1 %. DFT calculations show that the binding energy between *h*-BN and the transition metal surfaces decreases with the filling of the d shell and accordingly give a binding energy for *h*-BN/Co(0001) which is larger than for *h*-BN/Ni(111) [33]. In addition the *h*-BN ionicity is predicted to be smaller on Co while the charge transfer from the *h*-BN layer to the metal surface top layer is higher. It is worth mentioning that this ‘charge transfer’ is more to be regarded as a static polarization at the *h*-BN – metal interface instead of a real transfer of charge [34] (Sec. 1.3).

So far the existence of *h*-BN/Co has only been reported once where experimental N 1s and B 1s core level spectra measured by XPS have been shown [100]. Here we investigate the electronic structure of *h*-BN/Co measured with angle-resolved ultraviolet photoelectron spectroscopy. Band-structure measurements along the high symmetry directions $\overline{\Gamma\mathrm{K}}$ and $\overline{\Gamma\mathrm{M}}$ as well as FSMs will be presented. Information about the atomic structure of the interface is obtained by means of LEED and STM.

3.3.1 Experimental

100 nm thick Co(0001) films grown on a sapphire (Al_2O_3) substrate ($10 \times 10 \times 0.5\,\mathrm{mm}^3$) including an approximately 50 nm thick yttria-stabilized zirconia (YSZ) buffer layer served as metal substrates. These were cleaned by repeated Ar^+ sputter and annealing cycles, including O_2 exposure at 1000 K. The *h*-BN layer was formed by exposure of the clean substrate to 70 L of borazine [$(HBNH)_3$] at 1050 K. Because Co undergoes a structural phase transition from *hcp* to *fcc* at about $T = 660\,\mathrm{K}$ [101] the growth of the *h*-BN layer takes place in the *fcc* phase. The lattice constant for the Co *fcc* phase is reported to be $a_{\mathrm{Co,fcc}} = 3.5688 - 3.6214\,\mathrm{\AA}$ in a temperature range of 793 – 1671 K [102]. A linear extrapolation of this lattice constants to 1050 K together with the temperature dependent lattice constant

$$\begin{aligned} a_{h-\mathrm{BN}} &= 2.50424\,\mathrm{\AA} - 7.42\cdot 10^{-6}\,\mathrm{\AA K}^{-1}\left[T(\mathrm{K}) - 273.15\,\mathrm{K}\right] \\ &\quad + 4.79\cdot 10^{-9}\,\mathrm{\AA K}^{-2}\left[T(\mathrm{K}) - 273.15\,\mathrm{K}\right]^2 \end{aligned}$$

of *h*-BN [7] yields a tensile lattice mismatch of about 1.3 % at the growth temperature. This mismatch is definitely larger than the one derived from the room temperature lattice constants.

3.3.2 Results

For *hcp* Co the He I_α photoemission free final state sphere of electrons which originate from the vicinity of the Fermi level E_{F} ($E_{\mathrm{B}} \approx 0\,\mathrm{eV}$) has a radius of $k_z \approx 2.8\,\mathrm{\AA}^{-1}$ (Eqn. 2.3, inner potential $V_0 = 13.0\,\mathrm{eV}$, work function $\phi \approx 5\,\mathrm{eV}$). As a consequence mainly states in the lower half of the third BZ (about half way between the A point and the Γ point for normal emission) are sampled for initial states close to E_{F}.

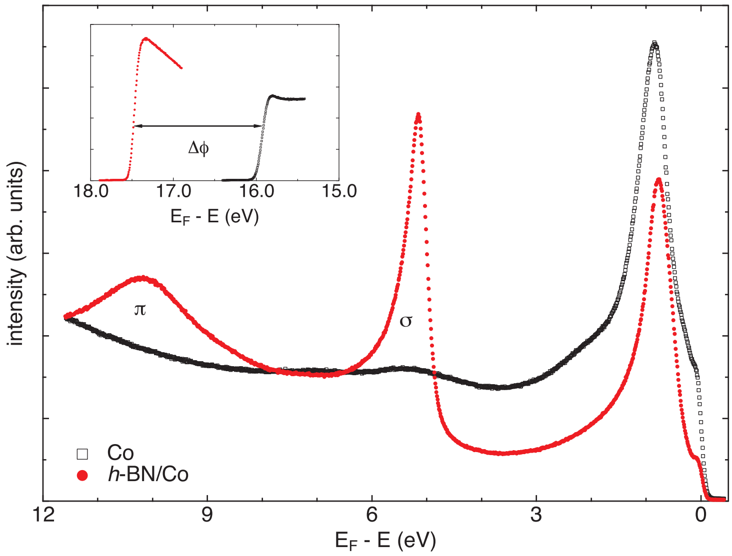

Figure 3.11: He I_α excited normal emission spectrum of *h*-BN/Co(0001) (filled red circles) and clean Co(0001) (open black rectangles). In addition to the Co bands one very sharp σ band and one π band is observed. The inset shows the secondary electron cutoff region where a shift of the work function ϕ can be observed.

Consistent with previous reports [103, 104] the normal emission UPS from clean Co in Figure 3.11 is governed by a broad peak centered at a binding energy of 0.8 eV and spanning a region of about 2 eV which originates from the Co 3d bands (Λ_3-symmetry). After formation of the *h*-BN layer the sample work function is found to be decreased by $\Delta\phi = 1.5\,\text{eV}$ from 5.3 eV for clean Co to 3.8 eV for the *h*-BN covered surface. This proves the predicted static polarization between the *h*-BN layer and the Co top layer [33, 34]. The Co 3d peak is found to be attenuated and slightly shifted in binding energy. However the shift of $\Delta E_B \approx -0.1\,\text{eV}$ towards lower binding energy is counterintuitive: For *h*-BN/Ni(111) a shift of the d band towards higher binding energy had been observed consistent with a ‘charge transfer’ from the *h*-BN layer into the largely unoccupied minority d bands [32]. A photoemission final state effect is unlikely to be the origin of the unexpected d band shift: The work function change of $-1.5\,\text{eV}$ during formation of the *h*-BN layer leads to an increase of k_z which corresponds to about 9 % of the distance $\overline{\mathrm{A}\Gamma}$ and along this high symmetry direction no strongly dispersing bands are found in the corresponding binding energy region [105]. In addition to the change of the Co related band two new *h*-BN derived peaks appear: A very sharp σ and a broad π band located at 5.1 eV and 10.2 eV binding energy, respectively. Calculating the binding energy of the σ band with respect to the vacuum level E_V a value of $E_B^V = E_B^F + \phi = 8.9\,\text{eV}$ is found. This value exactly agrees with the vacuum-level alignment as it has been shown by Nagashima *et al.* for *h*-BN on Ni(111), Pd(111) and Pt(111) [34]. The work function shift is obviously caused by the π electrons which have an asymmetric probability density with its main weight on the interface side rather than on the vacuum side of the *h*-BN basal plane.

Figure 3.12 shows that the *h*-BN layer forms as a 1×1 structure on the Co top layer. The LEED

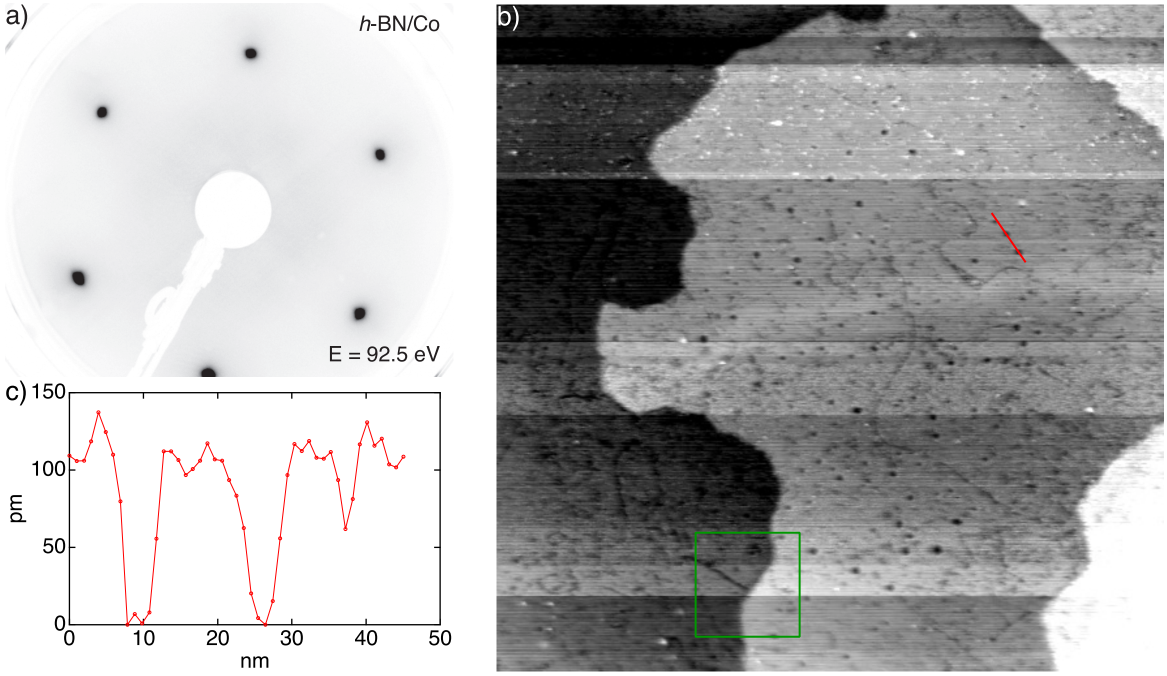

Figure 3.12: Atomic structure of *h*-BN/Co. a) LEED picture of *h*-BN/Co taken at an electron energy of $E = 92.5\,\mathrm{eV}$. The *h*-BN layer grows in a 1×1 structure on Co. b) and c) Room temperature STM data of *h*-BN/Co. b) STM topography image: $200\,\mathrm{nm} \times 200\,\mathrm{nm}$, $V_s = +0.8\,\mathrm{V}$, $I_t = 0.3\,\mathrm{nA}$. c) Line profile along the marked line in b). The defect marked by the square green ROI in b) is described in the text.

image in Figure 3.12 a) does not display any diffraction spots other than the sharp Co principal ones after *h*-BN exposure which indicates the growth of a commensurate 1×1 *h*-BN layer. The STM image of Figure 3.12 b) and its corresponding line profile [Fig. 3.12 c)] show a basically flat surface which is pervaded by a lot of grooves and pits (density about $1.6 \cdot 10^{-2}\,\mathrm{nm}^{-2}$). The grooves are $5 - 10\,\mathrm{nm}$ wide and up to about $150\,\mathrm{nm}$ long. They can be buried under successive Co layers in which they then are not visible any more by STM [see green ROI in Fig. 3.12 b)]. The pits have diameters of about $5\,\mathrm{nm}$ and depths of up to about $1\,\mathrm{\AA}$ as seen by STM. No regularity could be detected in the position of the defects. Measurements on the clean Co substrate (not shown) display a similar amount of analog defects and thus allow the conclusion that they originate from the Co metal substrate and that the *h*-BN forms a closed homogeneous layer on the defect free substrate areas.

The band dispersion of the σ bands (σ_1 and σ_2 are degenerate at $\overline{\Gamma}$) and the π band along $\overline{\Gamma\mathrm{K}}$ and $\overline{\Gamma\mathrm{M}}$ are displayed in Figure 3.13 a) and b), respectively. A large band gap of more than $4\,\mathrm{eV}$ is observed. The π band at $\overline{\mathrm{K}}$ levels off at a binding energy of $4.4\,\mathrm{eV}$ and at $\overline{\mathrm{M}}$ a value of $5.4\,\mathrm{eV}$ is found. Thus the π band width of $5.9\,\mathrm{eV}$ along $\overline{\Gamma\mathrm{K}}$ is $0.4\,\mathrm{eV}$ larger than for *h*-BN/Ni(111) ($5.5\,\mathrm{eV}$) [106] which is in line with the smaller ionicity of *h*-BN on Co [33]. The large number of unoccupied d states in Co leads to strong many-body interactions in the photoemission process and explains why no sharp quasiparticle peaks are found in the measured band structures of the clean Co surface along $\overline{\Gamma\mathrm{K}}$ and $\overline{\Gamma\mathrm{M}}$ for binding energies greater than $2\,\mathrm{eV}$ [Figs. 3.13 c) and d),

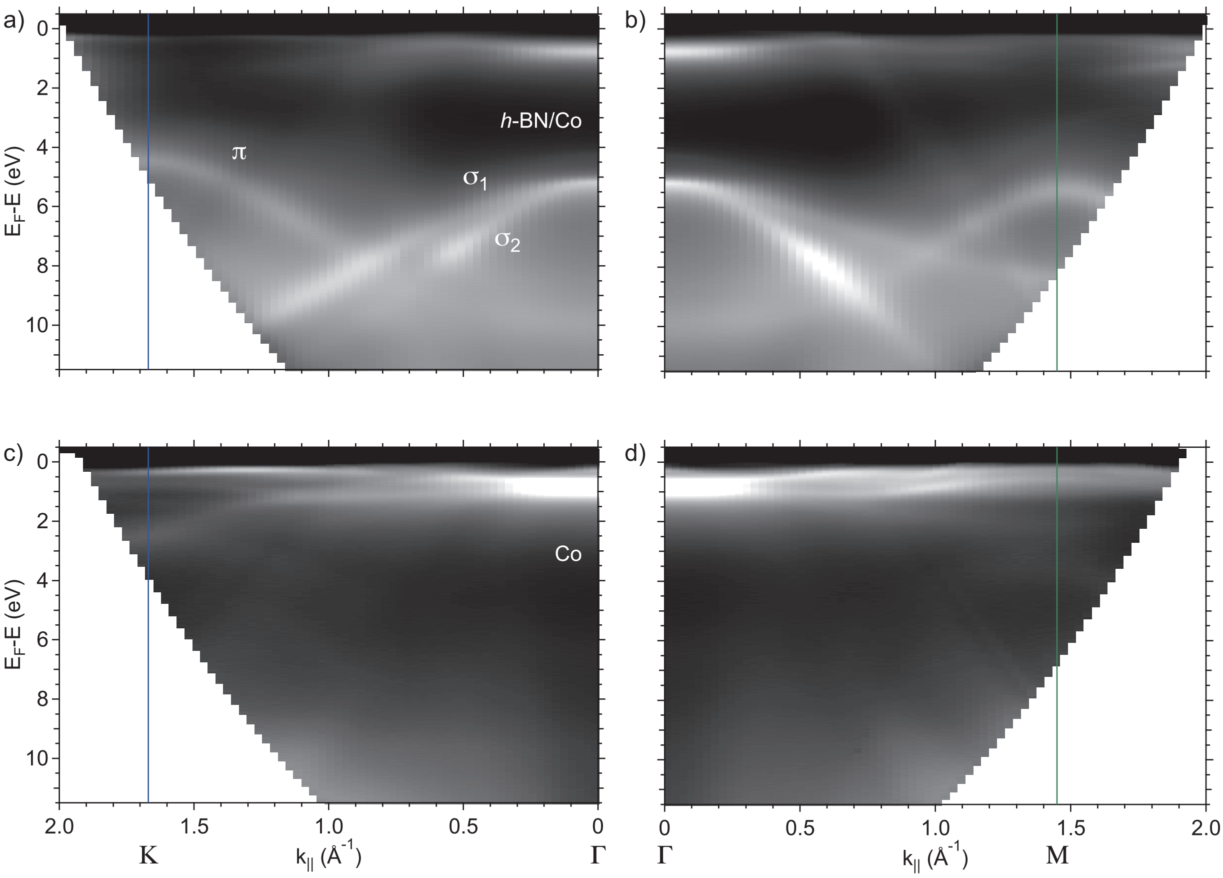

Figure 3.13: Band structure of *h*-BN/Co [a) and b)] and clean Co [c) and d)] measured with He I_α. a) and c) are measured along $\overline{\Gamma \mathrm{K}}$; b) and d) along $\overline{\Gamma \mathrm{M}}$. The *h*-BN derived bands σ_1, σ_2 and π are tagged in a). The vertical lines at $\overline{\mathrm{K}}$ and $\overline{\mathrm{M}}$ indicate the boundaries of the surface Brillouin zones of *h*-BN.

respectively] [103].

The electronic properties of a material are governed by electrons which have energies comparable to the Fermi energy ($E_\mathrm{F} \pm k_\mathrm{B}T$). Thus the Fermi surface of a metal carries important electronic structure information. In Figure 3.14 constant energy maps taken at the Fermi energy are displayed. The FSM of the clean Co features a rich pattern of sharp transitions with sixfold symmetry [Fig. 3.14 b)]. Starting from the $\overline{\Gamma}$ point of the surface Brillouin zone (SBZ) and moving outwards we first find six lobe-like features with their main weight located on a circle close to the $\overline{\Gamma}$ point. Second a distorted hexagon which is smaller than the indicated SBZ and rotated by 30° with its corners approaching the $\overline{\mathrm{M}}$ points attracts attention. Both are in agreement with Ref. [107] where they were assigned to sp-like majority electron bands. The arclike features in the second SBZs are replicas of the distorted hexagon from the first SBZ. The oval features centered at the $\overline{\mathrm{M}}$ points could be due to d-like minority hole pockets [105, 108]. Figure 3.14 a) shows the FSM of the Co surface covered with a single *h*-BN layer. Due to the fact that the *h*-BN layer is an insulator no new transitions appear and all Co related features are reduced in intensity. The distorted hexagon of the sp-like majority electron band is still visible as a sharp transition while

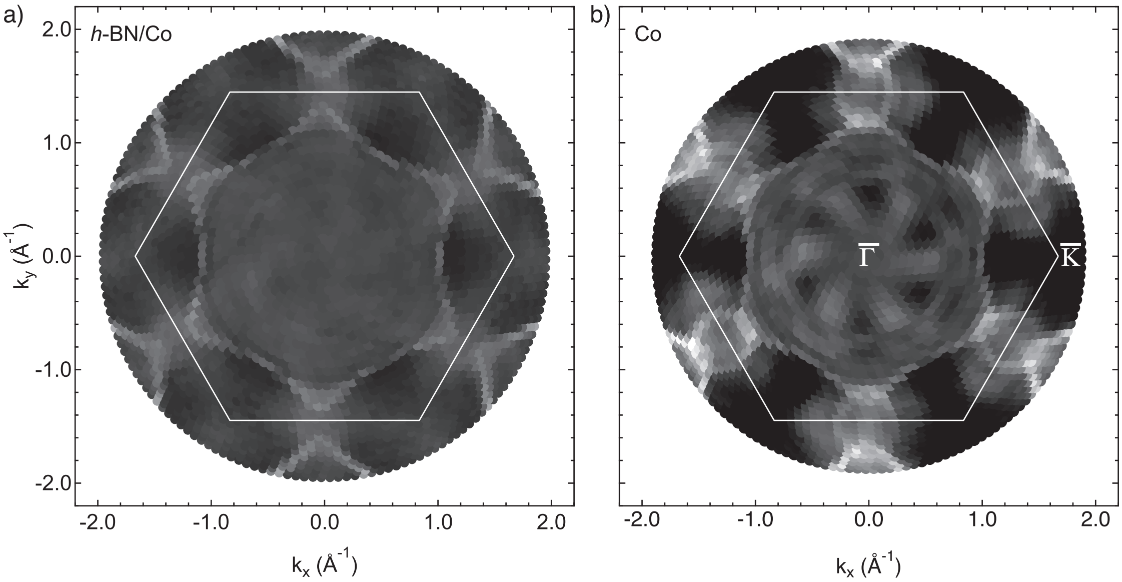

Figure 3.14: Fermi surface maps of a) *h*-BN/Co and b) Co measured with He I_α. The white hexagon indicates the surface Brillouin zone. Both FSMs have been φ-averaged for better visibility. In order to compensate the thereby generated error in the asymmetry ratios of a) and b) the grey scale of a) has been divided by a factor of 3.

all other Co features disappear in the background. However its size has increased: In the case of clean Co the transition is found at $k_{\|} = 0.94 \pm 0.02\,\text{Å}^{-1}$ on a line connecting $\overline{\Gamma}$ and $\overline{\text{K}}$, for the *h*-BN covered surface it is observed at $k_{\|} = 0.99 \pm 0.02\,\text{Å}^{-1}$. Again a final state effect does not explain the increase of this Fermi surface sheet: For increasing k_z the circumference of the Fermi surface sheet in the probed section of $\vec{k}$ space rather becomes smaller than larger [105, 108]. The increase of the sp-like majority electron sheet could be related to the above discussed shift of the Co 3d band towards lower binding energy. Eventually a charge redistribution from d to sp states occurs in the metal substrate. Due to their free electron-like behavior the majority sp electrons do not depend on the details of the crystal potential whereas the minority d states at the Fermi level are expected to depend strongly on the potential and therefore the arrangement of the ionic cores, that is the crystal structure [109]. If during growth the *h*-BN layer would induce stacking faults in the topmost Co layers a strong effect on the d band derived features of the FSM could be thought of. Also the effect of the *h*-BN induced polarization is expected to be stronger on the d band than on the sp bands.

3.3.3 Conclusions

We showed that on Co a single layer of *h*-BN can be grown and forms a perfect 1 × 1 commensurate structure. The dispersion of the sp^2-derived σ bands and π band has been presented. For the *h*-BN σ electrons a weak coupling to the substrate could be deduced from their vacuum level alignment. An unexpected increase of the Co majority Fermi surface sheet was found and at the same time the minority d band occupancy seems to be modified. In combination this could lead to an enhanced magnetic moment for *h*-BN/Co as compared to pure Co. The *h*-BN passivated Co is expected to have an increased stability against contamination as it had been observed for *h*-BN/Rh(111) [26]. Recently it was shown that also graphene forms perfect 1×1 overlayers on Co(0001) where a π band gap opens at the $\overline{\mathrm{K}}$ point of the BZ due to strong interactions of the graphene with the substrate [110]. A combined STM and DFT study confirms strong p_z-d C-Co hybridization [111]. Even though Co films of comparable thickness usually show out of plane magnetization a comparison of the VLEED spin asymmetry of Fe(001)-$p(1 \times 1)$-O and the two systems *h*-BN/Co and *g*/Co could be of interest. Maybe they could serve as inert and robust scattering targets.

3.4 Co clusters on the *h*-BN/Rh(111) nanomesh

The growth of surface supported metal clusters is not only important from fundamental aspects that is for example elucidating if metal clusters couple electronically and magnetically to their substrate and how this coupling depends on temperature or cluster size and shape. It is also relevant for technological applications, for example in the storage media sector. If magnetic materials could be used for the growth of nanometer sized ferromagnetic metal clusters on a robust template unmatched storage densities could be reached.

First supported metal nanocluster arrays have been fabricated by evaporating Ni and Co in UHV on the Au(111) herringbone reconstructed surface at room temperature at the beginning of the 1990's [112, 113]. In 1998 Huang *et. al* presented a method to grow metal clusters in the nanometer regime which required low temperatures ($T \leq 50\,\mathrm{K}$). A few layers of Xe were condensed on a (7×7) reconstructed Si(111) surface. Afterwards Ag was evaporated onto the Xe covered surface by molecular beam epitaxy (MBE). Upon annealing of the crystal the Xe desorbed and the clusters soft-landed onto the Si substrate. They called their new method buffer layer assisted growth (BLAG) [114]. For BLAG the formation of an ordered cluster array is not inherent but can be achieved if it is combined with the use of an appropriate substrate like the *h*-BN nanomesh [115]. More recent examples for self assembled metal nanocluster arrays are Ir clusters on *g*/Ir(111) where clusters of about 70 Ir atoms form hexagonal cluster lattices whose density depends on the Ir coverage [61]. Another one is a hexagonal metal-organic network on Ag(111) consisting of dicarbonitrile-polyphenyl molecules coordinated to Co centers (NC-Ph$_n$-CN)$_3$Co$_2$ where Fe atoms have been shown to selectively decorate either the molecules or the Co coordination nodes depending on the evaporation temperature [116].

While Co follows the Frank-van der Merwe (2D) growth mode on many metal surfaces [117] it has been shown to grow three-dimensional islands (Volmer-Weber growth mode) on *h*-BN/Ni(111) [118]. Hence the sum of the surface free energy of Co and the interface energy of Co and *h*-BN/Ni(111) must be larger than the surface free energy of *h*-BN/Ni(111). Presumably the same holds true for *h*-BN/Rh(111) since the surface free energy of *h*-BN/TM systems should be largely determined by the *h*-BN. The interesting question is whether the *h*-BN/Rh(111) nanomesh in addition exhibits *specific sites for the nucleation of the metal clusters*. With those it could serve as a robust template for the growth of highly ordered metal cluster arrays whose periodicity of 3.2 nm would lie well below the limit of what can be achieved with lithography at the present time. It would lead to a maximum nucleation site density of $1/A_{unitcell} = 1/\left(\sqrt{3}/2 \cdot a^2\right) = 0.11\,\mathrm{nm}^{-2} = 1.1 \cdot 10^{13}\,\mathrm{cm}^{-2}$.

In this section two completely different approaches to the growth of Co clusters on the *h*-BN/Rh(111) nanomesh are described: In the first part Co has been evaporated on *h*-BN/Rh(111) from a high purity Co cylinder (Sigma-Aldrich, 99.99 %) with a setup described elsewhere (Ref. [119]). In the second part the use of a molecular precursor for the growth of Co clusters on *h*-BN/Rh(111) is presented.

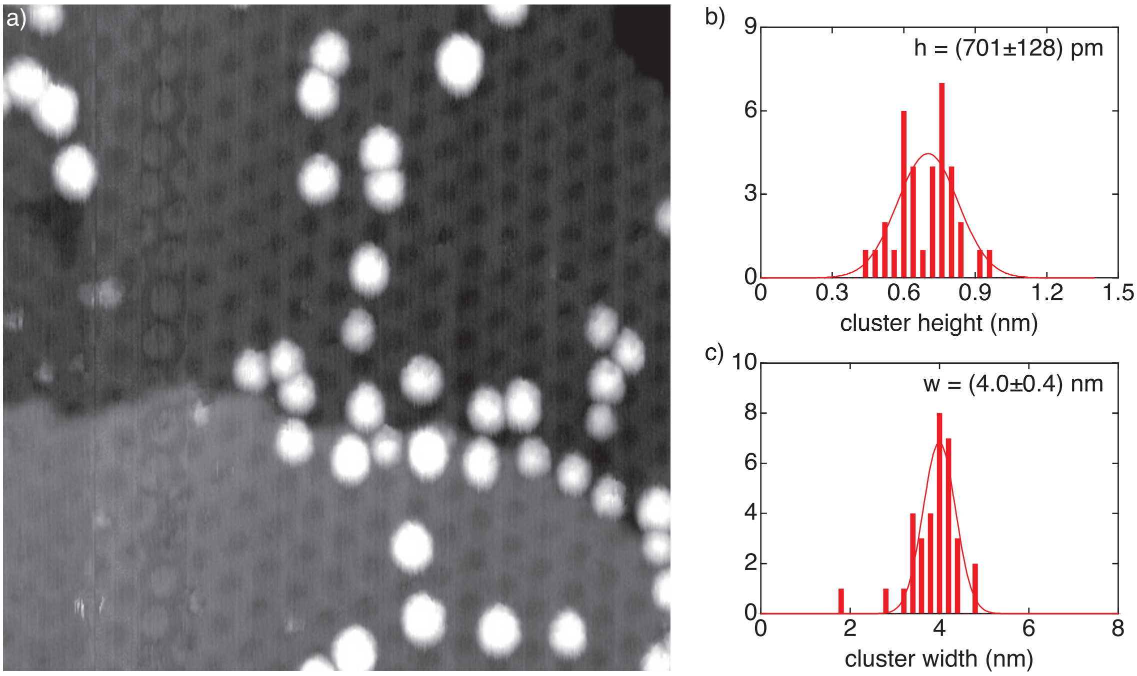

Figure 3.15: Room temperature STM data of the *h*-BN/Rh(111) nanomesh after room temperature evaporation of $\theta = 0.1\,\text{ML}$ Co. a) STM topography image: $50\,\text{nm} \times 50\,\text{nm}$, $V_s = +1.0\,\text{V}$, $I_t = 0.1\,\text{nA}$. b) and c) height and width distribution of the Co clusters from a) respectively.

3.4.1 Standard Co evaporation

Cluster formation at room temperature

In Fig. 3.15 a) a STM topography image of a preparation where $\theta = 0.1\,\text{ML}$ of Co had been evaporated on the as prepared room temperature *h*-BN/Rh(111) nanomesh with a rate of $0.01\,\text{MLmin}^{-1}$ is shown. The pressure during evaporation was about $p = 3 \cdot 10^{-8}\,\text{mbar}$. Two Rh(111) terraces covered with the corrugated single layer *h*-BN can be seen. In addition $N \approx 40$ clusters are found to occupy certain nanomesh pores. No clusters are found on the wires of the nanomesh. If we define a *filling factor* $\gamma = N/N_{pores}$ with the number of available nanomesh pores N_{pores} and the number of occupied nanomesh pores N we obtain a value of $\gamma = 0.15$ for this preparation.

XPS shows that the surface of the *h*-BN/Rh(111) after evaporation is partially covered with Co (Fig. 3.16) whose $2p_{3/2}$ core level binding energy is $E_b = 777.4\,\text{eV}$. This binding energy corresponds to that of pure Co metal [120]. The amount of C found on the surface after Co deposition is rather high (0.2 ML) and is most probably caused by an insufficiently degassed Co source since it decreased in advancing preparations. The O 1s signal was below the detection limit. Therefore the clusters must be Co metal clusters. A fit of a 2D Gaussian two each of the Co clusters in Figure 3.15 a) yields their height and their width distributions as they are shown in Figure 3.15 b) and c) respectively. The Co clusters have a mean height of $\overline{h} = 701 \pm 128\,\text{pm}$ and a mean width of $\overline{w} = 4.0 \pm 0.4\,\text{nm}$.

Annealing the sample of Figure 3.15 in UHV to $T = 650\,\text{K}$ for about 5 min results in somewhat smaller Co clusters ($\overline{h} = 609 \pm 181\,\text{pm}$ and $\overline{w} = 3.1 \pm 0.4\,\text{nm}$) with a filling factor of $\gamma = 0.18$

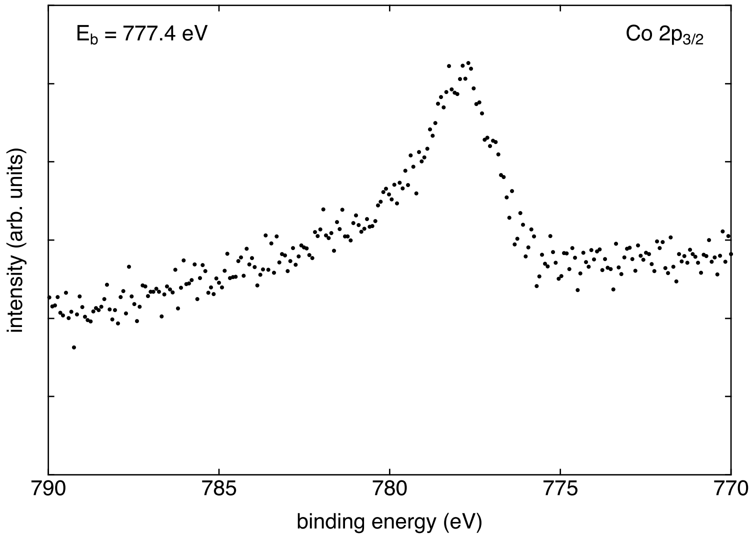

Figure 3.16: XPS of the preparation shown in Fig. 3.15 excited with Al K_α. The binding energy of the Co $2p_{3/2}$ core level shows that the clusters consist of pure Co.

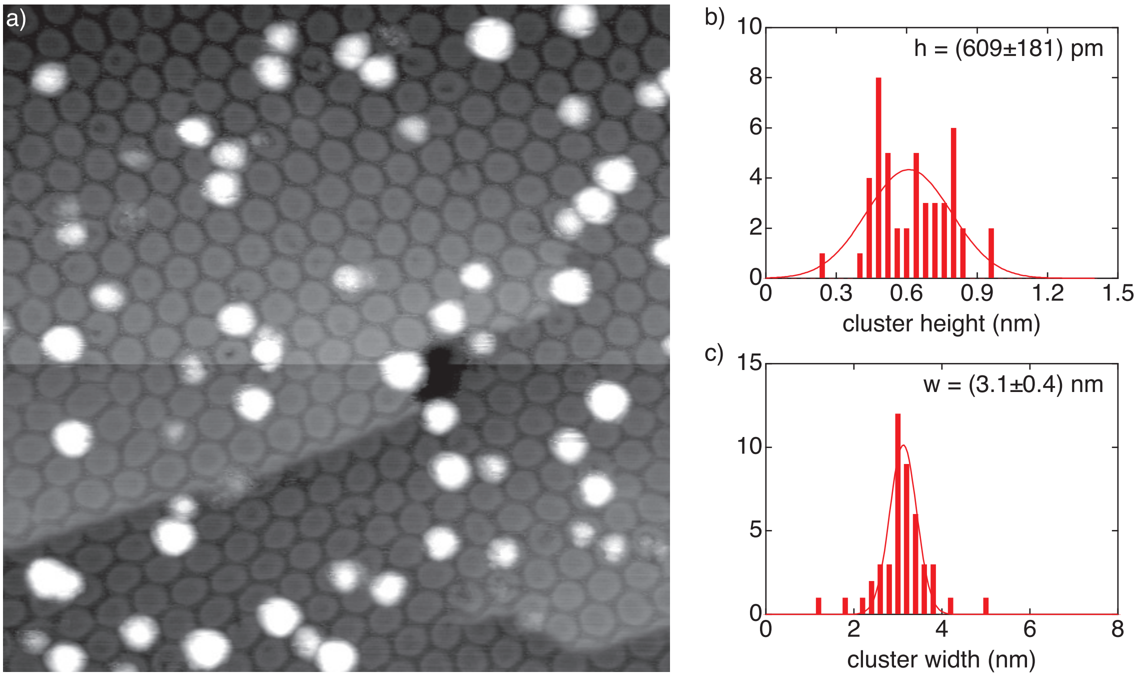

Figure 3.17: Room temperature STM data of the sample in Fig. 3.15 after annealing to $T = 650\,\mathrm{K}$. a) STM topography image: $50\,\mathrm{nm} \times 50\,\mathrm{nm}$, $V_s = +0.8\,\mathrm{V}$, $I_t = 0.2\,\mathrm{nA}$. b) and c) height and width distribution of the Co clusters from a) respectively.

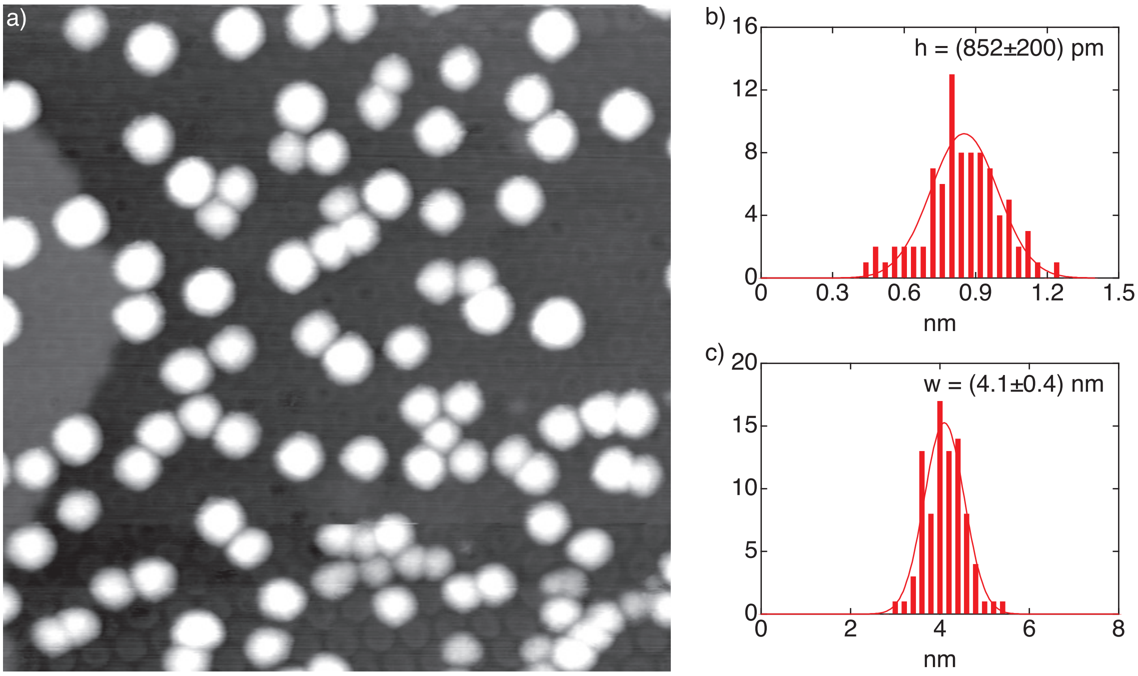

Figure 3.18: Room temperature STM data of the nanomesh after evaporation of $\theta = 0.2\,\mathrm{ML}$ Co at $T = 215\,\mathrm{K}$. a) STM topography image: $50\,\mathrm{nm} \times 50\,\mathrm{nm}$, $V_s = +1.0\,\mathrm{V}$, $I_t = 0.3\,\mathrm{nA}$. b) and c) height and width distribution of the Co clusters from a) respectively.

which is similar to that after evaporation (Fig. 3.17). This suggests that Co atoms desorb into the vacuum during the annealing process. Ostwald ripening seems not to occur at that temperature. The h-BN layer survives the annealing without evident damage. No regions where Co atoms could penetrate the nanomesh and form intercalated islands could be observed.

Cluster growth at $T \leq 215\,\mathrm{K}$

The kinetics of the cluster growth process strongly influence the morphology and the spatial distribution of the clusters. Hence the temperature is a crucial parameter for the formation of clusters since it rules the diffusion processes of ad-atoms on the substrate after they have landed from the gas phase.

After the first room temperature experiments we started to evaporate Co on the h-BN/Rh(111) nanomesh at temperatures $T \leq 300\,\mathrm{K}$.

Fig. 3.18 shows STM data of $\theta = 0.2\,\mathrm{ML}$ Co evaporated onto the nanomesh at $T = 215\,\mathrm{K}$ with a rate of $0.01\,\mathrm{ML\,min^{-1}}$ and a pressure of about $p = 8 \cdot 10^{-9}\,\mathrm{mbar}$. In addition to the h-BN nanomesh over-growing a Rh(111) terrace step $N = 98$ Co clusters can be observed. This results in a filling factor of $\gamma = 0.35$ which demonstrates a strong temperature dependence of the Co cluster density. P. Buluschek found the strongest temperature dependence of the clusters density in the temperature range between $T = 200\,\mathrm{K}$ and $T = 400\,\mathrm{K}$ [121]. The clusters have a mean height and width of $\overline{h} = 852 \pm 200\,\mathrm{pm}$ and $\overline{w} = 4.1 \pm 0.4\,\mathrm{nm}$, respectively. The mean width is similar to the preparation at room temperature while the mean height is about 20 % bigger. The

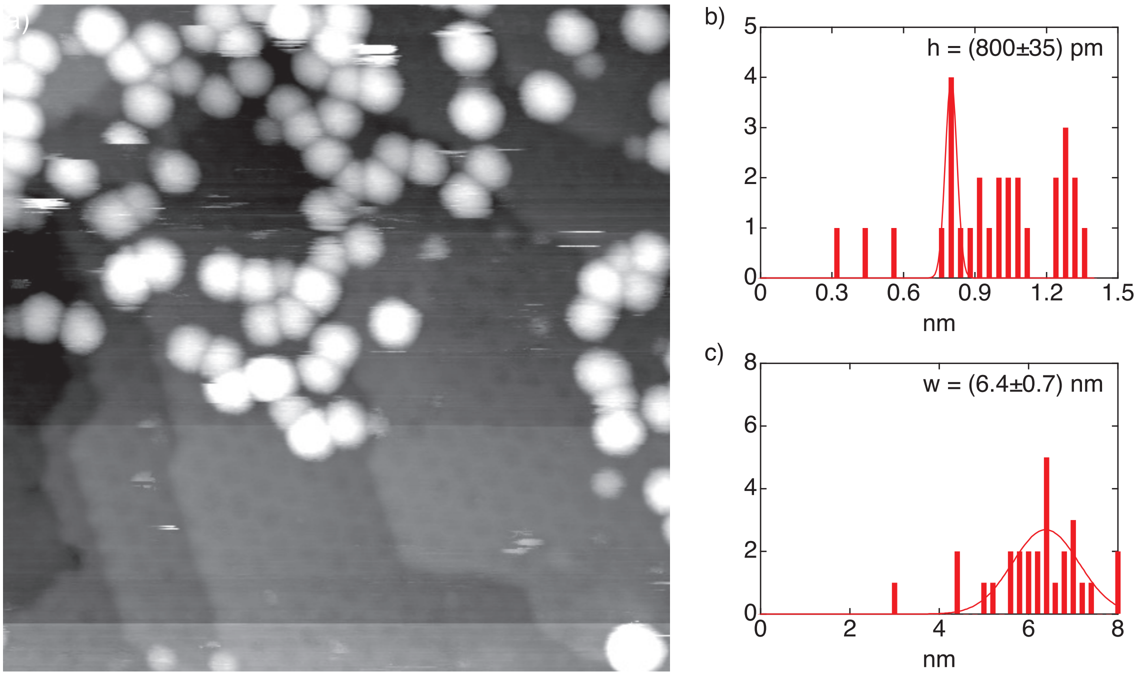

Figure 3.19: Room temperature STM data of the nanomesh after evaporation of $\theta = 0.5\,\mathrm{ML}$ Co at $T = 207\,\mathrm{K}$. a) STM topography image: $75\,\mathrm{nm} \times 75\,\mathrm{nm}$, $V_s = +1.0\,\mathrm{V}$, $I_t = 0.5\,\mathrm{nA}$. b) and c) height and width distribution of the Co clusters from a) respectively.

Co clusters accordingly tend to grow higher instead of growing wider which could be due to a lateral barrier for the cluster growth imposed by the nanomesh.

The lowest sample temperature which could be achieved in our setup with LN_2 cooling through a flow cryostat was about $T = 190\,\mathrm{K}$. Close to that temperature we wanted to investigate the effect of the coverage on the cluster morphology and density. A preparation at $T = 207\,\mathrm{K}$ where Co was evaporated at a rate of $0.01\,\mathrm{MLmin}^{-1}$ and a pressure of $p = 4 \cdot 10^{-8}\,\mathrm{mbar}$ is shown in Fig. 3.19. Several Rh(111) terraces covered by the *h*-BN nanomesh can be seen. In addition $N = 82$ Co clusters can be observed leading to a filling factor of $\gamma = 0.13$ which is rather low for the deposition temperature. Maybe a significant number of Co clusters has been swept away by the STM tip during the acquisition of the image due to the rather high tunneling current of $I_t = 0.5\,\mathrm{nA}$. Considering the mean cluster height of $\overline{h} = 800 \pm 35\,\mathrm{pm}$ and the mean cluster width of $\overline{w} = 6.4 \pm 0.7\,\mathrm{nm}$ together with the Co coverage of $\theta = 0.5\,\mathrm{ML}$ as measured with XPS this could also explain the low filling factor. It has to be said that scanning clusters with an aspect ratio of about $10\,\text{Å} : 30\,\text{Å}$ is not a standard measurements with an STM and might lead to aberrations and interactions with the measured entities. Usually abrupt height changes of about $3\,\text{Å}$ at most can still be resolved at an occurrence of about $0.5\,\mathrm{nm}^{-1}$, e.g. on vicinal metal surfaces [122]. In the case of the Co clusters on the *h*-BN/Rh(111) nanomesh we have to deal with height changes of the order of $10\,\text{Å}$ at a similar frequency. This has to be taken into account for the apparent widths of the Co clusters as determined by STM – most probably the true width is considerably smaller. In addition it may lead to strong interactions of the STM tip with the scanned metal clusters.

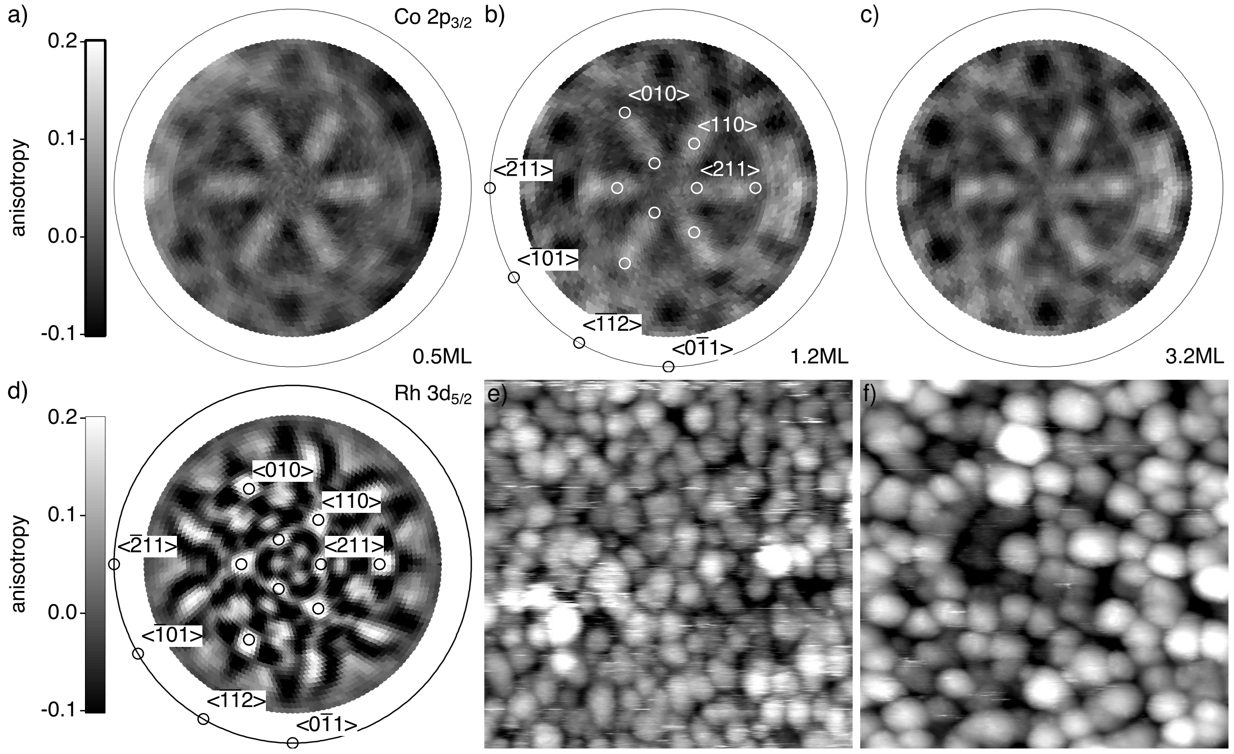

Figure 3.20: a)–c) Co $2p_{3/2}$ XPD patterns of various Co cluster coverages (0.5 ML, 1.2 ML and 3.2 ML, respectively) on the *h*-BN/Rh(111) nanomesh evaporated at $T = 200\,\mathrm{K}$. The clear sixfold rotational symmetry of the radial stripe pattern indicates azimuthal ordering of the Co clusters. d) Rh $3d_{5/2}$ XPD pattern of the 1.2 ML Co coverage preparation in b). The open circles in b) an d) represent the forward focusing directions of the first, second and third nearest neighbors of the fcc substrate ($\langle 110\rangle$, $\langle 010\rangle$ and $\langle 211\rangle$ directions respectively). e) and f) are STM topography images (both $50 \times 50\,\mathrm{nm}^2$) of the preparations in b) and c) respectively.

There are also competitive ways for the fabrication of metal cluster arrays on the *h*-BN/Rh(111) nanomesh: Recently filling factors of $\gamma = 0.7$ were achieved for Co clusters using repeated BLAG cycles [76].

Azimuthal ordering of the Co clusters

From STM we know that upon evaporation at room temperature as well as at about $T = 200\,\mathrm{K}$ hemispherical Co clusters evolve on the *h*-BN/Rh(111) nanomesh. Their crystallographic orientation with respect to the substrate however could not be deduced from the STM measurements since the Co atoms aggregate to clusters even at low coverages. Due to their height to width ratio of about one third which is fairly large for the fast scanning tip of the STM the detailed two dimensional shape of the first Co atom layer could not be resolved. Hence we used another method to determine the orientation of the Co clusters on the substrate.

Figure 3.20 shows XPD patterns of several preparations where Co clusters were grown on the *h*-BN/Rh(111) nanomesh at about $T = 200\,\mathrm{K}$. The XPD patterns of the photoelectrons which originate from the Co $2p_{3/2}$ core level show a sixfold radial stripe pattern for all measured Co

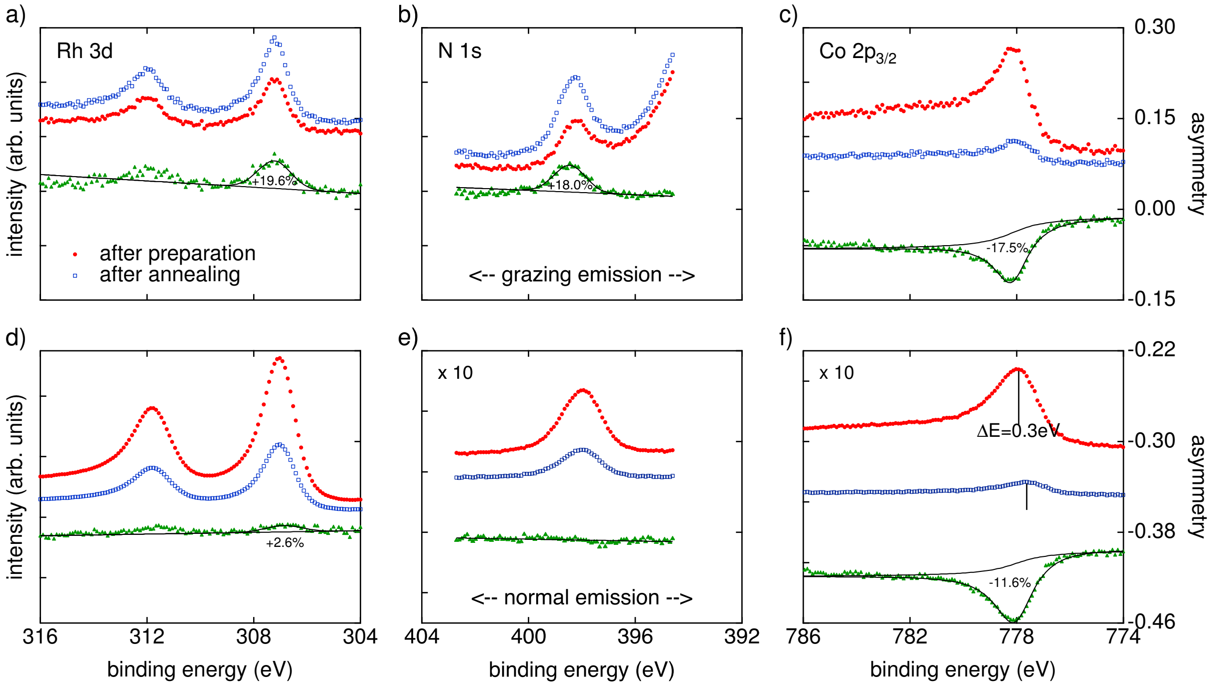

Figure 3.21: Mg K_α excited XPS of the preparation in Fig. 3.19 before (filled red circles) and after (open blue rectangles) exposure to 320 L ($t = 360\,\mathrm{s}$) of borazine at $T = 1010\,\mathrm{K}$ measured in grazing ($\vartheta = 80°$) and normal emission [a)-c) and d)-f) respectively]. Filled green triangles display the asymmetry of the core level spectra before and after exposure.

coverages [Fig. 3.20 a)-c)]. From a comparison to the simultaneously measured Rh $3d_{5/2}$ core level XPD patterns it can be concluded that the Co clusters lock in to the orientation of the *h*-BN layer. The fact that the Co $2p_{3/2}$ XPD patterns show stripes rather than pronounced forward scattering peaks can be caused by two scenarios: Either there exist two equivalent cluster orientations on the nanomesh rotated by 60° or the growth mode of the individual clusters is neither completely fcc, nor completely hcp.

Capping of Co clusters with BN

In order to study the magnetic properties of the Co clusters on the nanomesh at our institute we had to take our samples out of the UHV system and transfer them to a magnetometer where they would reside in low vacuum conditions. To prevent the Co clusters from oxidation we tried to cap them with a protective layer of *h*-BN after deposition onto the *h*-BN/Rh(111).

Figure 3.21 shows x-ray photoelectron spectra of the Rh 3d, the N 1s and the Co $2p_{3/2}$ core levels before and after annealing of the *h*-BN/Rh(111) nanomesh covered with $\theta = 0.5\,\mathrm{ML}$ of Co clusters from Figure 3.19 to $T = 1010\,\mathrm{K}$ including exposure to 320 L of borazine ($t = 360\,\mathrm{s}$). Three likely processes may occur during this procedure:

1. The preferred scenario would be that the Co clusters act as catalysts for the formation of *h*-BN and consequentially become covered by a thin layer of *h*-BN. This hardly affects the Rh core level photoelectron intensities I_{Rh} in normal or grazing emission XPS since almost the

same surface area is covered by adsorbates before and after the exposure. However the N and the B core level photoelectron intensities I_{N} and I_{B} would increase in normal emission by an amount that is proportional to the initial Co coverage. In grazing emission this effect would be strongly enhanced. An inverse behavior is expected for the Co core level photoelectron intensities I_{Co} in both normal and grazing emission with an enhancement in the latter.

2. Co atoms from the Co clusters desorb into the vacuum. This leads to a diminution of the cluster size and hence in normal emission a decreased I_{Co} would be observed. I_{Rh}, I_{N} and I_{B} would show a minor increase due to the lower Co surface coverage. In grazing emission the formerly described effects would be amplified because of the enhanced surface sensitivity.

3. A partial or complete intercalation of Co atoms between the *h*-BN and the topmost Rh(111) layer occurs. In this case I_{Rh} is reduced in normal emission because a larger surface area is covered by Co atoms and damps the photoelectron signal from the substrate. I_{N} would increase since a lot of *h*-BN moves from laying below Co clusters to above. The effect on I_{Co} is not obvious and depends on the initial morphology of the Co cluster. Most probably it will decrease since the intercalated Co would now be covered by the *h*-BN layer. The strongest effect in grazing emission is expected for I_{N} and I_{B} because *h*-BN would now be the dominant surface compound.

Of course a combination of these effects is also possible but will be impossible to distinguish by XPS alone. The presented experimental data for normal emission [Fig. 3.21 d)-e)] show a minimal increase of I_{Rh} and no change of I_{N} while I_{Co} is strongly reduced. In grazing emission [Fig. 3.21 a)-c)] both I_{Rh} and I_{N} are enhanced. The reduction of I_{Co} is even more pronounced than in normal emission. All of this observations match the second case in which Co atoms desorb from the Co cluster into the vacuum. This process is activated by the high temperature during annealing as can be seen in Figure 3.17. A pure *h*-BN capping scenario can be ruled out from the fact that I_{N} changes accordingly to I_{Rh} for both emission angles. The intercalation of Co is also unlikely to be the only process since for that case I_{N} in grazing emission should increase much more compared to I_{Rh}. But there is still the possibility that only a part of the Co intercalates between the outermost Rh(111) substrate layer and the *h*-BN layer. This had been observed earlier for Co on *h*-BN/Ni(111) [118] and very recently also for Co on *h*-BN/Rh(111) if Co is evaporated on the as prepared *h*-BN/Rh(111) nanomesh in a mild O_2 atmosphere ($p_{O_2} = 8 \cdot 10^{-9}$ mbar) [100]. From the phase diagram a binary alloy of Co and Rh also seems to be possible [123].

In conclusion the formation of a protective *h*-BN capping for the Co metal clusters has not been achieved.

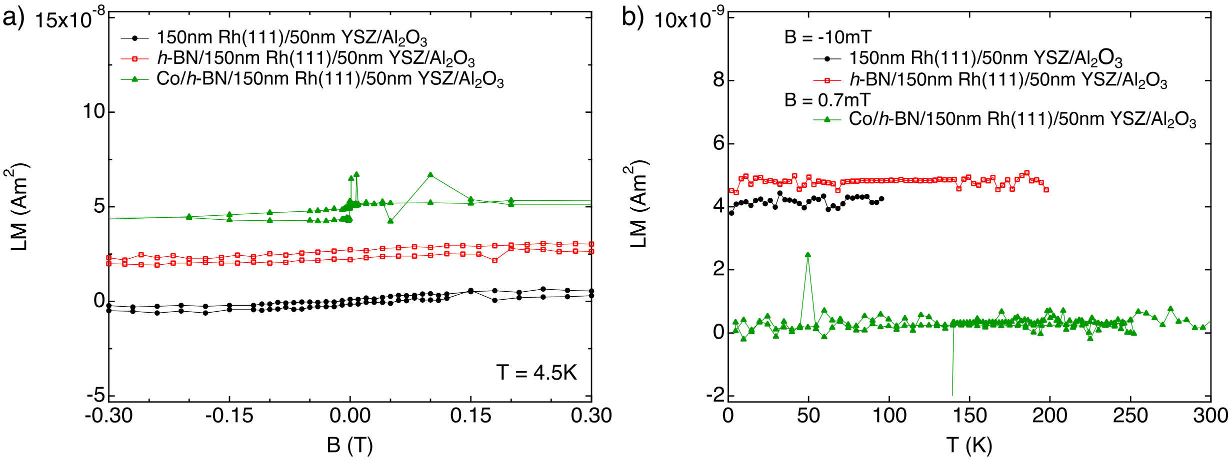

Figure 3.22: Comparison of zero field cooled SQUID magnetization measurements of 150 nm Rh(111) film samples as received (black filled circles), covered with a *h*-BN nanomesh (red open squares) and decorated with 0.2 ML of Co (green filled triangles). a) Full magnetization curves taken at $T = 4.5\,\mathrm{K}$ after subtraction of the linear diamagnetic background of the sapphire substrate. The three curves are vertically offset for clarity. b) Temperature sweep in a static field of $B = -10\,\mathrm{mT}$ (0.7 mT for the Co covered sample).

Magnetic properties of the Co clusters

The magnetic properties of the Co covered *h*-BN/Rh(111) nanomesh sample which had been treated by the high temperature borazine exposure (0.2 ML Co left) were investigated by means of magnetization measurements in a MPMS[3] in the group of Prof. H. Keller[4]. This device is a commercial superconducting quantum interference device (SQUID) in a ^{4}He bath cryostat equipped with a superconducting magnet. The sensitivity for longitudinal magnetic moments along the magnetic field axis is estimated to be about $10^{-8}\,\mathrm{Am}^2$ which corresponds to about $10^{15}\,\mu_\mathrm{B}$.

In Figure 3.22 reference measurements for a Rh(111) film sample as it was received from S. Gsell [125] with and without a *h*-BN nanomesh are displayed together with the 0.2 ML Co on *h*-BN/Rh(111) sample. Figure 3.22 a) shows the full magnetization curves of all three measurements taken at 4.5 K after subtraction of a linear background. This linear background is attributed to the diamagnetic properties of the sapphire (Al_2O_3) substrate. For all curves a paramagnetic Langevin behavior of the thin Rh metal film can be observed. Apart from that no effect of either the *h*-BN or the deposited Co is noticeable. The same observation is made for the temperature sweeps in Figure 3.22 b) which had been taken in a static field of $-10\,\mathrm{mT}$ (0.7 mT) in the case of the reference measurements (the Co covered sample).

An estimation of the detection limit of the SQUID device shows that a coverage corresponding to about 1 ML of ferromagnetic Co on the $10 \times 10\,\mathrm{mm}^2$ substrate should be detectable. This means that from the conducted measurements it can not be decided if either the Co clusters on

---

[3] Magnetic Properties Measurement System, Quantum Design

[4] with the kind help of S. Weyeneth [124]

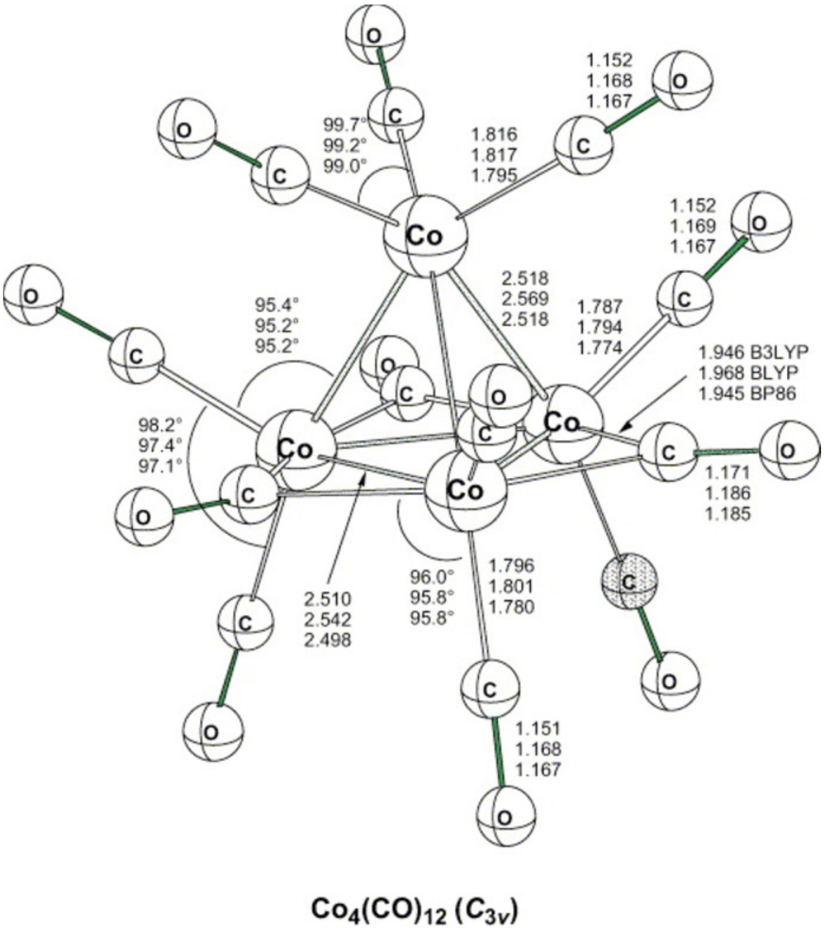

Figure 3.23: Structural model of tetracobaltdodecacarbonyl [$Co_4(CO)_{12}$] as it results from DFT calculations [126].

the *h*-BN/Rh(111) nanomesh are still superparamagnetic or the sensitivity of the measurement is not high enough. However magneto optical Kerr effect (MOKE) measurements in the group of Prof. H. Brune, Ecole Polytechnique Fédérale de Lausanne[5] at $T = 60\,\mathrm{K}$ in a field of about $B = 350\,\mathrm{mT}$ with Co coverages of up to 0.25 ML also did not show any signal above the background level. Since that MOKE setup in principle is sensitive enough for such small amounts of ferromagnetic material the conclusion that the Co clusters on the *h*-BN/Rh(111) nanomesh are still superparamagnetic stands to reason.

3.4.2 Evolution of Co clusters using a cobalt carbonyl precursor

Analyzing the results of our previous experiments and the findings of P. Buluschek [121] which also showed that Co does form clusters upon evaporation on the *h*-BN/Rh(111) nanomesh but that those are not exclusively occupying nanomesh pores, we were looking for a new route to deposit Co clusters on the *h*-BN/Rh(111) nanomesh. Its trapping mechanism for polarizable molecules seemed likely to be useful for that purpose [27]. Hence with the help of C. Egler from

---

[5] carried out by P. Buluschek [121]

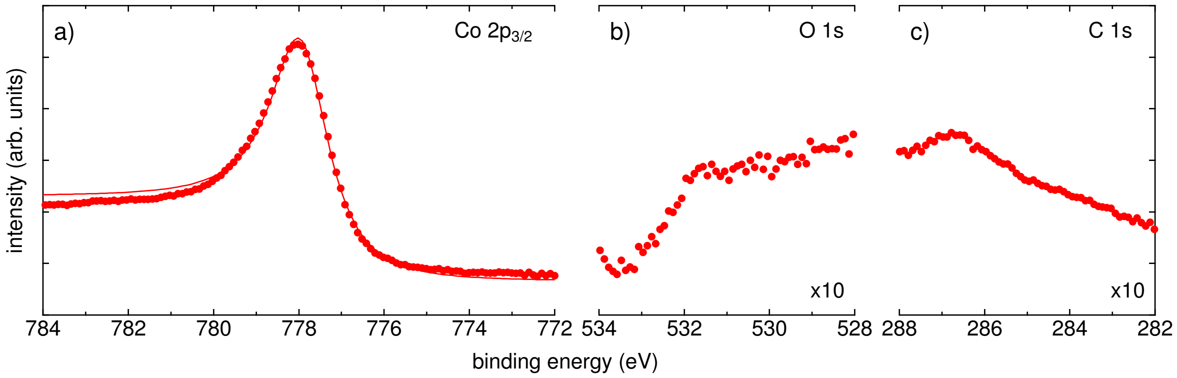

Figure 3.24: Mg K_α XPS data of *h*-BN/Rh(111) nanomesh after exposure to tetracobaltdodecacarbonyl [$Co_4(CO)_{12}$] at room temperature for t=120 min. The regions for the Co $2p_{3/2}$, O 1s and C 1s core level intensities are displayed [a), b) and c), respectively] where the intensity scale of the latter two is expanded by a factor of ten.

the group of Prof. H. Berke at the Institute of Inorganic Chemistry at our university we searched for a suitable metal cluster precursor in the form of molecules. Since P. Buluschek showed that Co clusters up to the pentamer diffuse on the *h*-BN/Rh(111) nanomesh [121], we intended to use the hexanuclear cobaltcarbonyl [$Co_6(CO)_{16}$] - a transition metal carbonyl molecule with six Co atoms in the center [127]. But that molecule turned out to decompose already at room temperature [128]. So we decided to use tetracobaltdodecacarbonyl [$Co_4(CO)_{12}$] which has a core of four Co atoms and is stable up to $T \approx 80°C$ [126, 128] (see Fig. 3.23). Details about the handling of the $Co_4(CO)_{12}$ molecules can be found in Appendix D.

Carbonyl deposition at room temperature

In a first set of experiments we exposed as prepared room temperature *h*-BN/Rh(111) nanomesh to $Co_4(CO)_{12}$. Due to the low decomposition temperature of $Co_4(CO)_{12}$ we could only mildly bake the carbonyl source which resulted in a very high background pressure when opening the valve to the source. Figure 3.24 shows XPS data of an exposure of the nanomesh to $p \approx 4 \cdot 10^{-6}$ mbar for $t = 120$ min. The presence of cobalt can clearly be deduced from Figure 3.24 a) and adds up to a coverage of about $\theta = 0.7$ ML. The binding energy of the Co $2p_{3/2}$ core level electrons of $E_b = 777.9$ eV as determined from a fit of a Doniach-Sunjic peak shape corresponds to that of Co metal. Only a minor amount of 0.1 ML of oxygen [Fig. 3.24 b)] and no detectable amount of carbon [Fig. 3.24 c)] is found on the surface after the exposure. The peak in Figure 3.24 c) at $E_b \approx 287$ eV is attributed to an artifact of the non monochromatized Mg K_α x-ray source since it is also present on the clean Rh(111) surface (data not shown). This is a remarkable result as it provided a cleaner sample than for most of the standard evaporations which had been performed. It is all the more interesting if we consider the initial stoichiometry of the precursor with three carbonyl groups per cobalt atom. The fact that the photoionization cross-section for the C 1s (O 1s) core level electron is about twelve (four) times smaller than the one for the Co $2p_{3/2}$ core level electron in the case of Mg K_α radiation ($h\nu = 1253.6$ eV) [129] is

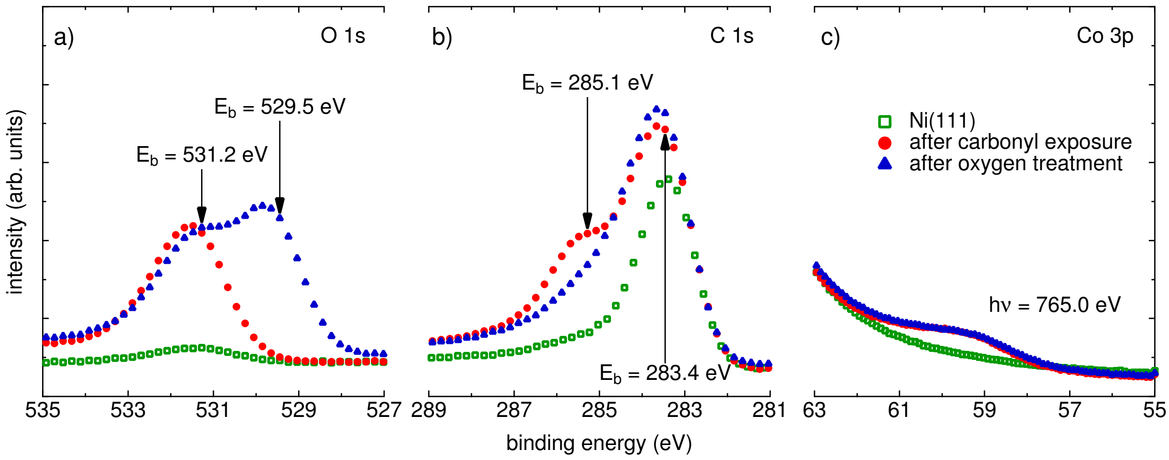

Figure 3.25: XPS data of a Ni(111) surface before (open green rectangles) and after exposure to $Co_4(CO)_{12}$ at room temperature for t=76 min (filled red circles). The photon energy was set to $E = 765.0$ eV. Filled blue triangles correspond to data taken after additional exposure to 48 L of O_2. The regions for the O 1s, C 1s and Co 3p core level intensities are displayed [a), b) and c), respectively].

not sufficient to explain the lacking photoelectron intensity for this two elements. The carbonyl groups must have been stripped off the Co metal core during the deposition process. The separation of the carbonyl groups from the tetrahedral Co core most probably took place upon or after adsorption of the $Co_4(CO)_{12}$ on the *h*-BN/Rh(111) nanomesh followed by immediate desorption of the CO from the inert *h*-BN interface. This finding is substantiated by a small experiment where we could use a few remaining hours of a beamtime at the Swiss Light Source. In this experiment the (111) face of a Ni yoke crystal which had been cleaned a few days before has been exposed to $Co_4(CO)_{12}$ at room temperature. In Figure 3.25 XPS data of the Ni(111) crystal before (open green rectangles) and after exposure to $p \approx 1 \cdot 10^{-7}$ mbar for totally $t = 72$ min (filled red circles) is shown. A clear increase in the amount of Co on the Ni(111) surface can be seen from Fig. 3.25 c) ($\theta \leq 0.1$ ML). The crystal had not been very clean before the exposure [Fig. 3.25 b)]. However the amounts of oxygen and carbon increase by about 0.3 ML [Fig. 3.25 a)] and 0.8 ML [Fig. 3.25 b)], respectively during cobaltcarbonyl exposure. The values for the O 1s binding energies after subsequent dosing of 48 L O_2 as determined from a fit of two Gaussians of $E_b = 531.2$ eV and $E_b = 529.5$ eV suggest the coexistence of CO molecules bonding to the Ni(111) substrate atoms with the carbon atom and pure oxygen probably forming a partial 2×2 reconstruction [130]. The C 1s peak at $E_b = 285.1$ eV also fits well into this model.

In conclusion the *h*-BN layer plays an important role for the surface chemistry of the carbonyl molecule on the transition metal surface.

Carbonyl deposition at $T \leq 150$ K

Figure 3.26 shows a STM image of the *h*-BN/Rh(111) nanomesh taken at room temperature. The sample had been freshly prepared and without further treatment exposed to tetracobaltdodecacar-

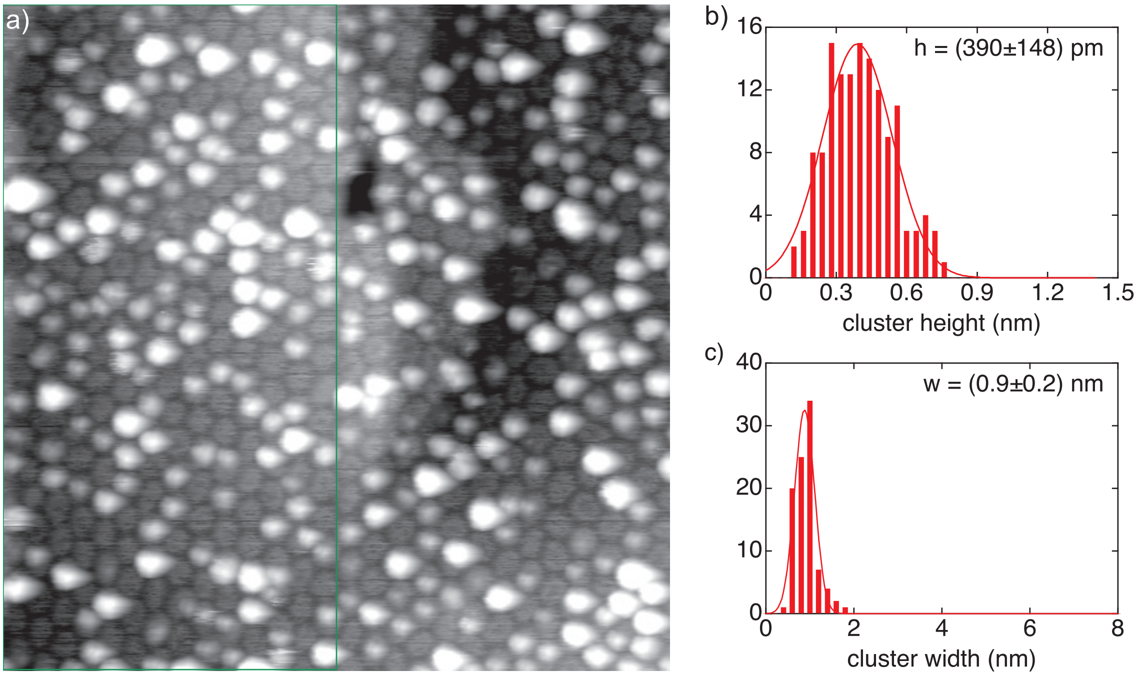

Figure 3.26: Room temperature STM data of the *h*-BN/Rh(111) nanomesh after $Co_4(CO)_{12}$ exposure at $T = 143\,K$ showing Co clusters occupying exclusively nanomesh pores. a) STM topography image: $68\,nm \times 68\,nm$, $V_s = -0.8\,V$, $I_t = 80\,pA$. b) and c) height and width distribution of 137 Co clusters within the green ROI in a) respectively.

bonyl at a pressure of $p = 4 \cdot 10^{-11}$ mbar for $t = 46$ min while being held at $T = 140\,K$. During the exposure no useful STM images could be recorded since the STM tip changed very frequently and soon lost its resolution. Several hours after the sample had been warmed up to room temperature the same tip could resolve the topography of the nanomesh again. Surprisingly we found the nanomesh to be covered with about $N = 285$ Co clusters which almost exclusively occupied the pores of the nanomesh. Their average width and height has been determined by fitting a two dimensional Gaussian to each of the clusters which can be found in the green ROI of Fig. 3.26 a) and turns out to be $\overline{w} = (0.9 \pm 0.2)\,nm$ and $\overline{h} = (390 \pm 148)\,pm$ respectively. The width of the clusters is significantly smaller compared to that of the Co clusters on the *h*-BN/Rh(111) nanomesh which had been grown with the standard evaporation method from a heated pure Co cylinder. The height is about a factor of two smaller. However the filling factor of $\gamma = 0.56$ is fairly high so that the small Co clusters could be suitable as nucleation centers for further cluster growth by MBE.

T (K)	θ (ML)	γ	$\overline{h}$ (pm)	$\overline{w}$ (nm)
300	0.1	0.15	701 ± 128	4.0 ± 0.4
215	0.2	0.35	852 ± 200	4.1 ± 0.4
207	0.5	0.13	800 ± 350	6.4 ± 0.7
143 (carbonyls)		0.56	390 ± 148	0.9 ± 0.2

Table 3.2: Co cluster growth parameters for the above discussed preparations: sample temperature T, coverage θ, filling factor γ, mean cluster height $\overline{h}$ and mean cluster width $\overline{w}$.

Chapter 4

Summary and Outlook

The *h*-BN/Rh(111) nanomesh is an extremely robust template for polarizable entities [26, 27] with a superlattice constant of 3.2 nm [31]: It is inert and remains clean at ambient conditions [26]. We saw that it is stable in aqueous solutions and may be non-destructively imaged by electrolytic *in situ* STM if kept at small potentials [36]. In ultra high vacuum (UHV) it was found to decompose at temperature as high as 1100 K [31]. Water molecules are among the most interesting molecules which we could trap in the ‘pores’ of the nanomesh. At low temperatures ($T = 50\,\mathrm{K}$) nano-ice crystals with a bilayer honeycomb crystal lattice were found to exclusively condense in the ‘pores’ while on the ‘wires’ a low-density gas phase exists [131].

On Ru(0001) where the *h*-BN nanomesh turned out to grow in a similar manner but with less long-range order [21] a superlattice constant of 3.5 nm was found [63]. However for its metallic analog *g*/Ru(0001) a surprisingly large superstructure unit cell of 25×25 *g* units on 23×23 Rh atoms was determined by the experiment [62]. We could demonstrate a corrugated electrostatic potential landscape above *g*/Ru(0001) similar to *h*-BN/Rh(111) and thus prove that corrugated single sp^2 layers on transition metals may act as templates independent from their metallicity [38] (Sec. 3.1).

A proof of principle for an interesting approach to switch the surface texture of these nano-templates and thus their functionality has been achieved by the reversible intercalation of hydrogen between *h*-BN and Rh(111). With hydrogen intercalated the corrugation of the sp^2 layer vanishes and so do its peculiar spectroscopic features (Sec. 3.2).

As an application of the *h*-BN/Rh(111) nano-template we investigated the effect of the nanomesh on the formation of Co clusters by MBE. With Co metal as a precursor separated hemispherical Co clusters were found on the *h*-BN/Rh(111) after evaporation. Unfortunately it turned out that the energy difference for cluster formation in the ‘pores’ and on the ‘wires’ seems to be rather small. However using a polarizable Co containing carbonyl molecule we could deposit small Co nucleation centers exclusively in the ‘pores’ of the nanomesh. This may present a possible route to well ordered metal cluster arrays. But first measurements of the magnetic properties of the Co clusters formed by the standard method did not yield any ferromagnetic signature (Sec. 3.4).

In order to complete the *g*, *h*-BN, Rh(111) and Ru(0001) quartet it would be desirable to investigate the properties of *g*/Rh(111) and compare them to *h*-BN/Rh(111), *g*/Ru(0001) and *h*-BN/Ru(0001) (Sec. 3.1). The core level spectroscopy data of Preobrajenski *et al.* [24] which show big similarities between *g* grown on Ru(0001) and on Rh(111) call for completion with valence band spectroscopy and STM. As a first step into that direction an easier way to prepare *g*/Rh(111) than it is described by Müller *et al.* [25] has to be tested. A first experiment using ethene (C_2H_4) as a precursor failed although it worked perfectly on Ru(0001). According to Ref. [24] propene (C_3H_6) should work as a precursor and hence is proposed to be tested next.

An affirmation of the template functionality of the two systems *g*/Ru(0001) and *g*/Rh(111) by site-specific adsorption of molecules would complete the conducted PAX experiment [38]. But what is considered to be more interesting at the moment is the investigation of the interaction of atomic hydrogen with this corrugated single layer graphene systems. For freestanding graphene theoretical calculations propose the existence of a stable fully hydrogenated graphene sheet called *graphane* [132]. Experimental evidence for the reversible hydrogenation of graphene to graphane has been adduced only recently [133]. Recent calculations predict a much lower stability of fully hydrogenated *h*-BN compared to *g* [134]. With this in mind one question to answer would be: Does the exposure of *g*/Ru(0001) or *g*/Rh(111) to atomic hydrogen lead to intercalation similar to the case of *h*-BN/Rh(111) (Sec. 3.2)? Or will the binding of H towards graphene be stronger? For both cases the influence on the electronic structure of the graphene layer will be interesting to observe. In a removed surface texture scenario a band structure similar to that of freestanding graphene is to be expected as it had been observed for *g*/Ni(111) after intercalation of 1 ML of Au [135].

For the case of the *h*-BN nanomesh a hydrogen intercalated sample is certainly also interesting for SXRD. The stability of the intercalated phase against hard x-rays would first have to be tested. But an *in situ* surface texture switching monitored by SXRD could maybe explain the differences for the formation mechanism of the *h*-BN nanomesh as it has been proposed by high temperature SXRD measurements for Rh(111) [31] and an extrapolation of room temperature SXRD measurements for Ru(0001) [63].

Appendix A

Projections

In angle-resolved photoelectron spectroscopy (ARPES) two projections of the hemisphere are widely used:
For the case of XPD the intensity distribution patterns are usually displayed in *stereographic projection* (Fig. A.1).
In angle-resolved ultraviolet photoelectron spectroscopy (ARUPS) the photoemission intensities are usually plotted versus the parallel momentum

$$\begin{aligned} K_{\parallel}(\mathring{A}^{-1}) = p_{\parallel}/\hbar &= \sin\vartheta\sqrt{2mE_{kin}/\hbar^2} \\ &= 0.5123\,\mathring{A}^{-1}\sin\vartheta\sqrt{E_{kin}(\mathrm{eV})} \\ &= 0.5123\,\mathring{A}^{-1}\sin\vartheta\sqrt{\left(h\nu - |E_B| - \phi\right)(\mathrm{eV})}. \end{aligned}$$

Due to the proportionality to $\sin\vartheta$ this represents a *parallel projection*.
So a parallel projection in ARUPS is directly related to a measurable quantity – the wave vector of the initial state electron perpendicular to the surface normal while a stereographic projection leads to a polar coordinate r which is more easy to interpret.

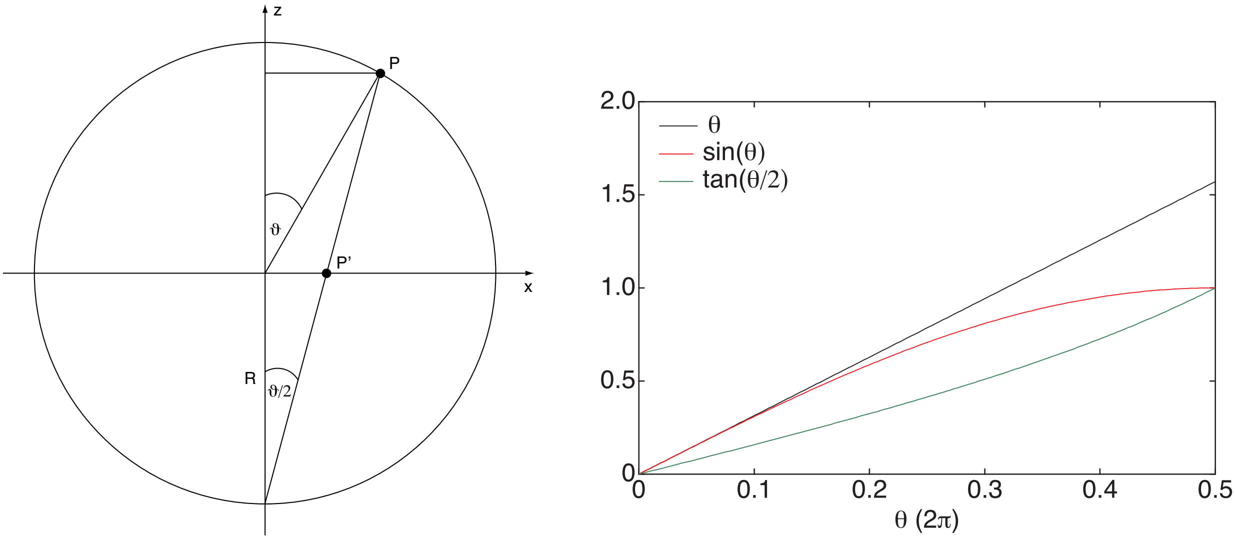

(a) (b)

Figure A.1: a) *Stereographic projection* maps a point P on the upper hemisphere with spherical coordinates ϑ and φ onto a point P' in the x-y plane with polar coordinates $r = \tan\frac{\vartheta}{2}$ and φ. In a *parallel projection* the polar coordinates are given by $r = \sin\vartheta$ and φ.

b) Parallel projections (red curve) are almost linear in θ for small polar angles while stereographic projections (green curve) provide a more constant $\Delta\theta$ over the experimentally accessible range from $0 - \pi/2$.

Appendix B

Nanomesh preparation

In order to prepare a high quality nanomesh it is advantageous to use a single crystal of Rh(111) or Ru(0001) which is well degassed (low carbon contaminations in the bulk) and exhibits large terraces ($\gtrsim$ 500 nm). For the last requirement annealing to high temperatures is crucial ($\approx$ 1400 K, difficult to reach in ESCA). Switch on the quadrupole mass spectrometer and degas both filaments with a 15 min ramp, a maximum emission current of $I_e = 10\,\mathrm{mA}$ and a filament protection current of $I_{fil,prot} = 3.5\,\mathrm{A}$ (after operating each at an emission current of $I_e = 2\,\mathrm{mA}$ for at least 5 min). Switch the filaments back to an emission current of $I_e = 0.8\,\mathrm{mA}$.

Depending on the history of the crystal perform a first Ar^+ sputter cycle of 30 min at a discharge potential of 1 kV if you had been working with e.g. metal clusters on the crystal before, 0.8 kV if you had been using molecules or just want to remove a previous nanomesh. If you encounter difficulties in cleaning the crystal the discharge potential may be increased to $1.5-2$ kV. Do not forget to switch of the secondary electron multiplier (SEM) of the mass spectrometer during high pressures in the chamber ($p > 1.0 \cdot 10^{-5}$ mbar, i.e. during sputtering). After the sputter cycle anneal the crystal to about 970 K and expose it to about $10-15$ L of O_2 ($p_{PC,O_2} \approx 1 \cdot 10^{-8} - 2 \cdot 10^{-8}$ mbar). Follow the oxygen exposure by a flash of the crystal to $1070-1120$ K. Hold the temperature high for about 2 min. If you monitor the oxygen, the CO and the CO_2 signals with the mass spectrometer during O_2 exposure as well as during the flash you can adopt the afore mentioned times if necessary. When the CO and the CO_2 signals start to drop during the O_2 exposure this indicates that all carbon on the crystal surface has been burned and the exposure time may be reduced. During the high temperature flash an increase of the oxygen signal can be observed verifying the desorption of oxygen which had been bound to the crystal surface (on Rh(111) and on Ru(0001) several ordered phases of adsorbed oxygen can exist [136, 137]). If you in addition have a look at the Ar signal you will find it to increase during the flash. This Ar is coming from the Ar bubbles in the crystal which are created during room temperature sputtering and indicates a healing of the crystal surface. Switch off the heating of the crystal and wait until its temperature dropped below $\approx$ 400 K before you proceed with the next sputtering cycle.

In the second cycle sputter with 0.8 kV for 20 min followed by an exposure to about 5 L of O_2

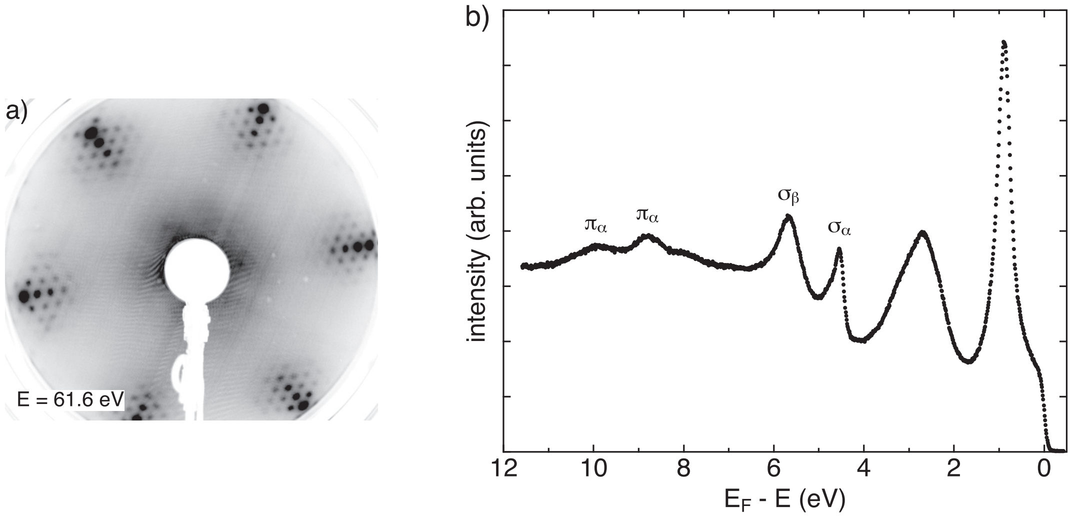

Figure B.1: Indications for a good nanomesh preparation. a) LEED image taken at a primary electron kinetic energy of 61.6 eV showing the sharp superstructure spots which surround the Rh(111) principal spots. b) He I_α normal emission UPS where a sharp σ_α band and the band splitting of the σ and the π band can be observed.

and the flash. After this cycle clean the borazine using a freeze–pump–thaw procedure: Switch off the Peltier cooler and carefully remove it from the glass vial. Pump the volume between the UHV leak valve and the borazine storage volume with the fast entry airlock (FEAL) turbopump. Freeze the liquid borazine with liquid nitrogen (LN_2): Slowly move the LN_2 container upwards until you start to cool the glass vial, remain at this position for a few seconds to allow the liquid borazine to freeze. Then dip roughly two third of the vial into the LN_2 and wait about 15 s before you open the 90° valve above the vial. Pump for a few seconds and then remove the LN_2 quickly. Now within about 5 s close the valve to the FEAL and then allow the borazine to expand into the volume between the UHV leak valve and the valve towards the FEAL. Protect it from UV light by putting some Al foil around the vial.

In the third cycle sputter at 0.5 kV for 15 min and only dose a small amount of O_2 ($\approx 1-2\,\mathrm{L}$). Flash the crystal and afterwards go back to a temperature of 1030 K. At that temperature expose the crystal to 55 L of borazine ($p_{DC} = 4 \cdot 10^{-7}\,\mathrm{mbar}, t = 3\,\mathrm{min}$), keep it another minute at this temperature and then slowly switch off the filament. During cool down you can already start to ramp up the filament of the LEED.

When the temperature reached about 400 K transfer the crystal to the LEED and take a picture. If you observe nice and sharp superstructure spots similar to the ones in Fig. B.1 a), you can freeze back the borazine. For that slowly cool the vial again with LN_2. In order to collect as much gaseous borazine as possible back to the storage container, cool the whole vial for about 30 s. Now close the 90° valve and remove the LN_2. Wait a few minutes before you mount and switch on the Peltier cooler again. Afterwards do UPS and check if you see the σ and π band splitting and especially a sharp σ_α band in normal emission [Fig. B.1 b)]. Do not forget to measure the work function of the *h*-BN/Rh(111) nanomesh ($\phi = 4.1\,\mathrm{eV}$).

Now you have a nice preparation at hand and may start your further experiments.

Appendix C

Nanomesh growth without sputtering

Achieving *h*-BN/Rh(111) nanomesh growth on 4 in Si wavers is an important step on the way to a more efficient nanomesh production. As this it is defined as one of the goals of a new SINERGIA project[1] funded by the Swiss National Science Foundation which started in 2009. A big step into that direction has already been realized by the growth of epitaxial Rh(111) metal films of 150 nm thickness on a 4 in Si wafer including a YSZ buffer layer of about 50 nm [125]. Since it is difficult and expensive to homogeneously sputter the area of a 4 in wafer even in a dedicated UHV setup we tried to grow the *h*-BN/Rh(111) nanomesh in our ESCA system on such 150 nm Rh(111) film samples that were cut out of a 4 in wafer without a single Ar^+ sputter cycle.

Figure C.1 shows a series of Mg K_α excited C1s core level x-ray photoelectron spectra. After introducing the as received film sample into the UHV system, degassing it at about 780 K for several hours and finally flashing it once to $T = 1035$ K the amount of carbon which corresponds to about 2.3 ML was found on the surface. Exposing the Rh(111) film sample to 50 L O_2 at $T = 905$ K and subsequently flashing it to $T = 1050$ K for a few minutes reduced the amount of carbon on the surface to an equivalent of about 1.8 ML. A second 50 L O_2 exposure at a slightly higher temperature of $T = 980$ K followed by flashing to $T = 1070$ K drastically reduced the carbon contaminations on the Rh(111) surface – the amount of only about 0.4 ML carbon was found after this step. In LEED a very weak superstructure, which could be a sign of partial graphene formation on the surface of the Rh(111) film sample, is visible after this treatment [Fig. C.2 a)]. In a third preparation step the sample was exposed to 25 L O_2 at $T = 970$ K followed by a flash to $T = 1070$ K concluding with a 80 L borazine exposure at $T = 1030$ K. After this step no carbon contamination could be found on the surface. In addition a distinct superstructure which suggests successful nanomesh formation arises in LEED [Fig. C.2 b)]. Normal emission UPS which is compared to a standard nanomesh preparation in Figure C.3 clearly verifies the formation of a *h*-BN/Rh(111) nanomesh by the above described procedure.

---

[1] `http://www.snf.ch/E/funding/projects/sinergia/Pages/default.aspx`

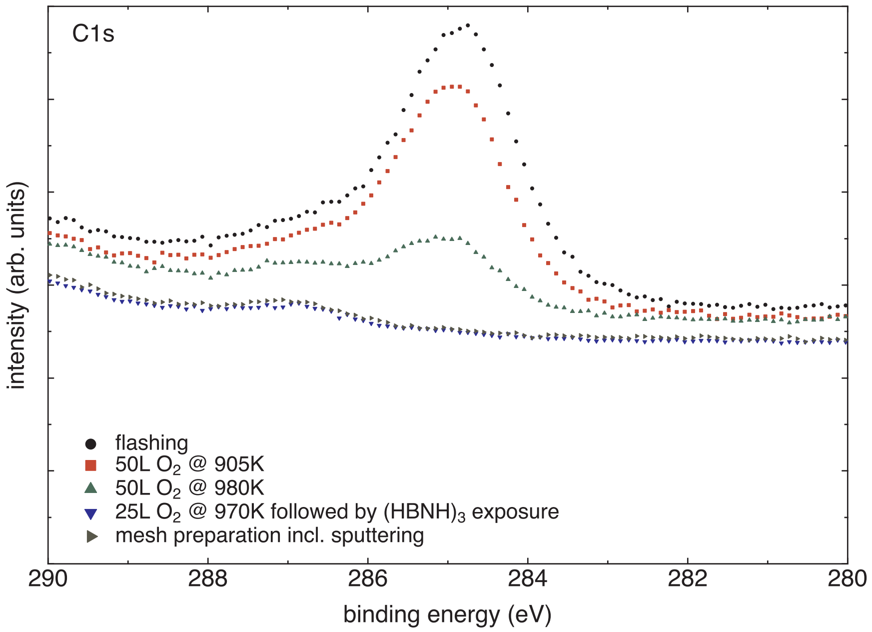

Figure C.1: Mg K_α excited C1s corelevel XPS on the same Rh(111) film sample after flashing to 1035 K (black filled circles), after dosing 50 L O_2 at $T = 905$ K (red filled squares), after additional dosing of 50 L O_2 at $T = 980$ K (green filled upright triangles) and after additional O_2 exposure of 50 L at $T = 970$ K followed by a borazine exposure of L at $T =$ K (blue filled reversed triangles).

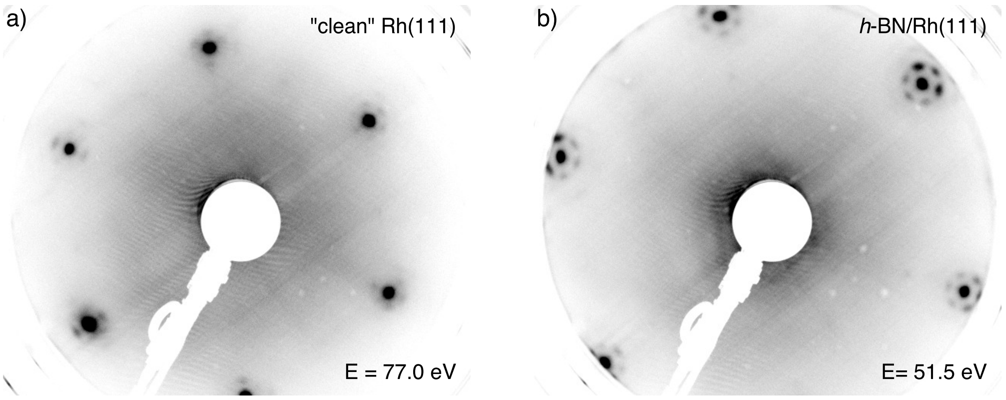

Figure C.2: LEED images of the unsputtered Rh(111) film sample a) before and b) after borazine exposure. In a) a weak superstructure is observed most probably due to partial graphene coverage of the sample. In b) the nanomesh superstructure can clearly be seen.

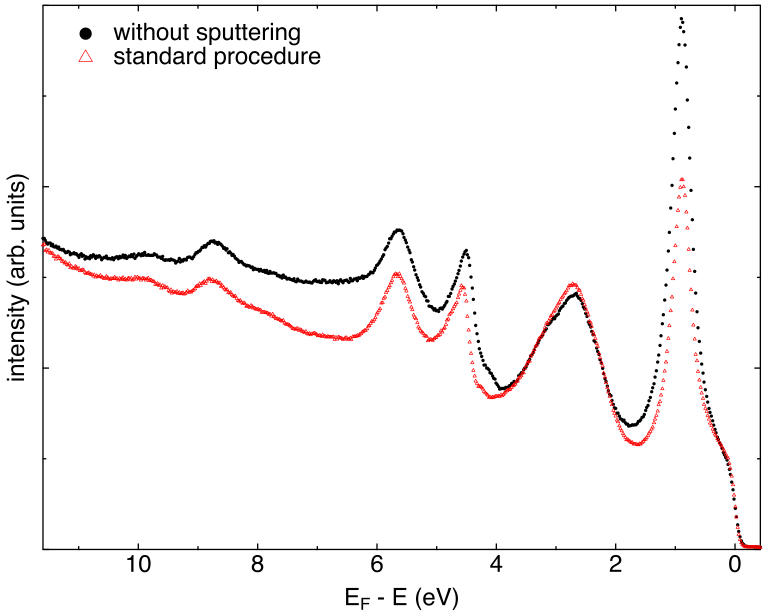

Figure C.3: He I_α excited normal emission UPS: Comparison of a *h*-BN/Rh(111) preparation with (red open triangles) and without (black filled circles) sputtering.

Figure C.4

Appendix D

Carbonyl handling

Tetracobalt dodecacarbonyl [$Co_4(CO)_{12}$] is a dark grey/black crystalline solid at room temperature which is usually sold in the form of small crystallites with sizes similar to the ones of Kish graphite (e.g. by Strem Chemicals Inc.). It melts with decomposition at 330 K and sublimes with decomposition at 360 K and a vapor pressure of about 0.1 mbar. Avoid exposure to $Co_4(CO)_{12}$ because its decomposition products may be toxic (carbon monoxide) and carcinogen (cobalt). Store in dark, cool and dry area (fridge) using tightly sealed container.

For the use as an evaporation source in UHV choose a flange equipped with a gate valve and direct line of sight to the sample. Reduce your flange size to CF16 but only keep an aperture of about $1-2$ mm open. Try to maximize the length of the aperture to achieve a good focus on the sample due to the beaming effect of molecular flow. Put a small amount of $Co_4(CO)_{12}$ into a standard borazine cooler (available as CFH-LIQCOOLER at Ferrovac GmbH) and mount it to the evaporation port. Pump the whole volume including the carbonyl reservoir with a turbo pump. With the carbonyl reservoir separated and the Peltier cooler of the CFH-LIQCOOLER running mildly bake the new volume. After the bake open the valve to the carbonyl reservoir and increase its temperature to about $310-320$ K by reversing the polarity of the Peltier cooler's power supply. Wait about 30 min before you carefully open the gate valve to your UHV chamber. If the pressure in the UHV chamber stays below a reasonable limit close the valve between the external turbo pump and the carbonyl evaporator – you are exposing your sample to $Co_4(CO)_{12}$.

MATERIAL SAFETY DATA SHEET

Manufacturer:
Strem Chemicals, Inc.
7 Mulliken Way
Newburyport, MA 01950-4098 U.S.A.
www.strem.com

Strem Customer Service	(978) 499-1600
CHEMTREC (Emergency Only)	(800) 424-9300
Poison Center	(800) 562-8236

SECTION 1: Product Identification

Chemical Name:	Tetracobalt dodecacarbonyl, min. 98%
Product Number:	27-1950
CAS Registry Number:	17786-31-1
Formula:	Co4(CO)12
EINECS Number:	none
Chemical Family:	metal carbonyl complexes
Synonym:	Dodecacarbonyl tetracobalt

SECTION 2: Composition and Information on Ingredients

Ingredient	CAS Number	Percent	ACGIH (TWA)	OSHA (PEL)
Title Compound	17786-31-1	100	0.02mg/m3	no data

SECTION 3: Hazards Identification

Emergency Overview:	Vapor may be harmful. Inhalation may lead to headaches and dizziness. Limited evidence of a carcinogenic effect.
Primary Routes of Exposure:	Ingestion, inhalation
Eye Contact:	May cause mild irritation to the eyes.
Skin Contact:	May cause mild irritation to the skin.
Inhalation:	Inhalation could lead to dizziness and headache.
Ingestion:	No information available on the effects from ingestion.
Acute Health Effects:	Inhalation could lead to headache and dizziness.
Chronic Health Effects:	Cobalt is a suspected carcinogen of the lungs and connective tissue.
NTP:	No
IARC:	Yes
OSHA:	No

SECTION 4: First Aid Measures

Eye Exposure:	Immediately flush the eyes with copious amounts of water for at least 15 minutes. A victim will need assistance in keeping their eye lids open. Get immediate medical attention.
Skin Exposure:	Wash the affected area immediately with water. Remove contaminated clothing if necessary. Seek medical assistance if irritation persists.
Inhalation:	Remove victim to fresh air immediately. Keep the victim lying down and warm. Give oxygen as soon as possible. If shock occurs, respond with appropriate first aid. Transport the victim to a hospital.
Ingestion:	Seek medical attention immediately. Keep the victim calm. Give water to dilute the toxin (only if conscious). Induce vomiting only if directed by medical personnel.

SECTION 5: Fire Fighting Measures

Flash Point:	not applicable
Autoignition Temperature:	no data
Explosion Limits:	no data
Extinguishing Medium:	carbon dioxide, dry chemical or foam
Special Fire Fighting Procedures:	If involved in a fire, fire fighters should be equipped with a NIOSH-approved positive pressure self-contained breathing apparatus.
Hazardous Combustion and Decomposion Products:	carbon monoxide, carbon dioxide, and cobalt oxide dust.
Unusual Fire or Explosion Hazards:	Flammable solid. No unusual fire or explosion hazards.

SECTION 6: Accidental Release Measures

Spill and Leak Procedures:	Small quantities can be mixed with sodium carbonate or vermiculite and swept up.

SECTION 7: Handling and Storage

Handling and Storage:	Store in a cool, dry, well-ventilated area away from heat and direct sunlight. Keep containers tightly sealed.

SECTION 8: Exposure Controls and Personal Protection

Eye Protection:	Always wear approved safety glasses when handling chemical substances.
Skin Protection:	Wear protective clothing and gloves. Consult with glove manufacturer to determine the proper type of glove.
Ventilation:	This product should be handled in an efficient fume hood.
Respirator:	If ventilation is not available a respirator should be worn. The use of respirators requires a Respirator Protection Program to be in compliance 29 CFR 1910.134.
Additional Protection:	No additional protection required.

SECTION 9: Physical and Chemical Properties

Color and Form:	black xtl.
Molecular Weight:	571.85
Melting Point:	60°C dec.
Boiling Point:	no data
Vapor Pressure:	no data
Specific Gravity:	2.09
Odor:	none
Solubility in Water:	Insoluble

SECTION 10: Stability and Reactivity

Stability:	air sensitive, (store cold)
Hazardous Polymerization:	no hazardous polymerization
Conditions to Avoid:	prolonged exposure to air.
Incompatibility:	Oxidizing agents and halogens
Decomposition Products:	carbon dioxide, carbon monoxide, cobalt oxide

SECTION 11: Toxicological Information

RTECS Data:	No specific information available on this product.
Carcinogenic Effects:	No data available
Mutagenic Effects:	No data available
Tetratogenic Effects:	No data available

SECTION 12: Ecological Information

Ecological Information:	No information available.

SECTION 13: Disposal Considerations

Disposal:	Dispose of this material according to local, state and federal regulations.

SECTION 14: Transportation

Shipping Name (CFR):	Flammable solids, inorganic, N.O.S.
Hazard Class (CFR):	4.1
Additional Hazard Class (CFR):	NA
Packaging Group (CFR):	II
UN ID Number (CFR):	UN# 3178
Shipping Name (IATA):	Flammable solid, inorganic, N.O.S.
Hazard Class (IATA):	4.1
Additional Hazard Class (IATA):	NA
Packaging Group (IATA):	II
UN ID Number (IATA):	UN# 3178

SECTION 15: Regulatory Information

TSCA:	Not listed in the TSCA inventory.
SARA (Title 313):	Title compound: See Category Code N096 and N511 for reporting.
Second Ingredient:	none
Third Ingredient:	none

SECTION 16: Other Information

Disclaimer:	The information herein is believed to be accurate and reliable as of the date compiled. However, Strem Chemicals, Inc. makes no representation, warranty, or guarantee of any kind with respect to the information contained in this document or any use of the product based on this information.
Preparation Date:	8/07/2000
Revision Date:	1/30/2004

Corporate Headquarters:
7 Mulliken Way
Newburyport, MA 01950-4098
U.S.A.
Tel: (978) 499-1600
Fax: (978) 465-3104

Strem Chemicals, Inc.
www.strem.com

European Headquarters:
15, rue de l'Atome
67800 BISCHHEIM (France)
Tel: (33) 03 88 62 52 60
Fax: (33) 03 88 62 26 81

Bibliography

[1] P. M. Echenique, R. Berndt, E. V. Chulkov, T. Fauster, A. Goldmann, and U. Höfer, *Decay of electronic excitations at metal surfaces*, Surface Science Reports **52**, 219 (2004), DOI: 10.1016/j.surfrep.2004.02.002.

[2] P. Avouris, I.-W. Lyo, and F. Bozso, *Atom-resolved surface chemistry: The early steps of Si(111)-7 x 7 oxidation*, Journal of Vacuum Science & Technology B **9**, 424 (1991), DOI: 10.1116/1.585584.

[3] H. Over and M. Muhler, *Catalytic CO oxidation over ruthenium–bridging the pressure gap*, Progress in Surface Science **72**, 3 (2003), DOI: 10.1016/S0079-6816(03)00011-X.

[4] J. V. Barth, G. Costantini, and K. Kern, *Engineering atomic and molecular nanostructures at surfaces*, Nature **437**, 671 (2005), DOI: 10.1038/nature04166.

[5] A. H. C. Neto, F. Guinea, N. M. R. Peres, K. S. Novoselov, and A. K. Geim, *The electronic properties of graphene*, Reviews of Modern Physics **81**, 109 (2009), DOI: 10.1103/RevModPhys.81.109.

[6] P. Trucano and R. Chen, *Structure of graphite by neutron diffraction*, Nature **258**, 136 (1975), DOI: 10.1038/258136a0.

[7] R. S. Pease, *An X-ray study of boron nitride*, Acta Crystallographica **5**, 356 (1952), DOI: 10.1107/S0365110X52001064.

[8] P. R. Wallace, *The Band Theory of Graphite*, Physical Review **71**, 622 (1947), DOI: 10.1103/PhysRev.71.622.

[9] S. Y. Zhou, G. H. Gweon, J. Graf, A. V. Fedorov, C. D. Spataru, R. D. Diehl, Y. Kopelevich, D. H. Lee, S. G. Louie, and A. Lanzara, *First direct observation of Dirac fermions in graphite*, Nature Physics **2**, 595 (2006), DOI: 10.1038/nphys393.

[10] A. Catellani, M. Posternak, A. Baldereschi, and A. J. Freeman, *Bulk and surface electronic structure of hexagonal boron nitride*, Physical Review B **36**, 6105 (1987), DOI: 10.1103/PhysRevB.36.6105.

[11] A. Nagashima, N. Tejima, Y. Gamou, T. Kawai, and C. Oshima, *Electronic dispersion relations of monolayer hexagonal boron nitride formed on the Ni(111) surface*, Physical Review B **51**, 4606 (1995), DOI: 10.1103/PhysRevB.51.4606.

[12] G. W. Semenoff, *Condensed-Matter Simulation of a Three-Dimensional Anomaly*, Physical Review Letters **53**, 2449 (1984), DOI: 10.1103/PhysRevLett.53.2449.

[13] K. S. Novoselov, A. K. Geim, S. V. Morozov, D. Jiang, Y. Zhang, S. V. Dubonos, I. V. Grigorieva, and A. A. Firsov, *Electric Field Effect in Atomically Thin Carbon Films*, Science **306**, 666 (2004), DOI: 10.1126/science.1102896.

[14] F. Schedin, A. K. Geim, S. V. Morozov, E. W. Hill, P. Blake, M. I. Katsnelson, and K. S. Novoselov, *Detection of individual gas molecules adsorbed on graphene*, Nature Materials **6**, 652 (2007), DOI: 10.1038/nmat1967.

[15] O. Leenaerts, B. Partoens, and F. M. Peeters, *Graphene: A perfect nanoballoon*, Applied Physics Letters **93**, 193107 (2008), DOI: 10.1063/1.3021413.

[16] P. Neugebauer, M. Orlita, C. Faugeras, A. L. Barra, and M. Potemski, *How Perfect Can Graphene Be?*, Physical Review Letters **103**, 136403 (2009), DOI: 10.1103/PhysRevLett.103.136403.

[17] S. D. Robertson, *Graphite Formation from Low Temperature Pyrolysis of Methane over some Transition Metal Surfaces*, Nature **221**, 1044 (1969), DOI: 10.1038/2211044a0.

[18] M. T. Paffett, R. J. Simonson, P. Papin, and R. T. Paine, *Borazine adsorption and decomposition at Pt(111) and Ru(001) surfaces*, Surface Science **232**, 286 (1990), DOI: 10.1016/0039-6028(90)90121-N.

[19] C. Oshima and A. Nagashima, *Ultra-thin epitaxial films of graphite and hexagonal boron nitride on solid surfaces*, Journal Of Physics - Condensed Matter **9**, 1 (1997).

[20] M. Corso, W. Auwärter, M. Muntwiler, A. Tamai, T. Greber, and J. Osterwalder, *Boron Nitride Nanomesh*, Science **303**, 217 (2004), DOI: 10.1126/science.1091979.

[21] A. Goriachko, Y. B. He, M. Knapp, H. Over, M. Corso, T. Brugger, S. Berner, J. Osterwalder, and T. Greber, *Self-Assembly of a Hexagonal Boron Nitride Nanomesh on Ru(0001)*, Langmuir **23**, 2928 (2007), DOI: 10.1021/la062990t.

[22] Y. Pan, D.-X. Shi, and H.-J. Gao, *Formation of graphene on Ru(0001) surface*, Chinese Physics **16**, 3151 (2007), DOI: 10.1088/1009-1963/16/11/001.

[23] S. Marchini, S. Günther, and J. Wintterlin, *Scanning tunneling microscopy of graphene on Ru(0001)*, Physical Review B **76**, 075429 (2007), DOI: 10.1103/PhysRevB.76.075429.

[24] A. B. Preobrajenski, M. L. Ng, A. S. Vinogradov, and N. Mårtensson, *Controlling graphene corrugation on lattice-mismatched substrates*, Physical Review B **78**, 073401 (2008), DOI: 10.1103/PhysRevB.78.073401.

[25] F. Müller, H. Sachdev, S. Hüfner, A. J. Pollard, E. W. Perkins, J. C. Russell, P. H. Beton, S. Gsell, M. Fischer, M. Schreck, et al., *How Does Graphene Grow? Easy Access to Well-Ordered Graphene Films*, Small **5**, 2291 (2009), DOI: 10.1002/smll.200900158.

[26] S. Berner, M. Corso, R. Widmer, O. Groening, R. Laskowski, P. Blaha, K. Schwarz, A. Goriachko, H. Over, S. Gsell, et al., *Boron Nitride Nanomesh: Functionality from a Corrugated Monolayer*, Angewandte Chemie-International Edition **46**, 5115 (2007), DOI: 10.1002/anie.200700234.

[27] H. Dil, J. Lobo-Checa, R. Laskowski, P. Blaha, S. Berner, J. Osterwalder, and T. Greber, *Surface Trapping of Atoms and Molecules with Dipole Rings*, Science **319**, 1824 (2008), DOI: 10.1126/science.1154179.

[28] R. Laskowski, P. Blaha, T. Gallauner, and K. Schwarz, *Single-layer model of the hexagonal boron nitride nanomesh on the Rh(111) surface*, Physical Review Letters **98**, 106802 (2007), DOI: 10.1103/PhysRevLett.98.106802.

[29] H. P. Singh, *Determination of thermal expansion of germanium, rhodium and iridium by X-rays*, Acta Crystallographica Section A - Crystal Physics Diffraction Theoretical and General Crystallography **A24**, 469 (1968), DOI: 10.1107/S056773946800094X.

[30] O. Bunk, M. Corso, D. Martoccia, R. Herger, P. R. Willmott, B. D. Patterson, J. Osterwalder, J. F. van der Veen, and T. Greber, *Surface X-ray diffraction study of boron-nitride nanomesh in air*, Surface Science **601**, L7 (2007), DOI: 10.1016/j.susc.2006.11.018.

[31] D. Martoccia, S. A. Pauli, T. Brugger, T. Greber, B. D. Patterson, and P. R. Willmott, *h-BN on Rh(111): Persistence of a commensurate 13-on-12 superstructure up to high temperatures*, Surface Science **604**, L9 (2010), DOI: 10.1016/j.susc.2009.12.016.

[32] T. Greber, W. Auwärter, M. Hoesch, G. Grad, P. Blaha, and J. Osterwalder, *The Fermi surface in a magnetic metal-insulator interface*, Surface Review and Letters **9**, 1243 (2002), DOI: 10.1142/S0218625X02001884.

[33] R. Laskowski, P. Blaha, and K. Schwarz, *Bonding of hexagonal BN to transition metal surfaces: An ab initio density-functional theory study*, Physical Review B **78**, 045409 (2008), DOI: 10.1103/PhysRevB.78.045409.

[34] A. Nagashima, N. Tejima, Y. Gamou, T. Kawai, and C. Oshima, *Electronic Structure of Monolayer Hexagonal Boron Nitride Physisorbed on Metal Surfaces*, Physical Review Letters **75**, 3918 (1995), DOI: 10.1103/PhysRevLett.75.3918.

[35] R. Laskowski and P. Blaha, *Unraveling the structure of the h-BN/Rh(111) nanomesh with ab initio calculations*, Journal of Physics-Condensed Matter **20**, 064207 (2008), DOI: 10.1088/0953-8984/20/6/064207.

[36] R. Widmer, S. Berner, O. Gröning, T. Brugger, J. Osterwalder, and T. Greber, *Electrolytic in situ STM investigation of h-BN-Nanomesh*, Electrochemistry Communications **9**, 2484 (2007), DOI: 10.1016/j.elecom.2007.07.019.

[37] V. A. Finkel, M. I. Palatnik, and G. P. Kovtun, *Thermal expansion of Ru, Os and Re at 77-300K x-ray determination*, Fizika Metallov Metallovedenie **32**, 212 (1971).

[38] T. Brugger, S. Günther, B. Wang, J. H. Dil, M.-L. Bocquet, J. Osterwalder, J. Wintterlin, and T. Greber, *Comparison of electronic structure and template function of single-layer graphene and a hexagonal boron nitride nanomesh on Ru(0001)*, Physical Review B **79**, 045407 (2009), DOI: 10.1103/PhysRevB.79.045407.

[39] A. Goriachko, Y. B. He, and H. Over, *Complex Growth of NanoAu on BN Nanomeshes Supported by Ru(0001)*, The Journal of Physical Chemistry C **112**, 8147 (2008), DOI: 10.1021/jp7119608.

[40] G. Binnig, H. Rohrer, C. Gerber, and E. Weibel, *Surface Studies by Scanning Tunneling Microscopy*, Physical Review Letters **49**, 57 (1982), DOI: 10.1103/PhysRevLett.49.57.

[41] J. Bardeen, *Tunnelling from a Many-Particle Point of View*, Physical Review Letters **6**, 57 (1961), DOI: 10.1103/PhysRevLett.6.57.

[42] J. Tersoff and D. R. Hamann, *Theory and Application for the Scanning Tunneling Microscope*, Physical Review Letters **50**, 1998 (1983), DOI: 10.1103/PhysRevLett.50.1998.
J. Tersoff and D. R. Hamann, *Theory of the scanning tunneling microscope*, Physical Review B **31**, 805 (1985), DOI: 10.1103/PhysRevB.31.805.

[43] M. F. Crommie, C. P. Lutz, and D. M. Eigler, *Confinement of Electrons to Quantum Corrals on a Metal Surface*, Science **262**, 218 (1993), DOI: 10.1126/science.262.5131.218.

[44] D. A. Bonnell, ed., *Scanning Tunneling Microscopy and Spectroscopy: Theory, Techniques and Applications* (VCH Publishers, Inc., 220 East 23rd Street, New York, NY 10010, 1993).

[45] H. Hertz, *Über einen Einfluss des ultravioletten Lichtes auf die elektrische Entladung*, Annalen der Physik und Chemie **267**, 983 (1887), DOI: 10.1002/andp.18872670827.

[46] A. Einstein, *über einen die Erzeugung und Verwandlung des Lichtes betreffenden heuristischen Gesichtspunkt*, Annalen der Physik **322**, 132 (1905), DOI: 10.1002/andp.19053220607.

[47] S. Hüfner, *Photoelectron spectroscopy: Principles and Applications*, vol. 82 of *Springer Series in Solid-State Sciences* (Springer-Verlag, 1995).

[48] M. P. Seah and W. A. Dench, *Quantitative electron spectroscopy of surfaces: A standard data base for electron inelastic mean free paths in solids*, Surface and Interface Analysis **1**, 2 (1979), DOI: 10.1002/sia.740010103.

[49] J. Osterwalder, T. Greber, E. Wetli, J. Wider, and H. Neff, *Full hemispherical photoelectron diffraction and Fermi surface mapping*, Progress in Surface Science **64**, 65 (2000), DOI: 10.1016/S0079-6816(00)00012-5.

[50] H. C. Poon and S. Y. Tong, *Focusing and diffraction effects in angle-resolved x-ray photoelectron spectroscopy*, Physical Review B **30**, 6211 (1984), DOI: 10.1103/PhysRevB.30.6211.

[51] C. N. Berglund and W. E. Spicer, *Photoemission Studies of Copper and Silver: Theory*, Physical Review **136**, A1030 (1964), DOI: 10.1103/PhysRev.136.A1030.

[52] J. Küppers, K. Wandelt, and G. Ertl, *Influence of the Local Surface Structure on the 5p Photoemission of Adsorbed Xenon*, Physical Review Letters **43**, 928 (1979), DOI: 10.1103/PhysRevLett.43.928.

[53] K. Wandelt, *Surface characterization by photoemission of adsorbed xenon (PAX)*, Journal of Vacuum Science & Technology A: Vacuum, Surfaces, and Films **2**, 802 (1984), DOI: 10.1116/1.572509.

[54] G. Ertl and J. Küppers, *Low Energy Electrons and Surface Chemistry* (VCH Verlagsgesellschaft mbH, 1985), 2nd ed.

[55] M. Henzler and W. Göpel, *Oberflächenphysik des Festkörpers*, Teubner-Studienbücher: Physik (Teubner, Stuttgart, 1994), 2nd ed.

[56] A. L. Vázquez de Parga, F. Calleja, B. Borca, M. C. G. Passeggi, J. J. Hinarejos, F. Guinea, and R. Miranda, *Periodically rippled graphene: Growth and spatially resolved electronic structure*, Physical Review Letters **100**, 056807 (2008), DOI: 10.1103/PhysRevLett.100.056807.

[57] Y. Gamou, M. Terai, A. Nagashima, and C. Oshima, *Atomic Structural Analysis of a Monolayer Epitaxial Film of Hexagonal Boron Nitride/Ni(111) studied by LEED Intensity Analysis*, Science reports of the Research Institutes Tohoku University Series A, Physics, chemistry and metallurgy **44**, 211 (1997).

[58] M. Morscher, M. Corso, T. Greber, and J. Osterwalder, *Formation of single layer h-BN on Pd(111)*, Surface Science **600**, 3280 (2006), DOI: 10.1016/j.susc.2006.06.016.

[59] T. A. Land, T. Michely, R. J. Behm, J. C. Hemminger, and G. Comsa, *STM investigation of single layer graphite structures produced on Pt(111) by hydrocarbon decomposition*, Surface Science **264**, 261 (1992), DOI: 10.1016/0039-6028(92)90183-7.

[60] Y. Gamo, A. Nagashima, M. Wakabayashi, M. Terai, and C. Oshima, *Atomic structure of monolayer graphite formed on Ni(111)*, Surface Science **374**, 61 (1997), DOI: 10.1016/S0039-6028(96)00785-6.

[61] A. T. N'Diaye, S. Bleikamp, P. J. Feibelman, and T. Michely, *Two-Dimensional Ir Cluster Lattice on a Graphene Moiré on Ir(111)*, Physical Review Letters **97**, 215501 (2006), DOI: 10.1103/PhysRevLett.97.215501.

[62] D. Martoccia, P. R. Willmott, T. Brugger, M. Björck, S. Günther, C. M. Schlepütz, A. Cervellino, S. A. Pauli, B. D. Patterson, S. Marchini, et al., *Graphene on Ru(0001): A 25 x 25 Supercell*, Physical Review Letters **101**, 126102 (2008), DOI: 10.1103/PhysRevLett.101.126102.

[63] D. Martoccia, T. Brugger, M. Björck, C. M. Schlepütz, S. A. Pauli, T. Greber, B. D. Patterson, and P. R. Willmott, *h-BN/Ru(0001) nanomesh: A 14-on-13 superstructure with 3.5 nm periodicity*, Surface Science **604**, L16 (2010), DOI: 10.1016/j.susc.2010.01.003.

[64] B. Wang, M. L. Bocquet, S. Marchini, S. Günther, and J. Wintterlin, *Chemical origin of a graphene moire overlayer on Ru(0001)*, Physical Chemistry Chemical Physics **10**, 3530 (2008), DOI: 10.1039/b801785a.

[65] B. Wang, M.-L. Bocquet, S. Günther, and J. Wintterlin, *Comment on 'Periodically Rippled Graphene: Growth and Spatially Resolved Electronic Structure'*, Physical Review Letters **101**, 099703 (2008), DOI: 10.1103/PhysRevLett.101.099703.

[66] A. L. Vázquez de Parga, F. Calleja, B. Borca, M. C. G. Passeggi, Jr., J. J. Hinarejos, F. Guinea, and R. Miranda, *Vázquez de Parga et al. Reply:*, Physical Review Letters **101**, 099704 (2008), DOI: 10.1103/PhysRevLett.101.099704.

[67] D. Martoccia, M. Bjoerck, C. Schlepuetz, T. Brugger, S. Pauli, B. Patterson, T. Greber, and P. Willmott, *Graphene on Ru(0001): A corrugated and chiral structure*, 0908.4517v1 (2009), URL: http://arxiv.org/abs/0908.4517.

[68] W. Moritz, B. Wang, M. L. Bocquet, T. Brugger, T. Greber, J. Wintterlin, and S. Günther, *Structure Determination of the Coincidence Phase of Graphene on Ru(0001)*, Physical Review Letters **104**, 1361021 (2010), DOI: 10.1103/PhysRevLett.104.136102.

[69] G. Kresse and D. Joubert, *From ultrasoft pseudopotentials to the projector augmented-wave method*, Physical Review B **59**, 1758 (1999), DOI: 10.1103/PhysRevB.59.1758.

[70] J. P. Perdew, K. Burke, and M. Ernzerhof, *Generalized Gradient Approximation Made Simple*, Physical Review Letters **77**, 3865 (1996), DOI: 10.1103/PhysRevLett.77.3865.

[71] A. Bostwick, T. Ohta, T. Seyller, K. Horn, and E. Rotenberg, *Quasiparticle dynamics in graphene*, Nature Physics **3**, 36 (2007), DOI: 10.1038/nphys477.

[72] A. B. Preobrajenski, M. A. Nesterov, M. L. Ng, A. S. Vinogradov, and N. Mårtensson, *Monolayer h-BN on lattice-mismatched metal surfaces: On the formation of the nanomesh*, Chemical Physics Letters **446**, 119 (2007), DOI: 10.1016/j.cplett.2007.08.028.

[73] G. Kaindl, T. C. Chiang, D. E. Eastman, and F. J. Himpsel, *Distance-Dependent Relaxation Shifts of Photoemission and Auger Energies for Xe on Pd(001)*, Physical Review Letters **45**, 1808 (1980), DOI: 10.1103/PhysRevLett.45.1808.

[74] H. Ulbricht, R. Zacharia, N. Cindir, and T. Hertel, *Thermal desorption of gases and solvents from graphite and carbon nanotube surfaces*, Carbon **44**, 2931 (2006), DOI: 10.1016/j.carbon.2006.05.040.

[75] M. S. Dresselhaus and G. Dresselhaus, *Intercalation compounds of graphite*, Advances in Physics **30**, 139 (1981), DOI: 10.1080/00018738100101367.

[76] J. Zhang, V. Sessi, C. H. Michaelis, I. Brihuega, J. Honolka, K. Kern, R. Skomski, X. Chen, G. Rojas, and A. Enders, *Ordered layers of Co clusters on BN template layers*, Physical Review B **78**, 165430 (2008), DOI: 10.1103/PhysRevB.78.165430.

[77] C. Eibl, G. Lackner, and A. Winkler, *Quantitative characterization of a highly effective atomic hydrogen doser*, Journal of Vacuum Science & Technology A: Vacuum, Surfaces, and Films **16**, 2979 (1998), DOI: 10.1116/1.581449.

[78] G. Lippert, J. Hutter, and M. Parrinello, *A hybrid Gaussian and plane wave density functional scheme*, Molecular Physics **92**, 477 (1997), DOI: 10.1080/002689797709482119.

[79] J. VandeVondele, M. Krack, F. Mohamed, M. Parrinello, T. Chassaing, and J. Hutter, *Quickstep: Fast and accurate density functional calculations using a mixed Gaussian and plane waves approach*, Computer Physics Communications **167**, 103 (2005), DOI: 10.1016/j.cpc.2004.12.014.

[80] *The CP2K developers group.* `http://cp2k.berlios.de/`, (2009), URL: http://cp2k.berlios.de/.

[81] Y. Zhang and W. Yang, *Comment on 'generalized gradient approximation made simple'*, Physical Review Letters **80**, 890 (1998), DOI: 10.1103/PhysRevLett.80.890.

[82] S. Grimme, *Accurate description of van der Waals complexes by density functional theory including empirical corrections*, Journal of Computational Chemistry **25**, 1463 (2004), DOI: 10.1002/jcc.20078.

[83] J. VandeVondele and J. Hutter, *Gaussian basis sets for accurate calculations on molecular systems in gas and condensed phases*, The Journal of Chemical Physics **127**, 114105 (2007), DOI: 10.1063/1.2770708.

[84] S. Goedecker, M. Teter, and J. Hutter, *Separable dual-space Gaussian pseudopotentials*, Physical Review B **54**, 1703 (1996), DOI: 10.1103/PhysRevB.54.1703.

[85] W. Humphrey, A. Dalke, and K. Schulten, *VMD: Visual molecular dynamics*, Journal of Molecular Graphics **14**, 33 (1996), DOI: 10.1016/0263-7855(96)00018-5.

[86] A. B. Preobrajenski, A. S. Vinogradov, M. L. Ng, E. Cavar, R. Westerstrom, A. Mikkelsen, E. Lundgren, and N. Mårtensson, *Influence of chemical interaction at the lattice-mismatched h-BN/Rh(111) and h-BN/Pt(111) interfaces on the overlayer morphology*, Physical Review B **75**, 245412 (2007), DOI: 10.1103/PhysRevB.75.245412.

[87] M. Fukuoka, M. Okada, M. Matsumoto, S. Ogura, K. Fukutani, and T. Kasai, *Location of hydrogen adsorbed on Rh(111) studied by low-energy electron diffraction and nuclear reaction analysis*, Physical Review B **75**, 235434 (2007), DOI: 10.1103/PhysRevB.75.235434.

[88] S. Blundell, *Magnetism in Condensed Matter*, Oxford master series in condensed matter physics (Oxford University Press, 2001).

[89] S. A. Wolf, D. D. Awschalom, R. A. Buhrman, J. M. Daughton, S. von Molnár, M. L. Roukes, A. Y. Chtchelkanova, and D. M. Treger, *Spintronics: A Spin-Based Electronics Vision for the Future*, Science **294**, 1488 (2001), DOI: 10.1126/science.1065389.

[90] D. Tillmann, R. Thiel, and E. Kisker, *Very-low-energy spin-polarized electron diffraction from Fe(001)*, Zeitschrift für Physik B Condensed Matter **77**, 1 (1989), DOI: 10.1007/BF01313611.

[91] R. Bertacco, M. Merano, and F. Ciccacci, *Spin dependent electron absorption in Fe(001)-p(1x1)O: A new candidate for a stable and efficient electron polarization analyzer*, Applied Physics Letters **72**, 2050 (1998), DOI: 10.1063/1.121261.

[92] T. Okuda, Y. Takeichi, Y. Maeda, A. Harasawa, I. Matsuda, T. Kinoshita, and A. Kakizaki, *A new spin-polarized photoemission spectrometer with very high efficiency and energy resolution*, Review of Scientific Instruments **79**, 123117 (2008), DOI: 10.1063/1.3058757.

[93] W. Auwärter, T. J. Kreutz, T. Greber, and J. Osterwalder, *XPD and STM investigation of hexagonal boron nitride on Ni(111)*, Surface Science **429**, 229 (1999), DOI: 10.1016/S0039-6028(99)00381-7.

[94] A. Taylor, J. Inst. Metals **77**, 585 (1950).

[95] H. A. Mook, *Magnetic Moment Distribution of Nickel Metal*, Physical Review **148**, 495 (1966), DOI: 10.1103/PhysRev.148.495.

[96] M. Corso, T. Greber, and J. Osterwalder, *h-BN on Pd(110): a tunable system for self-assembled nanostructures?*, Surface Science **577**, L78 (2005), DOI: 10.1016/j.susc.2005.01.015.

[97] T. Greber, L. Brandenberger, M. Corso, A. Tamai, and J. Osterwalder, *Single layer hexagonal boron nitride films on Ni(110)*, e-Journal of Surface Science and Nanotechnology **4**, 410 (2006), DOI: 10.1380/ejssnt.2006.410.

[98] F. Vincent and M. Figlarz, *Quelques Precisons sur les Paramtres Cristallins et Lintesite des Raies Debye-Scherrer du Cobalt Cubique et du Cobalt Hexagonal*, Comptes Rendus Hebdomadaires des Seances de L Academie des Sciences Serie C **264**, 1270 (1967).

[99] R. M. Moon, *Distribution of magnetic moment in hexagonal cobalt*, Physical Review **136**, A195 (1964), DOI: 10.1103/PhysRev.136.A195.

[100] A. B. Preobrajenski, M. L. Ng, N. A. Vinogradov, A. S. Vinogradov, E. Lundgren, A. Mikkelsen, and N. Mårtensson, *Impact of Oxygen Coadsorption on Intercalation of Cobalt under the h-BN Nanomesh*, Nano Letters **9**, 2780 (2009), DOI: 10.1021/nl901316p.

[101] F. X. Kayser, *Strains in FCC – HCP and FCC – DHCP transformations*, Scripta Metallurgica **5**, 1105 (1971), DOI: 10.1016/0036-9748(71)90182-7.

[102] B. Eisenmann and H. Schäfer, *Structure Data of Elements and Intermetallic Phases*, vol. 14a. Supplement and Extension to Volume III/6 of *Landolt-Börnstein - Numerical Data and Functional Relationships in Science and Technology - Group III: Crystal and Solid State Physics* (Springer-Verlag, 1986).

[103] S. Monastra, F. Manghi, C. A. Rozzi, C. Arcangeli, E. Wetli, H. J. Neff, T. Greber, and J. Osterwalder, *Quenching of Majority-Channel Quasiparticle Excitations in Cobalt*, Physical Review Letters **88**, 2364021 (2002), DOI: 10.1103/PhysRevLett.88.236402.

[104] F. J. Himpsel and D. E. Eastman, *Intrinsic Λ_1-symmetry surface state on Co(0001)*, Physical Review B **20**, 3217 (1979), DOI: 10.1103/PhysRevB.20.3217.
F. J. Himpsel and D. E. Eastman, *Experimental energy-band dispersions and magnetic exchange splitting for cobalt*, Physical Review B **21**, 3207 (1980), DOI: 10.1103/PhysRevB.21.3207.

[105] F. Batallan, I. Rosenman, and C. B. Sommers, *Band structure and Fermi surface of hcp ferromagnetic cobalt*, Physical Review B **11**, 545 (1975), DOI: 10.1103/PhysRevB.11.545.

[106] G. B. Grad, P. Blaha, K. Schwarz, W. Auwärter, and T. Greber, *Density functional theory investigation of the geometric and spintronic structure of h-BN/Ni(111) in view of photoemission and STM experiments*, Physical Review B **68**, 0854041 (2003), DOI: 10.1103/PhysRevB.68.085404.

[107] J. Osterwalder, *Correlation effects and magnetism in 3d transition metals*, Journal of Electron Spectroscopy and Related Phenomena **117-118**, 71 (2001), DOI: 10.1016/S0368-2048(01)00246-8.

[108] C. Lehmann, S. Sinning, P. Zahn, H. Wonn, and I. Mertig, *Fermi surfaces*, URL: http://www.physik.tu-dresden.de/ fermisur/.

[109] T. C. Schulthess, W. H. Butler, X. G. Zhang, D. M. C. Nicholson, and J. M. MacLaren, *Calculation of conductivity in the presence of structural defects: Application to spin dependence of conductivity in cobalt*, Physical Review B **56**, 8970 (1997), DOI: 10.1103/PhysRevB.56.8970.

[110] A. Varykhalov and O. Rader, *Graphene grown on Co(0001) films and islands: Electronic structure and its precise magnetization dependence*, Physical Review B **80**, 035437 (2009), DOI: 10.1103/PhysRevB.80.035437.

[111] D. Eom, D. Prezzi, K. T. Rim, H. Zhou, M. Lefenfeld, S. Xiao, C. Nuckolls, M. S. Hybertsen, T. F. Heinz, and G. W. Flynn, *Structure and Electronic Properties of Graphene Nanoislands on Co(0001)*, Nano Letters **9**, 2844 (2009), DOI: 10.1021/nl900927f.

[112] B. Voigtländer, G. Meyer, and N. M. Amer, *Epitaxial growth of thin magnetic cobalt films on Au(111) studied by scanning tunneling microscopy*, Physical Review B **44**, 10354 (1991), DOI: 10.1103/PhysRevB.44.10354.

[113] D. D. Chambliss, R. J. Wilson, and S. Chiang, *Nucleation of Ordered Ni Island Arrays on Au(111) by Surface-Lattice Dislocations*, Physical Review Letters **66**, 1721 (1991), DOI: 10.1103/PhysRevLett.66.1721.

[114] L. Huang, S. J. Chey, and J. H. Weaver, *Buffer-Layer-Assisted Growth of Nanocrystals: Ag-Xe-Si(111)*, Physical Review Letters **80**, 4095 (1998), DOI: 10.1103/PhysRevLett.80.4095.

[115] I. Brihuega, C. H. Michaelis, J. Zhang, S. Bose, V. Sessi, J. Honolka, M. Alexander Schneider, A. Enders, and K. Kern, *Electronic decoupling and templating of Co nanocluster arrays on the boron nitride nanomesh*, Surface Science **602**, L95 (2008), DOI: 10.1016/j.susc.2008.04.040.

[116] R. Decker, U. Schlickum, F. Klappenberger, G. Zoppellaro, S. Klyatskaya, M. Ruben, J. V. Barth, and H. Brune, *Using metal-organic templates to steer the growth of Fe and Co nanoclusters*, Applied Physics Letters **93**, 243102 (2008), DOI: 10.1063/1.3040328.

[117] H. Brune, *Microscopic view of epitaxial metal growth: nucleation and aggregation*, Surface Science Reports **31**, 125 (1998), DOI: 10.1016/S0167-5729(99)80001-6.

[118] W. Auwärter, M. Muntwiler, T. Greber, and J. Osterwalder, *Co on h-BN/Ni(111): from island to island-chain formation and Co intercalation*, Surface Science **511**, 379 (2002), DOI: 10.1016/S0039-6028(02)01545-5.

[119] W. Auwärter, *One Monolayer of Hexagonal Boron Nitride on Ni(111): an Atomically Sharp Interface*, Ph.D. thesis, University of Zürich (2003).

[120] J. F. Moulder, W. F. Stickle, P. E. Sobol, and K. D. Bomben, *Handbook of X-ray Photoelectron Spectroscopy : A Reference Book of Standard Spectra for Identification and Interpretation of XPS data* (Perkin-Elmer Corporation, Physical Electronics Division, Eden Prairie, Minnesota, 1992).

[121] P. Buluschek, *Submonolayer growth of cobalt on metallic and insulating surfaces studied by scanning tunneling microscopy and kinetic monte-carlo simulations*, Ph.D. thesis, Ecole Polytechnique Fédérale de Lausanne (2007).

[122] P. Gambardella, M. Blanc, H. Brune, K. Kuhnke, and K. Kern, *One-dimensional metal chains on Pt vicinal surfaces*, Physical Review B **61**, 2254 (2000), DOI: 10.1103/PhysRevB.61.2254.

[123] B. Predel, *Phase Equilibria, Crystallographic and Thermodynamic Data of Binary Alloys*, vol. 5c of *Landolt-Börnstein - Numerical Data and Functional Relationships in Science and Technology - Group IV: Macroscopic Properties of Matter* (Springer-Verlag, 1993).

[124] S. Weyeneth, *Anisotropic Properties and Critical Behavior of High-Temperature Superconductors*, Ph.D. thesis, University of Zürich (2009).

[125] S. Gsell, *Wachstum von grossflächigen einkristallinen Diamantschichten mittels Heteroepitaxie auf Silizium: Entwicklung von Pufferschichtsystemen und Untersuchung der Nukleationsmechanismen*, Ph.D. thesis, University of Augsburg (2008).

[126] Y. Xie, R. B. King, and H. F. Schaefer III, *Vibrational frequencies of the homoleptic cobalt carbonyls: $Co_4(CO)_{12}$ and $Co_6(CO)_{16}$*, Spectrochimica Acta Part A **61**, 1693 (2005), DOI: 10.1016/j.saa.2004.12.039.

[127] P. Chini, *Hexacobalt hexadecacarbonyl and its derivatives*, Chemical Communications (London) pp. 440–441 (1967), DOI: 10.1039/C19670000440.

[128] C. Egler, *Synthesis and Characterization of Cobalt Clusters*, Master's thesis, University of Zürich (2008).

[129] J. H. Scofield, *Hartree-slater subshell photoionization cross-sections at 1254 and 1487 ev*, Journal of Electron Spectroscopy and Related Phenomena **8**, 129 (1976), DOI: 10.1016/0368-2048(76)80015-1.

[130] G. Held, J. Schuler, W. Sklarek, and H. P. Steinrück, *Determination of adsorption sites of pure and coadsorbed CO on Ni(111) by high resolution X-ray photoelectron spectroscopy*, Surface Science **398**, 154 (1998), DOI: 10.1016/S0039-6028(98)80020-4.

[131] H. Ma, T. Brugger, S. Berner, Y. Ding, M. Iannuzzi, J. Hutter, J. Osterwalder, and T. Greber, *Nano-ice on Boron Nitride Nanomesh: Accessing Proton Disorder*, ChemPhysChem **11**, 399 (2009), DOI: 10.1002/cphc.200900857.

[132] J. O. Sofo, A. S. Chaudhari, and G. D. Barber, *Graphane: A two-dimensional hydrocarbon*, Physical Review B **75**, 153401 (2007), DOI: 10.1103/PhysRevB.75.153401.
D. W. Boukhvalov, M. I. Katsnelson, and A. I. Lichtenstein, *Hydrogen on graphene: Electronic structure, total energy, structural distortions and magnetism from first-principles calculations*, Physical Review B **77**, 035427 (2008), DOI: 10.1103/PhysRevB.77.035427.

[133] S. Ryu, M. Y. Han, J. Maultzsch, T. F. Heinz, P. Kim, M. L. Steigerwald, and L. E. Brus, *Reversible Basal Plane Hydrogenation of Graphene*, Nano Letters **8**, 4597 (2008), DOI: 10.1021/nl802940s.
D. C. Elias, R. R. Nair, T. M. G. Mohiuddin, S. V. Morozov, P. Blake, M. P. Halsall, A. C. Ferrari, D. W. Boukhvalov, M. I. Katsnelson, A. K. Geim, et al., *Control of Graphene's Properties by Reversible Hydrogenation: Evidence for Graphane*, Science **323**, 610 (2009), DOI: 10.1126/science.1167130.

[134] F. W. Averill, J. R. Morris, and V. R. Cooper, *Calculated properties of fully hydrogenated single layers of BN, BC_2N, and graphene: Graphane and its BN-containing analogues*, Physical Review B **80**, 195411 (2009), DOI: 10.1103/PhysRevB.80.195411.

[135] A. Varykhalov, J. Sánchez-Barriga, A. M. Shikin, C. Biswas, E. Vescovo, A. Rybkin, D. Marchenko, and O. Rader, *Electronic and Magnetic Properties of Quasifreestanding Graphene on Ni*, Physical Review Letters **101**, 157601 (2008), DOI: 10.1103/PhysRevLett.101.157601.

[136] S. Schwegmann, H. Over, V. De Renzi, and G. Ertl, *The atomic geometry of the O and CO + O phases on Rh(111)*, Surface Science **375**, 91 (1997), DOI: 10.1016/S0039-6028(97)01249-1.

[137] C. Stampfl, S. Schwegmann, H. Over, M. Scheffler, and G. Ertl, *Structure and Stability of a High-Coverage (1x1) Oxygen Phase on Ru(0001)*, Physical Review Letters **77**, 3371 (1996), DOI: 10.1103/PhysRevLett.77.3371.

Acknowledgment

First of all I would like to thank Thomas Greber for taking over the supervision of this thesis and for being a source of ideas, suggestions and visions. It was a pleasure to work under the vivid atmosphere which he spreads. Second I would like to thank Jürg Osterwalder for the possibility to carry out this thesis in his well positioned group and for his always constructive criticism. A big thanks also goes to Matthias Hengsberger a.k.a Matze for his immense patience whenever I needed help in the lab and for his constant sharing of knowledge. I also want to thank Harald Brune for the effort he made judging the thesis as an external expert.

A big thanks goes to Martin Morscher for the discussions about the fundamental aspects and the capabilities of our experimental methods and about our systems under investigation. Not to forget our periodic attempts to clear our minds running through the forest or enjoying a beer on Friday night. I also would like to thank Martin Klöckner for all the technical assistance and support during hard times with ESCA. Simon Berner and Martina Corso are acknowledged for their introduction into surface science and the handling of ESCA. Dominik Leuenberger, thank you for stimulating discussions and for your legendary lunchtime barbecues and your happy attitude. A thanks also goes to Haifeng Ma for sharing her experimental experience on the VT-STM and for introducing me a little bit to far east habits. I would like to thank Domenico Martoccia for the possibility to elucidate the prepared samples with a completely different experimental technique. A thank also goes to the Augsburg people, Stefan Gsell and Matthias Schreck for the supply of samples and for nice discussions during the Nanomesh meetings. I also would like to thank Stephen Weyeneth and Philipp Buluschek for the magnetization measurements of the samples.

The support and advice of the workshop team regarding technical issues is also greatly acknowledged, especially from Kurt Bösiger and Reto Maier. I thank Roland Bernet for the continuous IT support, Ruth Halter and Monika Röllin for their administrative support.

Finally I would like to mention the most important people. A big thanks goes to my family supporting me at all times. And to Kati: I am indebted to you for all your patience, your support over the years and your openness to experience new places.

Curriculum vitae

Name	BRUGGER Thomas
Birth	01.03.1980 in Friedrichshafen, Germany
Nationality	German

Education

1999	Abitur, Karl-Maybach-Gymnasium, Friedrichshafen, Germany
2000 – 2002	University of Konstanz, Germany, Studies of physics Elective courses: Computer science; business and administration
2002 – 2004	University of Karlsruhe (TH), Germany, Studies of physics Elective courses: Semiconductors and solar cells; biomedical metrology
Dec 2004 – Dec 2005	Diploma thesis in physics ‘Punktkontakt-Spektroskopie am Schwerfermionsupraleiter CeCoIn$_5$ im normalleitenden Zustand’ at the Physikalisches Institut, University of Karlsruhe
since Feb 2006	PhD studies of ‘Graphene and Hexagonal Boron Nitride on Transition Metals and their Application’ at the Physik-Institut, University of Zurich, Switzerland in the surface physics group of Prof. J. Osterwalder

Teaching

2003 – 2005	Teaching assistant, Physics department, University of Karlsruhe basic physics courses and lab-courses for students of chemistry and engineering
since Feb 2006	Teaching assistant, Physik-Institut, University of Zurich basic courses in mechanics, thermodynamics, optics, electricity and magnetism; lab-courses for medical student and for physics students; solid state physics

Publications

2010

- W. Moritz, B. Wang, M. L. Bocquet, T. Brugger, T. Greber, J. Wintterlin, and S. Günther, *Structure Determination of the Coincidence Phase of Graphene on Ru(0001)*, Physical Review Letters **104**, 1361021 (2010), DOI: 10.1103/PhysRevLett.104.136102.
- D. Martoccia, T. Brugger, M. Björck, C. M. Schlepütz, S. A. Pauli, T. Greber, B. D. Patterson, and P. R. Willmott, *h-BN/Ru(0001) nanomesh: A 14-on-13 superstructure with 3.5 nm periodicity*, Surface Science **604**, L16 (2010), DOI: 10.1016/j.susc.2010.01.003.
- D. Martoccia, S. A. Pauli, T. Brugger, T. Greber, B. D. Patterson, and P. R. Willmott, *h-BN on Rh(111): Persistence of a commensurate 13-on-12 superstructure up to high temperatures*, Surface Science **604**, L9 (2010), DOI: 10.1016/j.susc.2009.12.016.

2009

- T. Brugger, H. Ma, M. Iannuzzi, S. Berner, A. Winkler, J. Hutter, J. Osterwalder, and T. Greber, *Reversible switching of surface texture by hydrogen intercalation* (2009), submitted.
- H. Ma, T. Brugger, S. Berner, Y. Ding, M. Iannuzzi, J. Hutter, J. Osterwalder, and T. Greber, *Nano-ice on Boron Nitride Nanomesh: Accessing Proton Disorder*, ChemPhysChem **11**, 399 (2009), DOI: 10.1002/cphc.200900857.
- D. Martoccia, M. Bjoerck, C. Schlepuetz, T. Brugger, S. Pauli, B. Patterson, T. Greber, and P. Willmott, *Graphene on Ru(0001): A corrugated and chiral structure*, 0908.4517v1 (2009), URL: http://arxiv.org/abs/0908.4517.
- T. Brugger, S. Günther, B. Wang, J. H. Dil, M.-L. Bocquet, J. Osterwalder, J. Wintterlin, and T. Greber, *Comparison of electronic structure and template function of single-layer graphene and a hexagonal boron nitride nanomesh on Ru(0001)*, Physical Review B **79**, 045407 (2009), DOI: 10.1103/PhysRevB.79.045407.

2008

- M. Fischer, R. Brescia, S. Gsell, M. Schreck, T. Brugger, T. Greber, J. Osterwalder, and B. Stritzker, *Growth of twin-free heteroepitaxial diamond on Ir/YSZ/Si(111)*, Journal of Applied Physics **104**, 123531 (2008), DOI: 10.1063/1.3019046.
- D. Martoccia, P. R. Willmott, T. Brugger, M. Björck, S. Günther, C. M. Schlepütz, A. Cervellino, S. A. Pauli, B. D. Patterson, S. Marchini, et al., *Graphene on Ru(0001): A 25 x 25 Supercell*, Physical Review Letters **101**, 126102 (2008), DOI: 10.1103/PhysRevLett.101.126102.
- S. Gsell, S. Berner, T. Brugger, M. Schreck, R. Brescia, M. Fischer, T. Greber, J. Osterwalder, and B. Stritzker, *Comparative electron diffraction study of the diamond nucleation layer on Ir(001)*, Diamond and Related Materials **17**, 1029 (2008), DOI: 10.1016/j.diamond.2008.02.040.

2007

- A. Goriachko, Y. B. He, M. Knapp, H. Over, M. Corso, T. Brugger, S. Berner, J. Osterwalder, and T. Greber, *Self-Assembly of a Hexagonal Boron Nitride Nanomesh on Ru(0001)*, Langmuir **23**, 2928 (2007), DOI: 10.1021/la062990t.
- R. Widmer, S. Berner, O. Gröning, T. Brugger, J. Osterwalder, and T. Greber, *Electrolytic in situ STM investigation of h-BN-Nanomesh*, Electrochemistry Communications **9**, 2484 (2007), DOI: 10.1016/j.elecom.2007.07.019.

2006

- G. Goll, T. Brugger, M. Marz, S. Kontermann, H. v. Löhneysen, T. Sayles, and M. B. Maple, *Point-contact spectroscopy on heavy-fermion superconductors*, Physica B: Condensed Matter **378-380**, 665 (2006), DOI: 10.1016/j.physb.2006.01.419.

2005

- T. Brugger, *Punktkontakt-Spektroskopie am Schwerfermionsupraleiter* $CeCoIn_5$ *im normalleitenden Zustand*, Master's thesis, Universität Karlsruhe (2005).